



HAL
open science

Low Reynolds number hydrodynamics of immersed thin and slender bodies

Bingrui Xu

► **To cite this version:**

Bingrui Xu. Low Reynolds number hydrodynamics of immersed thin and slender bodies. Fluid Dynamics [physics.flu-dyn]. Université Paris Saclay (COmUE), 2016. English. NNT : 2016SACLS074 . tel-01308537

HAL Id: tel-01308537

<https://theses.hal.science/tel-01308537>

Submitted on 28 Apr 2016

HAL is a multi-disciplinary open access archive for the deposit and dissemination of scientific research documents, whether they are published or not. The documents may come from teaching and research institutions in France or abroad, or from public or private research centers.

L'archive ouverte pluridisciplinaire **HAL**, est destinée au dépôt et à la diffusion de documents scientifiques de niveau recherche, publiés ou non, émanant des établissements d'enseignement et de recherche français ou étrangers, des laboratoires publics ou privés.

NNT : 2016SACLS074

THÈSE DE DOCTORAT
DE
L'UNIVERSITÉ PARIS-SACLAY
PRÉPARÉE À
L'UNIVERSITÉ PARIS-SUD

ÉCOLE DOCTORALE N° 579
Sciences mécaniques et énergétiques, matériaux et géosciences

Spécialité de doctorat : Mécanique des fluides

Par

M. Bingrui XU

Hydrodynamique de fluides élançés à bas nombres de Reynolds

Thèse présentée et soutenue à Orsay, le 8 Avril 2016 :

Composition du Jury :

M. Basile AUDOLY	Directeur de Recherche, CNRS	Président du jury
M. Thomas CUBAUD	Associate Professor, State University of New York	Rapporteur
M. Francois GALLAIRE	Professeur associé, École Polytechnique Fédérale de Lausanne	Rapporteur
M. Harold AURADOU	Directeur de Recherche, CNRS	Examinateur
Mme Olivia DU ROURE	Chargée de recherche, l'ESPCI de Paris	Examinatrice
Mme Laurette TUCKERMAN	Directeur de Recherche, CNRS	Examinatrice
M. Neil RIBE	Directeur de Recherche, CNRS	Directeur de thèse
M. Damir JURIC	Chargé de Recherche, CNRS	Co-directeur de thèse
M. Jalel CHERGUI	Ingénieur de Recherche, CNRS	Co-directeur de thèse

Acknowledgements

I would like to express my gratitude to all the people who have contributed to the realization of this thesis. Neil, Damir and Jalel, thank you for your availability and for guiding me in my work during these three and half years. Neil, thank you especially for having supported me in the most difficult moments, encouraging me to go forward. I am really grateful that I was part of the laboratory FAST and LIMSI, where I shared both happy and funny moments but also stressed days. I would like to thank everyone in both laboratory FAST and LIMSI: Nicolas and Manish with whom I began this adventure, Anne, Anna, Sarah, Antoine, Anna, Maregrite for her friendship, Gianluca, Adama and other talented researchers, engineers and Ph.D. students. Special thanks goes to Marc and Neil for their help to find the fund of extra 6 months. Great thanks to Thomas Cubaud and Basile Audoly for the helpful discussions. Merci to Xavier Quidelleur and Kim Ho in the doctoral school SMEMaG.

I am grateful to François Gallaire, Thomas Cubaud, Harold Auradou, Olivia Du Roure and Laurette Tuckerman for reading this manuscript and attending the defense, and to Basile Audoly for presiding over the jury.

Acknowledgement goes to the China Scholarship Council (CSC) which has funded this thesis for three years, and to the Centre National de la Recherche Scientifique (CNRS) for the funding of extra months.

Also, I would like to thank my friends Zheng, Nan, Ming, Bo, Ji, Tongzhou, Yihao, Changyou, Chentao and ma belle Hui, with whom I enjoyed a lot of happy hours during the weekends and vacations. And as always, my family is always my last fortification, thank you mom and dad.

Orsay, 10 April 2016

Bingrui XU

Abstract

The subject of this thesis is the hydrodynamics of thin (sheet-like) and slender (filamentary) bodies of viscous fluid immersed in a second fluid with a different viscosity. We focus on two examples: the subduction of oceanic lithosphere; and the buckling of viscous threads injected into diverging microchannels. Despite the very different physical scales of the two phenomena, both have a characteristic Reynolds number $Re \ll 1$.

For the case of a thin subducting sheet, we propose a new hybrid boundary integral-thin sheet method (BITS) that combines an asymptotic thin-sheet formulation for the sheet with a boundary-integral representation of the outer flow. At present the model is limited to two dimensions, i.e. the sheet extends infinitely in the trench-parallel direction. The BITS equations are solved using a method based on discrete differential geometry developed by Audoly et al. (2013). The new BITS method is validated by comparing its predictions with those of a full two-dimensional boundary-element code. To model subduction using BITS, we suppose that the sheet initially comprises a long horizontal part (the ‘plate’) connected to a short bent part (the ‘slab’) whose negative buoyancy drives the subduction. We first perform a suite of instantaneous flow solutions for different values of the length of the slab, its inclination, and the viscosity ratio between the sheet and the ambient fluid. As an output parameter, we focus on the vertical sinking speed V of the

slab's leading end. Scaling analysis suggests that the normalized sinking speed $V/V_{\text{Stokes}} = \text{fct}(St)$, where V_{Stokes} is the slab's characteristic Stokes sinking speed and St is the sheet's 'flexural stiffness'. The scaling analysis is confirmed by the fact that the numerical predictions of V/V_{Stokes} collapse onto a single master curve as a function of St . The curve has two limits: a limit $St \leq 1$ for which the sinking speed is controlled by the viscosity of the ambient mantle, and a limit $St \gg 1$ in which it is controlled by the viscosity of the sheet itself (bending resistance). We then proceed to obtain time-dependent solutions for the evolution of the sheet's shape and thickness. For moderate viscosity ratios (≈ 100), the sheet thins substantially as it sinks, but not enough to lead to the 'slab breakoff' that is observed in several subduction zones on Earth. We propose that slab breakoff may be modelled using a modified BITS model with a non-Newtonian rheology; work on this is ongoing.

Next, the parallel code BLUE for multi-phase flows is used to simulate three-dimensional viscous folding in diverging microchannels. The code BLUE, developed by S. Shin and thesis co-supervisors D. Juric and J. Chergui, treats the free interface with a parallel Lagrangian front tracking method. Inspired by T. Cubaud's experiments, the calculation domain is a micro rectangle of dimensions $2 \text{ mm} \times 0.25 \text{ mm} \times 5 \text{ mm}$. The more viscous liquid L_1 with viscosity η_1 is injected into the channel from the center inlet at a volumetric rate Q_1 , and the less viscous liquid L_2 with viscosity η_2 from two side inlets at a total volumetric rate Q_2 . Liquid L_1 takes the form of a thin filament due to hydrodynamic focusing in the long channel that leads to the diverging region. Given the long computation time, we were limited to a parameter study comprising five simulations in which the flow rate ratio, the viscosity ratio, the Reynolds number, and the shape of the channel were varied relative to a reference model. The thread becomes unstable to a folding instability after its entry into the main chamber, due to the longitudinal

compressive stress applied to it by the diverging flow of liquid L_2 . The initial folding axis can be either parallel or perpendicular to the narrow dimension of the chamber. In the former case, the folding slowly transforms via twisting to perpendicular folding, or may disappear totally. The direction of folding onset is determined by the velocity profile and the elliptical shape of the thread cross section in the channel that feeds the diverging part of the cell. Due to the high viscosity contrast and very low Reynolds numbers involved, direct numerical simulations of this two-phase flow are very challenging and to our knowledge these are the first three-dimensional direct parallel numerical simulations of viscous threads in microchannels. However, since the computational time for these simulations is quite long, especially for such viscous threads, the simulations present only the early time onset of the buckling instability of the threads, thus long-time comparisons with experiments for quantities such as folding amplitude and frequency are limited.

Résumé

Cette thèse concerne la simulation numérique d'écoulement de nappes et de filamenteux de fluides visqueux en présence d'une seconde phase fluide non-miscible dont la viscosité est différente. Deux exemples sont présentés. Celui de la subduction de la lithosphère océanique ainsi que celui du flambage de filaments visqueux dans un micro-canal divergent. En dépit des très différentes échelles physiques des deux phénomènes, ces deux écoulements sont en particulier caractérisés par un nombre de Reynolds relativement bas ($Re \ll 1$).

Dans le premier cas, une nouvelle méthode hybride dite BITS (Boundary Integral & Thin Sheet) est proposée : elle, combine une formulation asymptotique de la nappe mince avec une représentation intégrale aux frontières de l'écoulement extérieur. Actuellement, le modèle est limité à deux dimensions, à savoir la nappe se prolonge à l'infini dans la direction de la tranchée parallèle. Les équations de BITS sont résolues en utilisant une méthode basée sur la géométrie différentielle discrète, développée par Audoly et al. (2013). Nous validerons les résultats de la nouvelle méthode BITS avec ceux obtenus et confirmés par une méthode bi-dimensionnelle dite d'éléments aux frontières (Ribe, 2010). Afin de modéliser le phénomène de subduction, nous supposons dans la méthode BITS, que la nappe est composée d'une longue partie horizontale reliée à une partie coudée plus courte (le 'slab') dont la flottabilité négative

entraîne la subduction. Les solutions instationnaires sont obtenues avec différentes valeurs de la longueur et l'inclinaison de la partie coudée (le 'slab'), et en faisant varier le rapport de viscosité entre la nappe et le fluide ambiant. L'un des paramètres de sortie sur lequel nous nous concentrons est la vitesse d'immersion verticale V à l'extrémité du slab. L'analyse des échelles suggère que la vitesse normalisée V/V_{Stokes} est une fonction de St , où V_{Stokes} est la vitesse caractéristique du slab et St est la rigidité en flexion de la nappe. L'analyse des échelles indique une bonne concordance avec les prédictions numériques que nous avons obtenues. La courbe $V/V_{Stokes} = \text{fct}(St)$ présente deux limites : une limite $St \leq 1$ pour laquelle la subduction est contrôlée par la viscosité du manteau ambiant, et une limite $St \gg 1$ où elle est contrôlée par la viscosité de la nappe (résistance à la flexion). Nous déterminons des solutions pour l'évolution de la forme et l'épaisseur de la nappe en fonction du temps. A des nombres de Reynolds modérés (~ 100), la nappe s'amincit considérablement pendant son écoulement sans pour autant atteindre sa rupture tel que cela est observé dans différentes régions de subduction terrestre. Nous proposons que la rupture de la nappe puisse être modélisée à l'aide de la méthode BITS, en tenant compte d'une rhéologie non-newtonienne; les travaux à ce sujet étant en cours.

Dans le second cas, nous avons utilisé le code BLUE pour réaliser cinq simulations numériques 3D diphasiques d'écoulements visqueux dans une configuration de flambage en micro-canal divergent. Le code BLUE, développé par S. Shin et deux co-directeurs de la thèse D. Juric et J. Chergui, traite l'interface libre avec une méthode parallèle de front-tracking. Inspiré par des expériences de T. Cubaud, le domaine de calcul est un micro rectangle de dimensions $2 \text{ mm} \times 0,25 \text{ mm} \times 5 \text{ mm}$. Le liquide le plus visqueux L_1 avec une viscosité η_1 , est injecté au centre de l'entrée du canal à un débit volumique Q_1 . Le liquide le moins visqueux L_2 de une viscosité η_2 , est injecté à partir de deux entrées latérales à

un débit volumique total Q_2 . Le liquide L_1 prend la forme d'un filament mince dans le long du canal qui mène au région divergent en raison du 'focusing' hydrodynamique. Compte tenu de la longue durée de calculs, nous étions limités à une étude paramétrique comprenant cinq simulations. L'écoulement dépend de plusieurs paramètres dont le rapport des débits volumétriques, le rapport des viscosités, le nombre de Reynolds et l'angle du micro-canal divergent. Il apparaît de cette étude que le filament présente une instabilité du type flambage en raison de la contrainte de compression longitudinale qui lui est appliquée par le flux divergent du liquide L_2 . L'axe principal de flambage peut être alors parallèle ou perpendiculaire à la direction étroite de la chambre. Dans le cas parallèle, le flambage tend lentement vers un flambage perpendiculaire au moyen d'une torsion ou peut totalement disparaître. La direction d'apparition du flambage est déterminée par le profil de vitesse et la forme elliptique de la section transversale du filament, dans le canal qui alimente la partie divergente. En raison du grand rapport des viscosités et des bas nombres de Reynolds, les simulations numériques de cet écoulement diphasique sont très difficiles. A notre connaissance, ce sont les premières simulations numériques tridimensionnelles directes parallèles de filaments visqueux dans des micro-canaux. Toutefois, le temps de calculs étant très long, surtout pour de tels liquides visqueux, les simulations présentent seulement le début de l'instabilité de flambage des filaments. Ainsi, les comparaisons avec des expériences (Cubaud and Mason, 2006a) pour des grandeurs telles que l'amplitude et la fréquence de flambage restent limitées.

Contents

Acknowledgements	i
Abstract	iii
Résumé	vii
1 Introduction	1
1.1 Free subduction	2
1.2 Buckling instabilities in microchannels	9
2 Thin Newtonian sheets: The discrete approach	17
2.1 Thin-sheet theory: essential concepts	17
2.2 Lagrangian description of a thin sheet	20
2.3 Boundary-integral equation for an immersed fluid sheet .	23
2.4 The discrete viscous thin sheet model	26
3 Subduction of a Newtonian sheet	35
3.1 Bending and stretching dissipation potentials of a Newtonian sheet	36
3.2 Numerical implementation	38
3.3 The Green's function for sheet subduction	40
3.4 Numerical solutions and analysis	43

3.4.1	Vertical sheet	43
3.4.2	Horizontal sheet	45
3.4.3	Subduction of a bent sheet	54
4	Parallel code for three dimensional multiphase flow	65
4.1	Mathematical formulation	65
4.2	Numerical method	67
4.2.1	Interface treatment	68
4.2.2	Extended interface for parallel processing	71
4.2.3	Solution procedure in parallel computing	74
5	Simulation of viscous folding in diverging microchannels	79
5.1	Thread formation	83
5.2	Folding instability	93
6	Conclusion	111
6.1	Summary of results obtained	111
6.2	Future perspectives	115
	Bibliography	119

List of Figures

1.1	The subduction of oceanic lithosphere into the Earth's mantle	3
1.2	Laboratory setup used for studying subduction by Funicciello and co-workers (Funicciello et al., 2006).	4
1.3	Modes of free subduction observed in analogue laboratory experiments.	7
1.4	Phase diagram of the modes of free subduction as a function of the viscosity ratio γ and the ratio D/h of the layer depth to the sheet thickness.	8
1.5	Schematic diagram of Cubaud's experimental setup.	12
1.6	Viscous folding of a thread in diverging microchannels for different channel angles and flow rate ratios.	13
1.7	Regime diagram for two-dimensional flow patterns in diverging channels as functions of the flow ratio ϕ , the viscosity ratio χ , and the channel shape (Chung et al., 2010)	15
2.1	A viscous thin sheet	18
2.2	Discrete representation of the sheet's centerline as a polygonal curve with $n + 2$ vertices and $n + 1$ edges.	27
3.1	A thin sheet of viscous fluid immersed in a second fluid with a different viscosity.	36

3.2	Band structure of the dissipation matrices $\underline{\underline{D}}_s$ and $\underline{\underline{D}}_b$. .	41
3.3	Geometry of the vertical (solid line) and horizontal (dashed line) sheets used to test the numerical BITS code.	43
3.4	Velocity solutions for a vertical sheet at different viscosity ratios γ with a length $L = 20H_0$ and a distance $d = 10H_0$ below the free surface	44
3.5	Vertical velocity $v/(H_0^2 g \delta \rho / \eta_1)$ predicted by BITS for the vertical sheet at $\gamma = 1$ and $\gamma = 100$	46
3.6	Vertical velocities of a vertical sheet with $L = 20H_0$, $d = 10H_0$, $\gamma = 100$ and different discretization numbers. . . .	47
3.7	Velocity fields predicted by BITS for a sinking horizontal sheet with two different viscosity ratios γ	48
3.8	The sinking velocity predicted by the BITS and BEM models for a horizontal sheet	51
3.9	Sinking velocities of a horizontal sheet with $L = 20H_0$ and $\gamma = 10000$ as a function of discretization number . .	52
3.10	Sinking velocities of a horizontal sheet with $L = 40H_0$ and $\gamma = 10000$ as a function of discretization number . .	53
3.11	Instantaneous velocity field of a sheet with $L = 40H_0$, $\gamma = 1000$ and $d = H_0$, for two different resolutions. . . .	55
3.12	Instantaneous velocity field of a sheet with $L = 40H_0$, $\gamma = 1000$, and $\delta S = 0.02H_0$ for two values of the lubrication layer thickness.	56
3.13	Instantaneous velocity field of a sheet with $L = 60H_0$, $\gamma = 1000$, and $\delta S = 0.02H_0$ for two values of the lubrication layer thickness.	57
3.14	The curling rate of a bent sheet with $L = 40H_0$, $\gamma = 100$ and $d = 0.5H_0$	59

3.15	Dimensionless sinking speed V/V_{Stokes} of the slab as a function of the sheet stiffness St , for three different values of the dip θ_0	60
3.16	Shape (a) and thickness (b) of a sheet with $L = 40H_0$, $d = 0.2H_0$, $\theta_0 = 30^\circ$ and $\gamma = 1000$ at different times from 0 to $35\tau_0$	62
3.17	Shape (a) and thickness (b) of a sheet with $L = 40H_0$, $d = 0.2H_0$, $\theta_0 = 30^\circ$ and $\gamma = 100$ at different times from 0 to $35\tau_0$	63
4.1	Level contour reconstruction in a 2D calculation. Interfaces are reconstructed by linear approximation of the $\phi_f = 0.5$ contour in each grid cell.	70
4.2	Procedure for LCRM in three-dimensions	71
4.3	Domain decomposition concept for distributed processing.	73
4.4	Extended interface concept using buffer zone for distributed processing with the LCRM.	75
5.1	The calculation domain of the microchannel.	80
5.2	Velocity field on the channel midsurface with $Re_1 = 1.64 \times 10^{-3}$, $\chi = 2174$, $\phi = 1/12$ and $\alpha = \pi/2$ (case 2) using a low resolution $128 \times 32 \times 256$	84
5.3	Formation of viscous threads by hydrodynamic focusing and contact line detachment (thin lines) from the channel walls.	86
5.4	Three-dimensional velocity fields of hydrodynamic focusing with $Re_1 = 1.64 \times 10^{-3}$, $\phi = 1/12$, $\chi = 2174$, $\alpha = \pi/2$ (case 2) showing cross section across the channel width and cross section across the channel depth.	88

5.5	The velocity contour of cross sections across the depth at different positions $z = 2.2$ mm, $z = 2.5$ mm, $z = 3$ mm, $z = 4$ mm for case 2 ($\text{Re}_1 = 1.64 \times 10^{-3}$, $\phi = 1/12$, $\chi = 2174$, $\alpha = \pi/2$)	89
5.6	The minor axis ϵ_1 and major axis ϵ_2 of the thread along the flow direction for case 2 ($\text{Re}_1 = 1.64 \times 10^{-3}$, $\phi = 1/12$, $\chi = 2174$, $\alpha = \pi/2$)	90
5.7	Downstream evolution of core diameter ϵ/w versus flow rate ratio ϕ for a thread in plug flow in a square microchannel.	92
5.8	Evolution of core diameter ϵ/w versus flow rate ratio ϕ for a thread in plug flow in a square microchannel.	94
5.9	The flow patterns at different times for case 1 with $\text{Re}_1 = 2.74 \times 10^{-4}$, $\phi = 1/12$, $\chi = 2174$, $\alpha = \pi/2$	96
5.10	The velocities along the middle line of the cross section at $z = 2.5$ mm at different times corresponding to the flow patterns in Fig. 5.9.	97
5.11	The flow patterns at different times for case 2 with $\text{Re}_1 = 1.64 \times 10^{-4}$, $\phi = 1/12$, $\chi = 2174$, $\alpha = \pi/2$	100
5.12	The flow patterns at different times for case 3 with $\text{Re}_1 = 2.74 \times 10^{-4}$, $\phi = 1/12$, $\chi = 1000$, $\alpha = \pi/2$	102
5.13	The flow patterns at different times for case 5 with $\text{Re}_1 = 2.74 \times 10^{-4}$, $\phi = 1/12$, $\chi = 1000$, $\alpha = \pi$	104
5.14	The velocity contour and thread shape (black line) at $z = 2.5$ mm before the diverging point for the 5 cases	107
5.15	The velocities along the center line (solid line) and mid-line (dashed line) on the cross section at $z = 2.5$ mm for different cases.	108

5.16	The derivatives $\partial v_z/\partial z$ of the velocity v_z on the thread interface before onset of folding at $t = 0.178$ s for case 1 with $\text{Re}_1 = 2.74 \times 10^{-4}$, $\phi = 12$, $\chi = 2174$, $\alpha = \pi/2$	108
5.17	The bending moment at $z = 1.7$ mm for case 1 with $\text{Re}_1 = 2.74 \times 10^{-4}$, $\phi = 1/12$, $\chi = 2174$, $\alpha = \pi/2$ when the folding instability occurs.	109
5.18	The bending moment at $z = 1.7$ mm for case 2 with $\text{Re}_1 = 1.64 \times 10^{-3}$, $\phi = 1/12$, $\chi = 2173$, $\alpha = \pi/2$ when the folding instability occurs.	110

List of Tables

5.1	Dimensional and nondimensional parameters for the simulation case 1 with $\chi = 2174$, $\phi = 1/12$ and $\alpha = \pi/2$. . .	82
5.2	Dimensional and nondimensional parameters for the 5 simulations	83
5.3	The stable ϵ_1 , ϵ_2 , ϵ_1/w , ϵ_2/w and ϵ_1/ϵ_2 for all 5 cases . .	87

Chapter 1

Introduction

Thin and slender bodies immersed in fluids occur widely in nature and technology. In biology, microscopic organisms such as bacteria and spermatozoa propel themselves in viscous fluid by waving long slender flagellae (Toppaladoddi and Balmforth, 2014). In construction, metal reinforcing rods are immersed in liquid concrete before it hardens. Undersea telephone and fiber optics cables make rapid communication possible. Finally, in the chemical and food industries, one often encounters suspensions of small rod-like or plate-like particles (Tornberg and Shelley, 2004).

In all the above examples, the immersed body is solid or elastic. But there are other cases in which the immersed body is itself a viscous fluid. In these situations, the viscosity of the body plays a role analogous to that of elasticity in the case of solid bodies. However, immersed thin and slender fluid bodies have been much less studied than their elastic counterparts.

This thesis focuses on two examples of immersed thin or slender fluid bodies. The first is the subduction of oceanic lithosphere, a crucial part of the Earth's plate tectonic cycle. In this case the lithosphere can

be regarded as a thin viscous sheet immersed in the substantially less viscous mantle. The typical thickness of the lithosphere is 50-80 km, and the typical depth of subduction is in the range 660-2900 km, so that the subducted portion of the lithosphere (the so-called ‘slab’) is strictly speaking a ‘thin’ body with one characteristic dimension much smaller than the other two. The second case we study is the buckling of viscous threads in diverging microchannels. In this case the immersed body is ‘slender’, because it has two characteristic dimensions that are much smaller than the third. But despite the very different geometries and physical scales of the two phenomena, both are characterized by a small Reynolds number $Re \ll 1$. Inertia is therefore negligible, and the flow in both cases is ‘Stokes’ or ‘creeping’ flow.

1.1 Free subduction

Subduction, the free sinking of dense (oceanic) lithosphere into the Earth’s mantle, is shown schematically in Fig. 1.1. Subduction is an essential feature of the planet’s plate tectonics, because the negative buoyancy of the slabs drives mantle convection. Subduction also generates most of the great earthquakes and the explosive volcanoes on Earth, and is the main process responsible for recycling oceanic crust and volatile species like H_2O and CO_2 .

Because of its geophysical importance, subduction has been the object of numerous studies aiming to understand its physical mechanisms. Perhaps the simplest reasonable model comprises a single dense and highly viscous sheet (density $\rho + \delta\rho$, viscosity η_2 and initial thickness h_0) that sinks into a mantle with density ρ and viscosity $\eta_1 \ll \eta_2$. Experimentally, this model has been studied with different pairs of materials representing the plate and mantle: rubber and water (Jacoby,

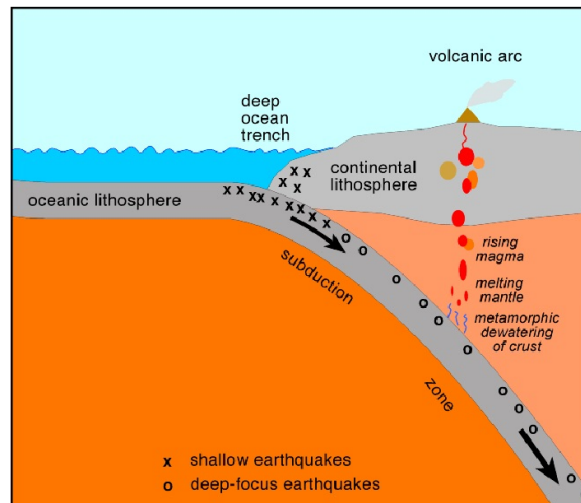


Figure 1.1: The subduction of oceanic lithosphere into the Earth's mantle

1973), solid and molten paraffin (Jacoby, 1976), very viscous and less viscous corn syrup (Kincaid and Olson, 1987), and silicone putty and honey or glucose syrup (Funiciello et al., 2003a, 2006, 2008; Schellart, 2004b,a, 2008; Schellart et al., 2010; Faccenna et al., 2007). In these experiments, one edge of the flat sheet on the surface of the low viscosity fluid is pushed down to create a short slab, which initiates the subduction. A schematic view of Funiciello and co-workers' experiments is shown in Fig. 1.2 (Funiciello et al., 2006). The evolving shape of the sheet is observed with video cameras, and the velocity field of the surrounding fluid using either Particle Image Velocimetry (PIV) (Kincaid and Griffiths, 2003) or Feature Tracking (FT) (Funiciello et al., 2006). But obtaining good quantitative measurements in this way is laborious.

Subduction has also been studied extensively using numerical techniques. There are three different approaches. The first is to solve the governing equations using full continuum descriptions of both the

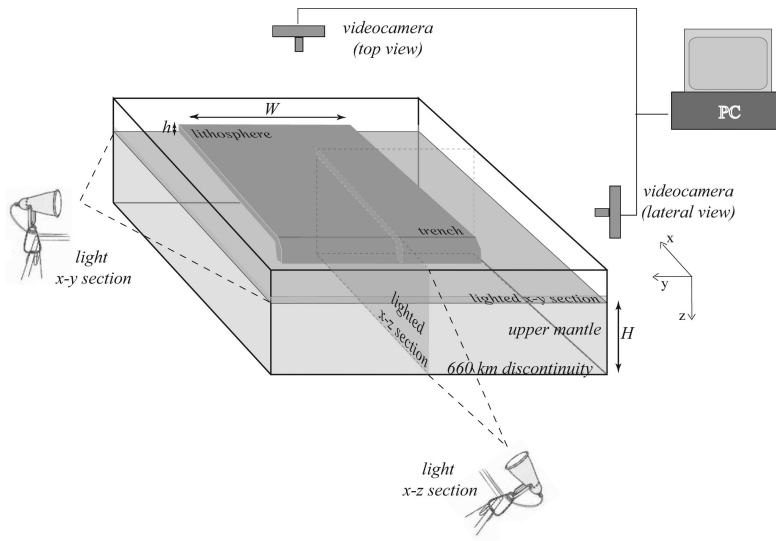


Figure 1.2: Laboratory setup used for studying subduction by Funciello and co-workers (Funciello et al., 2006). The lithosphere is simulated by means of a silicone plate of density ρ_l , viscosity η_l , width w , thickness h , and length L . The mantle is simulated by means of glucose syrup of density ρ_m , viscosity η_m , and thickness $H = 0.11$ m. Experiments are monitored over their entire duration using two video cameras to record lateral and top views perpendicular to two illuminated planes.

sheet and the surrounding fluid. The solutions can be either steady-state (Conrad and Hager, 1999), quasi-static (Piromallo et al., 2006), or fully time-dependent. In this last category, some simulations are two-dimensional (Enns et al., 2005; Manea and Gurnis, 2007; Di Giuseppe et al., 2008; Schmeling et al., 2008; Capitanio et al., 2009) and others are in three dimensions (Morra et al., 2006, 2009; Stegman et al., 2006, 2010a,b; Schellart et al., 2007; Capitanio and Morra, 2012; Manea et al., 2012). These numerical simulations capture well the self-consistent interaction between the sheet and the surrounding fluid. But they are computationally expensive and the treatment of the point (or line) where the sheet separates from the upper surface is difficult (Schmeling et al., 2008).

The second numerical approach is to describe the dynamics of the sheet and/or the surrounding mantle in a parametrized way, so that an explicit determination of the flow is not necessary. One can, for example, represent the viscous stresses exerted by the external fluid by a prescribed distribution of dashpots (Funicello et al., 2003b) or by drag coefficients obtained from analytical solutions of the Stokes equations for idealized geometries (Capitanio et al., 2007, 2009; Goes et al., 2008). At the opposite extreme, Conrad and Hager (2001) combine a parametrized representation of the sheet's deformation with an explicit calculation of the surrounding flow. There are even a few models in which the flows in both the sheet and the surrounding fluid are parametrized (Buffett and Rowley, 2006). All these methods are computationally efficient, but the lack of full fluid-mechanical self-consistency is a serious drawback.

A third approach is to use the boundary element method (BEM). This semianalytical method is based on the boundary-integral representation of Stokes flow, whereby the flow in a volume of fluid is represented by weighted integrals of the velocity and stress over the boundaries of the volume. A two-dimensional model of this kind was studied by Ribe

(2010), and extended to three dimensions by Li and Ribe (2012). There have also been several BEM studies of subduction in spherical geometry (Morra et al., 2009; Capitanio and Morra, 2012). The advantages of BEM method are several: a total absence of unwanted wall effects, reduction of the dimensionality of the problem by one (from 3-D to 2-D or 2-D to 1-D), and the possibility of using Green's functions that satisfy identically the boundary conditions on horizontal boundaries. Disadvantages include a lack of flexibility, as well as the dense character of the matrix describing the interaction of each boundary node with every other.

The above-mentioned experimental and numerical studies have yielded much insight into free subduction driven by negative buoyancy, in which the dense and highly viscous sheet drives flow in the ambient fluid and is in turn deformed by it. Many features of subduction in the geological record can be explained by these results, such as the correlation between trench and plate velocities (Stegman et al., 2006; Funicello et al., 2008), the shapes of trenches and island arcs (Morra et al., 2006; Schellart et al., 2007), and the factors controlling the mode or style of subduction (Bellahsen et al., 2005; Schellart, 2008; Stegman et al., 2010a; Ribe, 2010). Concerning the last point, laboratory experiments have revealed that subduction can occur in several distinct modes, including trench-retreating, folding, trench-advancing, and strong trench retreating when the viscosity ratio $\gamma = \eta_2/\eta_1$ is very large (Bellahsen et al., 2005; Di Giuseppe et al., 2008; Schellart, 2008; Stegman et al., 2010a). Photographs of these modes are shown in Fig. 1.3. Based on laboratory experiments, Schellart (2008) proposed a regime diagram for the four modes mentioned above as a function of the viscosity ratio γ and the ratio D/H of the layer depth to the sheet thickness, as shown in Fig. 1.4. Li and Ribe (2012) showed that the mode of subduction is selected by the angle at which the slab first impinges on the bottom of

the experimental tank, which corresponds to a depth of 660 km in the Earth. These authors further identified a key dimensionless parameter, the ‘bending stiffness’

$$St = \frac{\eta_2}{\eta_1} \left(\frac{h}{l_b} \right)^3, \quad (1.1)$$

which determines whether the subduction rate is controlled by the viscosity of the ambient fluid ($St \sim O(1)$) or by the viscosity of the sheet itself ($St \gg 1$). In (1.1), l_b is the ‘bending length’, i.e. the length of the portion of the sheet (the slab plus the seaward flexural bulge) where deformation occurs primarily by bending as opposed to stretching/shortening.

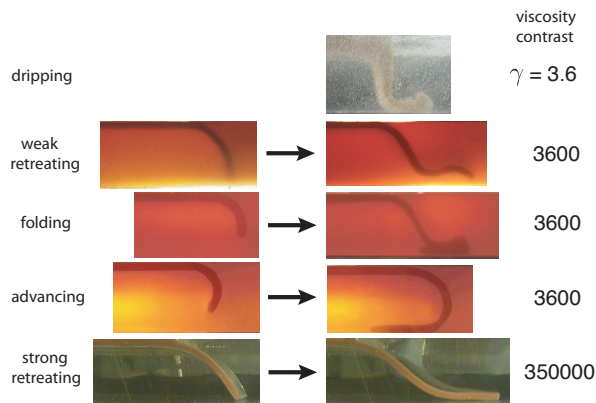


Figure 1.3: Modes of free subduction observed in analogue laboratory experiments. The photographs in the left-hand column were taken before the sheet’s leading end reached the bottom of the experimental tank, and those in the right-hand column some time after. The viscosity contrast γ for each experiment is indicated at far right. Photographs courtesy of F.Funiciello.

In the BEM models of Ribe (2010) and Li and Ribe (2012), the theory of thin viscous sheets (see below) is used *a posteriori* as an interpretative

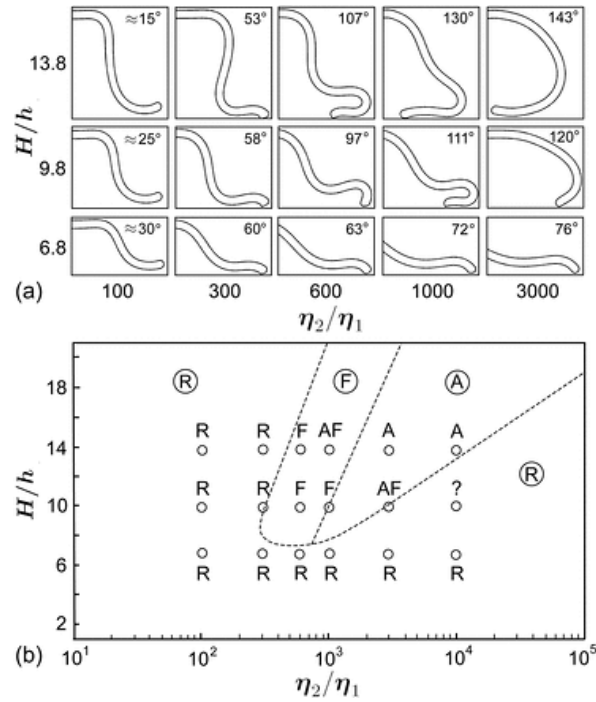


Figure 1.4: Phase diagram of the modes of free subduction as a function of the viscosity ratio γ and the ratio D/h of the layer depth to the sheet thickness. Fields: trench retreating, folding and trench advancing modes, adapted from Fig. 13 of Schellart (2008). Dots: subduction mode observed in numerical BEM solutions of Li and Ribe (2012). AF (advancing trench with folding) is a new mode not (yet) seen in laboratory experiments.

tool. In this thesis, we pursue an alternate route by developing a new approach in which thin-sheet theory is built in from the start. We call the hybrid model that results the ‘BITS’ (Boundary-integral/thin sheet) model. Unlike the full BEM models, the BITS approach can be used for either Newtonian or non-Newtonian sheets. The Newtonian case is discussed in Chapter 3 of this thesis, and work on the non-Newtonian case is ongoing.

1.2 Buckling instabilities in microchannels

The folding of viscous threads in diverging microchannels has recently attracted much attention due to the need to mix two fluids with very different viscosities. The dynamics of viscous multiphase flows at small scales is important in industrial technology (oil recovery, biodiesel production, etc.). Microfluidic devices are well suited for studying precisely controlled flow geometries and finely manipulating the fluid, and can be used to produce individual bubbles, droplets and complex soft materials (Utada et al., 2005; Cubaud et al., 2005; Meleson et al., 2004). The effective mixing is of great importance in these various microfluidic applications. But microfluidic flows are usually laminar, so liquid streams are parallel and different fluids can only mix by diffusion. The time scale associated with diffusion, $t_d = h^2/D$, where h is the characteristic length scale and D is the diffusion coefficient between the liquids, is typically much larger than the time scale associated with convection, $t_c = h/U$, where U is the characteristic flow velocity. Therefore, diffusion alone is an extremely inefficient mixing method.

There are different innovative strategies to enhance mixing in microfluidics, which can be classified as either active or passive methods. In active methods an external forcing is imposed by e.g. rotary pumps

(Chou et al., 2001), forced oscillatory transverse flows (Bottausci et al., 2004) or electric or magnetic fields (Paik et al., 2003a,b; Pollack et al., 2002; Paik et al., 2003b; Kang et al., 2007a,b; Rida and Gijs, 2004). Passive methods rely on a particular design of the microchannel, including patterned surface relief (Chen et al., 2009; Bringer et al., 2004; Stroock et al., 2002a,b). However, industrial and biological fluids usually exhibit widely different viscosities and the relative motions between the fluids are complex. In this thesis we study one promising method, wherein periodic folding of viscous threads injected into microchannels enhances mixing by greatly increasing the specific surface area of the fluid/fluid interface.

The buckling (folding or coiling) of slender viscous threads is familiar to anyone who has ever poured honey or molten chocolate onto toast. Taylor (1969) investigated the viscous buckling problem and suggested that the instability requires an axial compressive stress, like the more familiar ‘Euler’ buckling of a compressed elastic rod. Since then, viscous buckling has been studied by numerous authors using experimental, theoretical, and numerical approaches (Cruickshank and Munson, 1982b,a, 1983; Cruickshank, 1988; Griffiths and Turner, 1988; Tchavdarov et al., 1993; Mahadevan et al., 1998; Skorobogatiy and Mahadevan, 2000; Tome and Mckee, 1999; Ribe, 2004; Ribe et al., 2006; Maleki et al., 2004; Habibi et al., 2014). The primary result of this work is that buckling can occur in four distinct modes (viscous, gravitational, inertio-gravitational, and inertial) depending on the force that balances the viscous resistance to bending as a function of fall height.

With the exception of Griffiths and Turner (1988), all the studies cited above consider ‘non-immersed’ folding/coiling that occurs when the influence of the external fluid (typically air in experiments) is negligible. Recently, Cubaud and Mason (2006a) have studied the immersed buckling that occurs when two fluids with different viscosities are in-

jected into a diverging microchannel. Their experimental setup with $h = 100\mu\text{m}$ is shown in Fig. 1.5. The thread is produced by hydrodynamic focusing of a viscous fluid flow by a less viscous fluid injected from the sides. Silicone oils with different viscosities were used to obtain different viscosity ratios. Fig. 1.6 shows the viscous folding for different divergence angles and flow rate ratios. On the basis of their experimental results, Cubaud and Mason (2006a) proposed that $f \sim \dot{\gamma}$, where f is the folding frequency and $\dot{\gamma} = U_1/(h/2)$ is the characteristic shear rate. The thread of radius R_1 can be assumed to flow at nearly constant velocity, $U_1 = Q_1/(\pi R_1^2)$, like a solid plug, inside a sheath of the less viscous liquid, similar to the flow in a circular channel. In this case, U_1 represents the maximum velocity of the surrounding liquid. Downstream, the thread and surrounding liquid enter the diverging channel creating a decelerating extensional flow in Fig. 1.5. Extensional viscous stresses cause the thread to bend and fold, rather than dilate, in order to minimize dissipation and conserve mass. As the thread folds, it reduces its velocity and mixes with the outer liquid. In addition to folding, many other potentially useful flow phenomena are obtained, including oscillatory folding, folding modified by strong diffusion, heterogeneous folding, and subfolding (Cubaud and Mason, 2006b).

To our knowledge, the only existing numerical study of immersed buckling is Chung et al. (2010), who performed numerical and experimental studies on viscous folding in diverging microchannels similar to those of Cubaud and Mason (2006a). However, it is important to note that the numerical simulations of Chung et al. (2010) are two-dimensional, unlike their or Cubaud's experiments which are fully three-dimensional. Chung et al. (2010) obtained a regime diagram for the flow pattern observed (stable, folding, or chaotic) as a function of the flow rate ratio, the viscosity ratio, and the channel shape, as shown in Fig. 1.7. In addition to the divergence angles $\alpha = \pi/2$ and $\alpha = \pi$, Chung

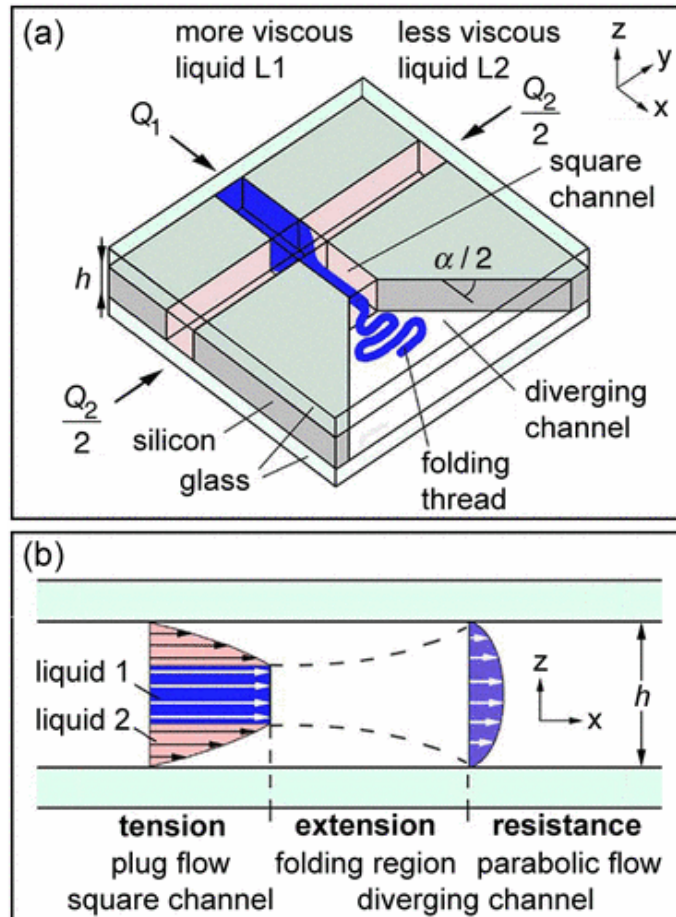


Figure 1.5: Schematic diagram of Cubaud's experimental setup. (a) Diverging microchannel module (height, $h = 100\mu\text{m}$). Simultaneous injection of liquid 1 (more viscous) and liquid 2 (less viscous) produces a thread of liquid 1 in the square channel. The thread enters a diverging channel with opening angle α . (b) Flow profiles during the folding instability (side view). Arrows indicate velocities.

et al. (2010) also performed simulations for a channel with walls of hyperbolic shape, to obtain a more uniform compressive stress along the channel's centerline. The hyperbolic channel generated folding flows with smaller frequency and amplitude, as well as a delay of onset of the folding. From their numerical results, Chung et al. (2010) obtained a power-law relation $f \sim \dot{\gamma}^{1.68}$, which is quite different from Cubaud and Mason's law $f \sim \dot{\gamma}$.

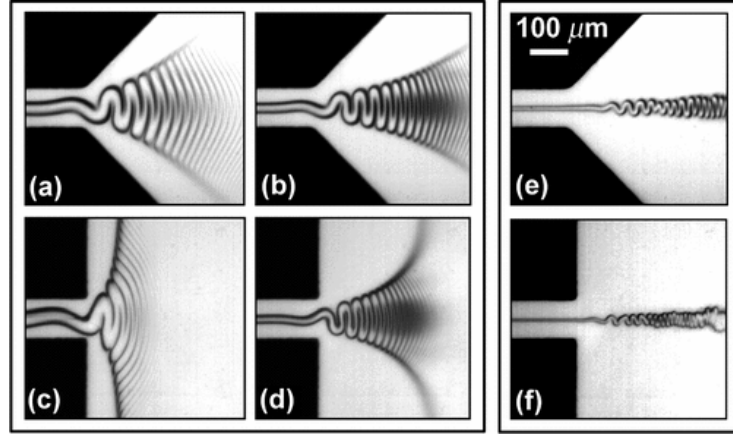


Figure 1.6: Viscous folding of a thread in diverging microchannels for different channel angles and flow rate ratios. The viscosities are fixed at $\eta_1 = 500\text{cP}$ and $\eta_2 = 6\text{cP}$ ($\chi = 83$). (a)-(d) The thread flow rate is fixed at $Q_1 = 5\mu\text{ l/min}$. (a) $\phi = Q_1/Q_2 = 0.4$, $\alpha = \pi/2$. (b) $\phi = 0.2$, $\alpha = \pi/2$. (c) $\phi = 0.4$, $\alpha = \pi$. (d) $\phi = 0.2$, $\alpha = \pi$. (e) $\phi = 0.03$ ($Q_1 = 1\mu\text{l/min}$), $\alpha = \pi/2$. (f) $\phi = 0.02$ ($Q_1 = 1\mu\text{l/min}$), $\alpha = \pi$ (Figure from (Cubaud and Mason, 2006a)).

The different power-law relations obtained by Chung et al. (2010) and Cubaud and Mason (2006a) may be due to the different dimensionalities of the simulations and the experiments, suggesting that fully three-dimensional simulations are justified. To this end, we will use

the parallel code BLUE for multiphase flow based on the front tracking method (developed by Shin, Chergui, and Juric (2014)) to simulate three-dimensional viscous folding in diverging microchannels.

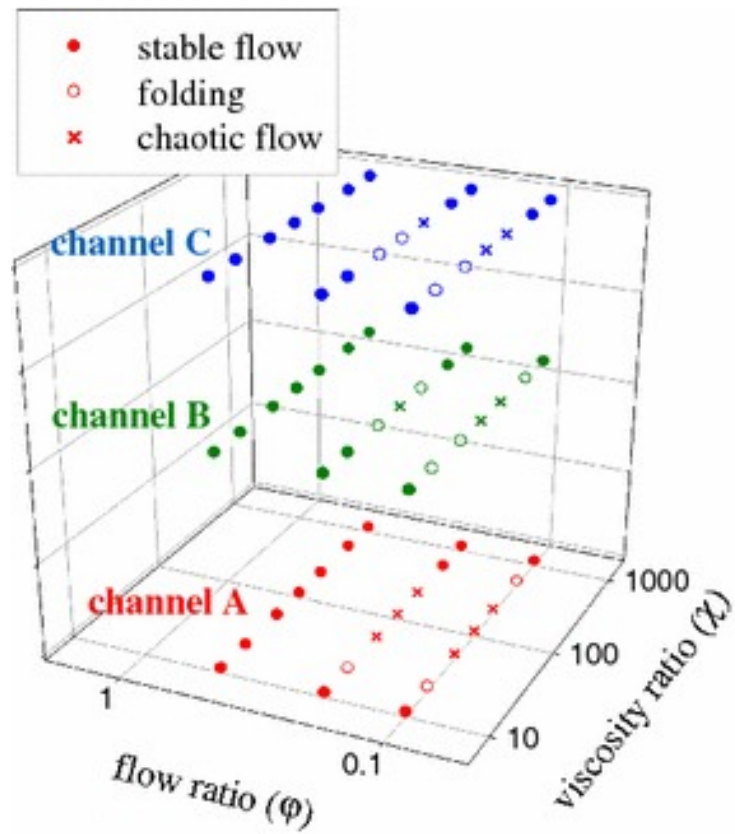


Figure 1.7: Regime diagram for two-dimensional flow patterns in diverging channels as functions of the flow ratio ϕ , the viscosity ratio χ , and the channel shape (Chung et al., 2010). Channel A has opening angle $\alpha = 180^\circ$, channel B has $\alpha = 90^\circ$, and channel C has walls of hyperbolic shape.

Chapter 2

Thin Newtonian sheets: The discrete approach

In this chapter we build a numerical model for the subduction of a thin viscous sheet. The model has four parts: the thin-sheet theory, a Lagrangian description of the sheet's geometry and kinematics; a boundary integral representation for the flow inside and outside the sheet; and a discrete (as opposed to smooth) formulation of the thin viscous sheet equations simplified from Audoly et al. (2013)'s discrete approach for thin viscous threads.

2.1 Thin-sheet theory: essential concepts

Because our subduction model involves a thin viscous sheet, we summarize here the essential concepts of thin-sheet theory (Ribe, 2001) in Fig. 2.1. At each point on the sheet, let \mathbf{d}_1 be the tangent vector to the sheet's midsurface, \mathbf{d}_2 the unit normal to the midsurface, and \mathbf{d}_3 the unit vector pointing out of the page. The Cartesian coordinates of the midsurface are $\mathbf{x}_0(s)$, and those of an arbitrary point on the sheet

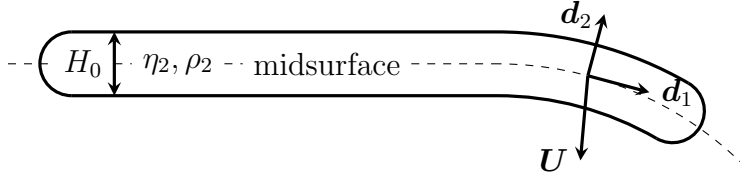


Figure 2.1: A viscous thin sheet

are $\mathbf{x}(s, z) \equiv \mathbf{x}_0(s) + z\mathbf{d}_2$, $(-H/2 \leq z \leq H/2)$, where H is the sheets thickness. Let the inclination of the midsurface to the horizontal be $\theta(s)$, and the curvature of the midsurface be $K(s) \equiv \partial\theta/\partial s$. The balance of forces and moments on an element of the sheet requires

$$\mathbf{N}' + \rho\mathbf{g}h + \mathbf{F} = 0, \quad \mathbf{M}' + \mathbf{d}_1 \times \mathbf{N} = 0, \quad (2.1)$$

where \mathbf{F} is the traction applied by the outer fluid and the prime denotes differentiation with respect to s . The stress resultant $\mathbf{N} \equiv N_1\mathbf{d}_1 + N_2\mathbf{d}_2$ and the bending moment $\mathbf{M} \equiv M\mathbf{d}_3$ are

$$\mathbf{N} = \int_{-H/2}^{H/2} \boldsymbol{\sigma} \cdot \mathbf{d}_1 \, dz, \quad \mathbf{M} = \int_{-H/2}^{H/2} z\mathbf{d}_1 \times \boldsymbol{\sigma} \, dz. \quad (2.2)$$

Let the velocity of the sheet's midsurface be

$$\mathbf{U} = U\mathbf{d}_1 + W\mathbf{d}_2. \quad (2.3)$$

The equations that describe the low Reynolds number flow of a curved two-dimensional sheet are

$$\frac{\partial u}{\partial s} + \frac{\partial}{\partial z}(hw) = 0, \quad (2.4)$$

$$\frac{\partial \sigma_{ss}}{\partial s} + \frac{\partial}{\partial z}(h\sigma_{zs}) + \sigma_{zs} \frac{\partial h}{\partial z} = 0, \quad (2.5)$$

$$\frac{\partial}{\partial z}(h\sigma_{zz}) + \frac{\partial \sigma_{zs}}{\partial s} - \sigma_{ss} \frac{\partial h}{\partial z} = 0, \quad (2.6)$$

where σ_{ij} is the stress tensor and $h = 1 - zK$. The components of the stress tensor are related to the velocity by

$$\sigma_{ss} = -p + \frac{2\eta_2}{h} \left(\frac{\partial u}{\partial s} - Kw \right), \quad (2.7)$$

$$\sigma_{zz} = -p + 2\eta_2 \frac{\partial w}{\partial z}, \quad (2.8)$$

$$\sigma_{zs} = \eta_2 \left[\frac{1}{h} \frac{\partial w}{\partial s} + h \frac{\partial}{\partial z} \left(\frac{u}{h} \right) \right]. \quad (2.9)$$

Now because the sheet is thin, the components σ_{sz} , σ_{zz} are small compared to the remaining component σ_{ss} . We can therefore set

$$\sigma_{sz} = \sigma_{zz} = 0. \quad (2.10)$$

From the equations (2.8), (2.9) and (2.10),

$$h \frac{\partial}{\partial z} \left(\frac{u}{h} \right) = -\frac{1}{h} \frac{\partial w}{\partial s}, \quad p = 2\eta_2 \frac{\partial w}{\partial z}. \quad (2.11)$$

According to the continuity equation,

$$\frac{\partial w}{\partial z} = -\frac{1}{h} \left(\frac{\partial u}{\partial s} - Kw \right) \approx -\frac{1}{h} \left(\frac{\partial u}{\partial s} - KW \right) \quad (2.12)$$

Considering the sheet is very thin, it is assumed that the velocity w varies little along the z -direction, i.e. $\partial w/\partial z = \partial W/\partial z$. Thus, the first equation in (2.11) becomes

$$h \frac{\partial}{\partial z} \left(\frac{u}{h} \right) = -\frac{1}{h} \frac{\partial W}{\partial s}. \quad (2.13)$$

By integration of the equation (2.13), the velocity u is therefore

$$u = -\frac{1}{K} \frac{\partial W}{\partial s} + C_2 h. \quad (2.14)$$

When $z = 0$, the equation (2.14) gives the velocity on the midsurface $U(s) = -K^{-1} \partial W/\partial s + C_2$, so we can obtain $C_2 = -U(s) + K^{-1} \partial W/\partial s$. Thus, the velocity u is approximately

$$\mathbf{u} = \mathbf{U} - z(\Delta \mathbf{d}_2 + \omega \mathbf{d}_1), \quad (2.15)$$

where

$$\Delta = \frac{\partial U}{\partial s} - KW, \quad \omega = \frac{\partial W}{\partial s} + KU, \quad (2.16)$$

are the stretching rate and rotation rate of the midsurface, respectively.

The constitutive relations for N_1 and M are

$$N_1 = 4\eta H \Delta, \quad (2.17)$$

$$M = -\frac{1}{3}\eta H^3 \omega'. \quad (2.18)$$

There is no constitutive relations for N_2 , which is small and must be determined by solving the equilibrium equations.

2.2 Lagrangian description of a thin sheet

It is convenient to express the variables of a thin sheet in a Lagrangian framework. Let t be the time, and S be the Lagrangian coordinate along the midsurface at the initial time $t = 0$. For any variable $f(S, t)$, its spatial derivative is denoted by a prime,

$$f' = \frac{\partial f(S, t)}{\partial S}, \quad (2.19)$$

and its time derivative by a dot,

$$\dot{f}(S, t) = \frac{\partial f(S, t)}{\partial t}. \quad (2.20)$$

Let the midsurface of the sheet be $\mathbf{X}(S, t)$. The material tangent $\mathbf{T}(S, t)$ is defined by

$$\mathbf{T}(S, t) = \mathbf{X}'(S, t). \quad (2.21)$$

The norm of $\mathbf{T}(S, t)$ measures the amount of stretching of the centerline with respect to the reference configuration, and is used to define the unit

tangent \mathbf{t} of the centerline as

$$l(S, t) = |\mathbf{T}(S, t)|, \quad (2.22)$$

$$\mathbf{t}(S, t) = \frac{\mathbf{T}(S, t)}{l(S, t)}. \quad (2.23)$$

Then the Lagrangian axial stretching strain rate d is defined by

$$d(S, t) = \frac{\partial l(S, t)}{\partial t}. \quad (2.24)$$

In the Lagrangian framework the velocity \mathbf{U} is the time derivative of position:

$$\mathbf{U}(S, t) = \frac{\partial \mathbf{X}(S, t)}{\partial t}. \quad (2.25)$$

A kinematic relation between the stretching strain rate $d(S, t)$ and the velocity $\mathbf{U}(S, t)$ is:

$$\begin{aligned} d(S, t) &= \frac{\partial l(S, t)}{\partial t} = \frac{1}{2l} \frac{\partial (l^2)}{\partial t} = \frac{1}{2l} \frac{\partial (\mathbf{T}^2)}{\partial t} \\ &= \frac{1}{l} \mathbf{T} \cdot \frac{\partial \mathbf{T}}{\partial t} = \mathbf{t}(S, t) \cdot \frac{\partial \mathbf{U}(S, t)}{\partial S}. \end{aligned} \quad (2.26)$$

To describe the bending of the sheet, an orthonormal triad of vectors $\mathbf{d}_1(S, t)$, $\mathbf{d}_2(S, t)$, $\mathbf{d}_3(S, t)$ is introduced. The unit tangent vector \mathbf{t} is identified with $\mathbf{d}_1(S, t)$, $\mathbf{d}_2(S, t)$ is the unit normal vector, and $\mathbf{d}_3(S, t)$ is a unit vector perpendicular to the sheet. The rate of change of the vectors \mathbf{d}_i are

$$\frac{\partial \mathbf{d}_i(S, t)}{\partial t} = \boldsymbol{\omega}(S, t) \times \mathbf{d}_i(S, t) \quad (2.27)$$

where $\boldsymbol{\omega}$ is the Darboux vector (angular velocity vector). Similarly, there is a second Darboux vector with respect to the space derivative:

$$\frac{\partial \mathbf{d}_i(S, t)}{\partial S} = \boldsymbol{\pi}(S, t) \times \mathbf{d}_i(S, t) \quad (2.28)$$

The relation between $\boldsymbol{\omega}$ and $\boldsymbol{\pi}$ is known as the Maurer-Cartan identity:

$$\frac{\partial \boldsymbol{\omega}(S, t)}{\partial S} = \frac{\partial \boldsymbol{\pi}(S, t)}{\partial t} - \boldsymbol{\omega}(S, t) \times \boldsymbol{\pi}(S, t) \quad (2.29)$$

The rotational strain rate can be written in terms of the first Darboux vector $\boldsymbol{\omega}$ as

$$\boldsymbol{e}(S, t) = \frac{\partial \boldsymbol{\omega}(S, t)}{\partial S} \quad (2.30)$$

The vector \boldsymbol{e} describes the rates of rotational deformation by bending and twisting. For the 2-D sheet, there is no twisting but only bending around the vector \boldsymbol{d}_3 , i.e. the axis \boldsymbol{a}_3 (always $\boldsymbol{a}_3 = \boldsymbol{d}_3$ in this case):

$$\boldsymbol{\omega}(S, t) = \omega \boldsymbol{a}_3, \quad \boldsymbol{e}(S, t) = e \boldsymbol{a}_3 \quad (2.31)$$

$$\boldsymbol{e}_b(S, t) = \boldsymbol{e}(S, t) = \frac{\partial \boldsymbol{\omega}(S, t)}{\partial S} \quad (2.32)$$

where \boldsymbol{e}_b is the bending strain rate.

Also, a simple explicit expression for the angular velocity for a 2-D sheet can be obtained:

$$\boldsymbol{\omega}(S, t) = \boldsymbol{t}(S, t) \times \dot{\boldsymbol{t}}(S, t) \quad (2.33)$$

Equation (2.33) involves the time derivative of the unit tangent vector which can be derived from the permutation of derivatives with respect to t and S :

$$\dot{\boldsymbol{T}} = \frac{\partial}{\partial t} \left(\frac{\partial \boldsymbol{X}}{\partial S} \right) = \frac{\partial}{\partial S} \left(\frac{\partial \boldsymbol{X}}{\partial t} \right) = \boldsymbol{U}'. \quad (2.34)$$

At the same time, according to equation (2.23) we have $\dot{\boldsymbol{T}} = l\dot{\boldsymbol{t}} + \dot{l}\boldsymbol{t}$, whence the following relation is found:

$$l\dot{\boldsymbol{t}} + \dot{l}\boldsymbol{t} = \boldsymbol{U}' \quad (2.35)$$

Expanding the cross product with \boldsymbol{t} , the angular velocity for a 2-D sheet becomes

$$\boldsymbol{\omega} = \boldsymbol{t} \times \dot{\boldsymbol{t}} = \frac{1}{l} \boldsymbol{t} \times (l\dot{\boldsymbol{t}}) = \frac{1}{l} \boldsymbol{t} \times (l\dot{\boldsymbol{t}} + \dot{l}\boldsymbol{t}) = \frac{1}{l} \boldsymbol{t} \times \boldsymbol{U}' \quad (2.36)$$

In the Lagrangian framework, the internal viscous stress in the sheet can be described by a Rayleigh dissipation potential, Torby (1984). This potential has three contributions, corresponding to the stretching, bending and twisting modes of deformation. The utility of the Rayleigh potential \mathcal{D} is that the net viscous force can be obtained by differentiation with respect to the velocity. Thus the resultant of the internal viscous stress on the midsurface is

$$\mathbf{P}(S, t) = -\frac{\partial \mathcal{D}(S, t)}{\partial \mathbf{U}(S, t)}. \quad (2.37)$$

Note that the quantity \mathbf{P} is the net resultant per unit length dS in the Lagrangian configuration. The expression of the dissipation potential in terms of the above kinematic variables will be derived in the following chapter for Newtonian fluid.

The forces acting on the sheet are the internal viscous forces, gravity, and the tractions applied by the outer fluid. Finally, the force balance per unit length dS for a thin viscous sheet in the Lagrangian description is

$$\mathbf{P} + \mathbf{g}lh\delta\rho + \mathbf{f}_1^+ + \mathbf{f}_1^- = 0, \quad (2.38)$$

where \mathbf{f}_1^\pm are the tractions exerted on the surfaces $z = \pm h/2$ by the external fluid and \mathbf{g} is the gravitational acceleration.

2.3 Boundary-integral equation for an immersed fluid sheet

Let V_1 and V_2 be the volumes occupied by fluids 1 and 2, respectively, and let C be the interface between them. The general integral represen-

tations for the flows in fluids 1 and 2 are (Ladyzhenskaya (1963)):

$$-\frac{1}{\eta_1} \int_C \mathbf{f}_1(\mathbf{y}) \cdot \mathbf{J}(\mathbf{y} - \mathbf{x}) d\ell(\mathbf{y}) + \int_C \mathbf{u}_1(\mathbf{y}) \cdot \mathbf{K}(\mathbf{y} - \mathbf{x}) \cdot \mathbf{n}(\mathbf{y}) d\ell(\mathbf{y}) = \chi_1(\mathbf{x}) \mathbf{u}_1(\mathbf{x}), \quad (2.39)$$

$$\frac{1}{\eta_2} \int_C \mathbf{f}_2(\mathbf{y}) \cdot \mathbf{J}(\mathbf{y} - \mathbf{x}) d\ell(\mathbf{y}) - \int_C \mathbf{u}_2(\mathbf{y}) \cdot \mathbf{K}(\mathbf{y} - \mathbf{x}) \cdot \mathbf{n}(\mathbf{y}) d\ell(\mathbf{y}) = \chi_2(\mathbf{x}) \mathbf{u}_2(\mathbf{x}), \quad (2.40)$$

where \mathbf{J} and \mathbf{K} are the velocity and stress Green functions for Stokes flow satisfying the relevant boundary conditions which will be discussed in more detail in the next chapter. Let $\chi_1(\mathbf{x}) = 1, 1/2$ or 0 if \mathbf{x} is in V_1 , right on the contour, or in V_2 , respectively, and define $\chi_2(\mathbf{x})$ similarly with the subscripts 1 and 2 interchanged. The unit normal vector \mathbf{n} is directed out of fluid 2 and into fluid 1.

On the contour C , the velocity is continuous while the modified normal stress undergoes a jump proportional to the difference of the densities of the two fluids. Symbolically,

$$\mathbf{u}_1 = \mathbf{u}_2, \quad (2.41)$$

$$\mathbf{f}_2(\mathbf{y}) = \mathbf{f}_1(\mathbf{y}) + \delta\rho(\mathbf{g} \cdot \mathbf{y})\mathbf{n}. \quad (2.42)$$

Now add (2.39) and (2.40) and use the matching condition (2.41) to obtain

$$\chi_1(\mathbf{x}) \mathbf{u}_1(\mathbf{x}) + \chi_2(\mathbf{x}) \mathbf{u}_2(\mathbf{x}) = \int_C \left(\frac{\mathbf{f}_2}{\eta_2} - \frac{\mathbf{f}_1}{\eta_1} \right) \cdot \mathbf{J}(\mathbf{y} - \mathbf{x}) d\ell. \quad (2.43)$$

Then apply (2.42) to obtain

$$\begin{aligned} & \chi_1(\mathbf{x}) \mathbf{u}_1(\mathbf{x}) + \chi_2(\mathbf{x}) \mathbf{u}_2(\mathbf{x}) \\ &= \frac{1-\gamma}{\eta_2} \int_C \mathbf{f}_1 \cdot \mathbf{J}(\mathbf{y} - \mathbf{x}) d\ell + \frac{\delta\rho}{\eta_2} \int_C (\mathbf{g} \cdot \mathbf{y}) \mathbf{n} \cdot \mathbf{J}(\mathbf{y} - \mathbf{x}) d\ell. \end{aligned} \quad (2.44)$$

Evaluate on the midsurface $\mathbf{x} = \mathbf{X}$ to obtain

$$U(\mathbf{X}) = \frac{1-\gamma}{\eta_2} \int_C \mathbf{f}_1 \cdot \mathbf{J}(\mathbf{y} - \mathbf{X}) d\ell + \frac{\delta\rho}{\eta_2} \int_C (\mathbf{g} \cdot \mathbf{y}) \mathbf{n} \cdot \mathbf{J}(\mathbf{y} - \mathbf{X}) d\ell. \quad (2.45)$$

To simplify the first integral in (2.45), we note that in the limit $\epsilon \rightarrow 0$ the kernel $\mathbf{J}(\mathbf{y} - \mathbf{X})$ on both the upper and lower surfaces of the sheet is approximately equal to its value $\mathbf{J}(\mathbf{y} - \mathbf{X})$ on the sheet's midsurface. Ignoring the small regions of size $O(h)$ near the ends of the sheet, we may write

$$\begin{aligned} \int_C \mathbf{f}_1 \cdot \mathbf{J}(\mathbf{y} - \mathbf{x}) d\ell &\approx \int_{C_+} \mathbf{f}_+ \cdot \mathbf{J}(\mathbf{y} - \mathbf{X}) d\ell + \int_{C_-} \mathbf{f}_- \cdot \mathbf{J}(\mathbf{y} - \mathbf{X}) d\ell \\ &\approx \int_M (\mathbf{f}_+ + \mathbf{f}_-) \cdot \mathbf{J}(\mathbf{Y} - \mathbf{X}) d\ell \\ &\approx \int_0^L [\mathbf{f}_+(R) + \mathbf{f}_-(R)] \cdot \mathbf{J}(\mathbf{X}(R) - \mathbf{X}) dR \\ &= - \int_0^L [\mathbf{P} + lh\delta\rho\mathbf{g}] \cdot \mathbf{J}(\mathbf{X}(R) - \mathbf{X}) dR \end{aligned} \quad (2.46)$$

where R is a dummy Lagrangian variable of integration along the midsurface and the thin-sheet force balance (2.38) has been used in the last step.

To simplify the second integral in (2.45), we convert it to a surface integral using the divergence theorem and expand the derivative under the integral sign to obtain

$$\begin{aligned} \int_C (\mathbf{g} \cdot \mathbf{y}) \mathbf{n} \cdot \mathbf{J}(\mathbf{y} - \mathbf{X}) d\ell &= \int_S \mathbf{g} \cdot \mathbf{J}(\mathbf{y} - \mathbf{X}) dA \\ &\quad + \int_S (\mathbf{g} \cdot \mathbf{y}) \nabla \cdot \mathbf{J}(\mathbf{y} - \mathbf{X}) dA. \end{aligned} \quad (2.47)$$

In the thin-sheet limit $\epsilon \rightarrow 0$, the second integral on the right side of (2.47) is asymptotically small relative to the first, which moreover can

be approximated as an integral along the midsurface over a distribution of Stokeslets with density $lh\mathbf{g}$ per unit length dR . We therefore obtain

$$\begin{aligned} \int_C (\mathbf{g} \cdot \mathbf{y}) \mathbf{n} \cdot \mathbf{J}(\mathbf{y} - \mathbf{X}) d\ell &\approx \int_M h\mathbf{g} \cdot \mathbf{J}(\mathbf{Y} - \mathbf{X}) d\ell \\ &\approx \int_0^L lh\mathbf{g} \cdot \mathbf{J}(\mathbf{X}(R) - \mathbf{X}) dR. \end{aligned} \quad (2.48)$$

Substituting (2.46) and (2.48) into (2.45), we obtain a hybrid boundary-integral/thin-sheet ('BITS') equation

$$\mathbf{U}(S) = \frac{1}{\eta_2} \int_0^L [\gamma l h \delta \rho + (\gamma - 1) \mathbf{P}(R)] \cdot \mathbf{J}(\mathbf{X}(R) - \mathbf{X}(S)) dR \quad (2.49)$$

Now we can nondimensionalize all the equations using the initial plate thickness H_0 as the length scale, $H_0^2 g \delta \rho / \eta_1$ as the velocity scale, and $\eta_1 / H_0 g \delta \rho$ as the time scale. The dimensionless form of the integral equation (2.49) is

$$\begin{aligned} \mathbf{U}(S) = \frac{\gamma - 1}{\gamma} \int_0^{L/H_0} \mathbf{P}(R) \cdot \mathbf{J}(\mathbf{X}(R) - \mathbf{X}(S)) dR \\ + \int_0^{L/H_0} l(R) h(R) \mathbf{e}_2 \cdot \mathbf{J}(\mathbf{X}(R) - \mathbf{X}(S)) dR \end{aligned} \quad (2.50)$$

It is noted that in the equation (2.50) the first integral vanishes when the two fluids have the same viscosity, in which case the flow is just the sum of Stokeslets distributed along the sheet's midsurface. When $\gamma > 1$, the first integral takes account of the viscous forces acting on cross-sections of the sheet.

2.4 The discrete viscous thin sheet model

In this section, discrete forms of the smooth equations discussed above are introduced, using concepts from discrete differential geometry developed by Audoly et al. (2013).

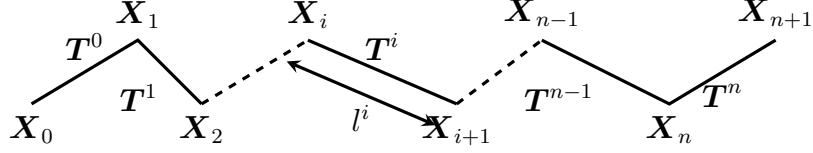


Figure 2.2: Discrete representation of the sheet's centerline as a polygonal curve with $n+2$ vertices and $n+1$ edges. Subscripts and superscripts denote variables that are defined on vertices and edges, respectively.

The first step is to represent the sheet's midsurface by a collection of discrete vertices and connecting edges, as shown in Fig. 2.2. The positions of the $(n+2)$ vertices are $\mathbf{X}_0(t), \mathbf{X}_1(t), \dots, \mathbf{X}_{n+1}(t)$. The material tangent \mathbf{T} becomes the segments between the vertices $\mathbf{T}^0(t), \mathbf{T}^1(t), \dots, \mathbf{T}^n(t)$,

$$\mathbf{T}^i(t) = \mathbf{X}_{i+1}(t) - \mathbf{X}_i(t). \quad (2.51)$$

Here and henceforth, subscripts and superscripts denote variables that are defined on vertices and edges, respectively.

The discrete segment length and unit tangent analogous to equations (2.22) and (2.23) are

$$l^i(t) = |\mathbf{T}^i(t)|, \quad (2.52)$$

$$\mathbf{t}^i(t) = \frac{\mathbf{T}^i(t)}{l^i(t)}. \quad (2.53)$$

The velocities of the vertices are the time derivatives of the positions, or

$$\mathbf{U}_i(t) = \frac{\partial \mathbf{X}_i(t)}{\partial t}. \quad (2.54)$$

In terms of the discrete variables, the discrete axial stretching strain rate for the segment \mathbf{T}^i is

$$d^i(t) = \frac{dl^i(t)}{dt} = \mathbf{t}^i(t) \cdot (\mathbf{U}_{i+1}(t) - \mathbf{U}_i(t)). \quad (2.55)$$

Comparing with equation (2.26) in smooth case, we see that $d^i(t)$ is the integrated strain rate on the segment \mathbf{T}^i .

Similarly, the discrete analogue of (2.32) and (2.36) is the following expression for the discrete bending strain rate on an interior vertex \mathbf{X}_i ($1 \leq i \leq n$):

$$\mathbf{e}_i^b(t) = \boldsymbol{\omega}^i(t) - \boldsymbol{\omega}^{i-1}(t), \quad (2.56)$$

$$\boldsymbol{\omega}^i(t) = \mathbf{t}^i(t) \times \frac{\mathbf{U}_{i+1}(t) - \mathbf{U}_i(t)}{l^i(t)}. \quad (2.57)$$

Also, the discrete bending strain rate \mathbf{e}_i^b is an integrated form of the smooth bending strain rate $\mathbf{e}^b(S, t)$. Note that the bending strain rate on vertex \mathbf{X}_i involves the vertices \mathbf{X}_{i-1} , \mathbf{X}_i and \mathbf{X}_{i+1} . So when the bending strain rates on the vertices \mathbf{X}_0 and \mathbf{X}_{n+1} at the ends are calculated, extra vertices outside the sheet are necessary. These extra vertices are called ghost vertices, and are shown in Fig. 2.2. For the vertex \mathbf{X}_0 at the left end, we have:

$$\begin{aligned} \frac{\partial \mathbf{X}(S)}{\partial S} &= \frac{-3\mathbf{X}_0 + 4\mathbf{X}_1 - \mathbf{X}_2}{2\Delta S} + O(\Delta S)^2 \\ &= \frac{\mathbf{X}_1 - \mathbf{X}_{-1}}{2\Delta S} + O(\Delta S)^2. \end{aligned} \quad (2.58)$$

In equation (2.58), the first form is a one-sided difference approximation and the second form is the usual second-order centered approximation involving the ghost vertex. Thus, from the equation (2.58), the position of the ghost vertex at the left end is obtained:

$$\mathbf{X}_{-1} = 3\mathbf{X}_0 - 3\mathbf{X}_1 + \mathbf{X}_2. \quad (2.59)$$

By the same method, the velocity on the left-end ghost vertex is

$$\mathbf{U}_{-1} = 3\mathbf{U}_0 - 3\mathbf{U}_1 + \mathbf{U}_2. \quad (2.60)$$

Similar equations hold for the ghost vertex at the sheet's right end. With the ghost vertex \mathbf{X}_{-1} and its velocity \mathbf{U}_{-1} , the quantities \mathbf{t}^{-1} , l^{i-1} , $\boldsymbol{\omega}^{-1}$ on the ghost segment \mathbf{T}^{-1} are given as for the interior segments and then we can get the bending strain rate \mathbf{e}_0^b on vertex \mathbf{X}_0 by substituting $\boldsymbol{\omega}^{-1}$ into the equation (2.56).

Now, other geometrical quantities and the modulus involved in the dissipation potential will be discretized. Each segment \mathbf{T}^i carries an area A^i . This quantity is based on the initial segment length and thickness, and is conserved during a simulation in the Lagrangian framework. Thus, the thickness of each segment is:

$$H^i(t) = \frac{A^i}{l^i(t)}. \quad (2.61)$$

The length \tilde{l}_i on a given interior vertex is necessary later, and is defined as the average length of adjoining segments:

$$\tilde{l}_i(t) = \frac{l^{i-1}(t) + l^i(t)}{2} \quad (1 < i < n). \quad (2.62)$$

The tilde symbol means the variable based on a vertex is calculated from the average values on adjoining segments. Similarly, the area on a given vertex \mathbf{X}_i can be obtained as

$$\tilde{A}_0 = \frac{A^0}{2}, \quad \tilde{A}_i = \frac{A^{i-1} + A^i}{2}, \quad \tilde{A}_{n+1} = \frac{A^n}{2}. \quad (2.63)$$

By analogy with equation (2.37), the discrete net internal viscous resultant acting on the vertex \mathbf{X}_i is given by

$$\mathbf{P}_i(t) = -\frac{\partial \mathcal{D}(t)}{\partial \mathbf{U}_i(t)}. \quad (2.64)$$

Here, the net viscous resultant \mathbf{P}_i is the integral of the quantity \mathbf{P} in the smooth setting.

For convenience, all the positions and velocities on vertices are represented in the form of a matrix with the size $1 \times 3(n+2)$:

$$\underline{X}(t) = (\mathbf{X}_0(t), \mathbf{X}_1(t), \dots, \mathbf{X}_{n+1}(t)), \quad (2.65)$$

$$\underline{U}(t) = (\mathbf{U}_0(t), \mathbf{U}_1(t), \dots, \mathbf{U}_{n+1}(t)). \quad (2.66)$$

So the expressions of the strain rates and the angular velocity vector depending can be rewritten with \underline{X} and \underline{U} in matrix form. Moreover, they are linear with respect to the velocity \underline{U} , whence

$$d^i(t) = \mathcal{L}_s^i(\underline{X}, \underline{U}) = \underline{U} \cdot \underline{\mathcal{L}}_s^i(\underline{X}), \quad (2.67)$$

$$\mathbf{e}_i^b(t) = \underline{\mathcal{L}}_i^b(\underline{X}, \underline{U}) = \underline{U} \cdot \underline{\mathcal{L}}_i^b(\underline{X}), \quad (2.68)$$

$$\boldsymbol{\omega}^i(t) = \underline{\mathcal{W}}^i(\underline{X}, \underline{U}) = \underline{U} \cdot \underline{\mathcal{W}}^i(\underline{X}). \quad (2.69)$$

The size of the stretching strain rate matrix $\underline{\mathcal{L}}_s^i(\underline{X})$ is $3(n+2) \times 1$. The sizes of the bending strain rate matrix $\underline{\mathcal{L}}_i^b(\underline{X})$ and the angular velocity matrix $\underline{\mathcal{W}}^i(\underline{X})$ are both $3(n+2) \times 3$.

Since the stretching strain rate $d^i(t)$ only depends on the velocities \mathbf{U}_i and \mathbf{U}_{i+1} according to equation (2.55), the matrix $\underline{\mathcal{L}}_s^i(\underline{X})$ is sparse and has the form:

$$\underline{\mathcal{L}}_s^i(\underline{X}) = \begin{pmatrix} \underline{0} \\ \hat{\underline{\mathcal{L}}}_s^i(\underline{X}) \\ \underline{0} \end{pmatrix}, \quad \hat{\underline{\mathcal{L}}}_s^i(\underline{X}) = (-\mathbf{t}^i, \mathbf{t}^i)^T. \quad (2.70)$$

Here the matrix $\hat{\underline{\mathcal{L}}}_s^i(\underline{X})$, with the size 6×1 , is the non-zero submatrix in the matrix $\underline{\mathcal{L}}_s^i(\underline{X})$ corresponding to the velocities \mathbf{U}_i and \mathbf{U}_{i+1} .

Similarly, in view of equations (2.56) and (2.57), the matrix $\underline{\mathcal{L}}_i^b(\underline{X})$

and $\underline{\underline{\mathcal{W}}}^i(\underline{\underline{X}})$ can be represented in the sparse matrix form

$$\underline{\underline{\mathcal{W}}}^i(\underline{\underline{X}}) = \begin{pmatrix} \underline{\underline{0}} \\ \underline{\underline{\hat{\mathcal{W}}}}^i(\underline{\underline{X}}) \\ \underline{\underline{0}} \end{pmatrix},$$

$$\underline{\underline{\hat{\mathcal{W}}}}^i(\underline{\underline{X}}) = \frac{1}{l^i} \begin{pmatrix} 0 & -t^i[3] & t^i[2] \\ t^i[3] & 0 & -t^i[1] \\ -t^i[2] & t^i[1] & 0 \\ 0 & t^i[3] & -t^i[2] \\ -t^i[3] & 0 & t^i[1] \\ t^i[2] & -t^i[1] & 0 \end{pmatrix}, \quad (2.71)$$

$$\underline{\underline{\mathcal{L}}}^b(\underline{\underline{X}}) = \begin{pmatrix} \underline{\underline{0}} \\ \underline{\underline{\hat{\mathcal{L}}}}^b(\underline{\underline{X}}) \\ \underline{\underline{0}} \end{pmatrix} = \underline{\underline{\mathcal{W}}}^i(\underline{\underline{X}}) - \underline{\underline{\mathcal{W}}}^{i-1}(\underline{\underline{X}}),$$

$$\underline{\underline{\hat{\mathcal{L}}}}^b(\underline{\underline{X}}) = \underline{\underline{\hat{\mathcal{W}}}}^i(\underline{\underline{X}}) - \underline{\underline{\hat{\mathcal{W}}}}^{i-1}(\underline{\underline{X}}). \quad (2.72)$$

The 6×3 non-zero submatrix $\underline{\underline{\hat{\mathcal{W}}}}^i(\underline{\underline{X}})$ corresponds to the velocities \mathbf{U}_i and \mathbf{U}_{i+1} . With the quantities on ghost vertices, the angular velocity

matrix outside the sheet can be evaluated as:

$$\underline{\hat{\mathcal{W}}}^{-1} = \frac{1}{l^{-1}} \begin{pmatrix} 0 & -2t^{-1}[3] & 2t^{-1}[2] \\ 2t^{-1}[3] & 0 & -2t^{-1}[1] \\ -2t^{-1}[2] & 2t^{-1}[1] & 0 \\ 0 & 3t^{-1}[3] & -3t^{-1}[2] \\ -3t^{-1}[3] & 0 & 3t^{-1}[1] \\ 3t^{-1}[2] & -3t^{-1}[1] & 0 \\ 0 & -t^{-1}[3] & t^{-1}[2] \\ t^{-1}[3] & 0 & -t^{-1}[1] \\ -t^{-1}[2] & t^{-1}[1] & 0 \end{pmatrix},$$

$$\underline{\hat{\mathcal{W}}}^{n+1} = \frac{1}{l^{n+1}} \begin{pmatrix} 0 & t^{n+1}[3] & -t^{n+1}[2] \\ -t^{n+1}[3] & 0 & t^{n+1}[1] \\ t^{n+1}[2] & -t^{n+1}[1] & 0 \\ 0 & -3t^{n+1}[3] & 3t^{n+1}[2] \\ 3t^{n+1}[3] & 0 & -3t^{n+1}[1] \\ -3t^{n+1}[2] & 3t^{n+1}[1] & 0 \\ 0 & 2t^{n+1}[3] & -2t^{n+1}[2] \\ -2t^{n+1}[3] & 0 & 2t^{n+1}[1] \\ 2t^{n+1}[2] & -2t^{n+1}[1] & 0 \end{pmatrix} \quad (2.73)$$

From the velocity on ghost vertices (2.60), $\underline{\hat{\mathcal{W}}}^{-1}$ and $\underline{\hat{\mathcal{W}}}^{n+1}$ are seen to depend on $(\mathbf{U}_0, \mathbf{U}_1, \mathbf{U}_2)$ and $(\mathbf{U}_{n-1}, \mathbf{U}_n, \mathbf{U}_{n+1})$ respectively. Thus, the submatrix $\underline{\hat{\mathcal{L}}}_i^b(\underline{X})$ involving three vertices $(i-1, i, i+1)$ has the size 9×3 ; the submatrices at the end vertices $\underline{\hat{\mathcal{L}}}_0^b(\underline{X})$ and $\underline{\hat{\mathcal{L}}}_{n+1}^b(\underline{X})$ with the same size 9×3 are one-side representations.

Now, the discrete internal viscous forces are arranged in matrix form \underline{P} and then related to the dissipation and velocity matrices according to equation (2.64):

$$\underline{P} = (\mathbf{P}_0(t), \mathbf{P}_1(t), \dots, \mathbf{P}_{n+1}(t)) = -\frac{\partial \mathcal{D}(t)}{\partial \underline{U}} \quad (2.74)$$

Thus, the discrete representation of the BITS equation (2.50) is:

$$\begin{aligned} \mathbf{U}_i &= \frac{\gamma - 1}{\gamma} \sum_{j=0}^{n+1} (\mathbf{P}_j \cdot \mathbf{J}_{ij}) + \sum_{j=0}^{n+1} ((\tilde{l}\tilde{H})_j \mathbf{e}_2 \cdot \mathbf{J}_{ij}) \\ &= \frac{\gamma - 1}{\gamma} \sum_{j=0}^{n+1} (\mathbf{P}_j \cdot \mathbf{J}_{ij}) + \sum_{j=0}^{n+1} (\tilde{A}_j \mathbf{e}_2 \cdot \mathbf{J}_{ij}) \end{aligned} \quad (2.75)$$

where the Green function $\mathbf{J}_{ij} = \mathbf{J}(\mathbf{X}_j - \mathbf{X}_i)$. Rewriting the discrete integral equation (2.75) in matrix form and substituting the net internal force (2.74), we obtain

$$\underline{U} \cdot \underline{\delta}_i - \frac{\gamma - 1}{\gamma} \underline{P} \cdot \underline{J}_i = \underline{A} \cdot \underline{J}_i \quad (2.76)$$

where, $\underline{\delta}_i = (\underline{0}, \underline{0}, \dots, \underline{I}, \dots, \underline{0})^T$, $\underline{J}_i = (\mathbf{J}_{i1}, \mathbf{J}_{i2}, \dots, \mathbf{J}_{i(n+1)})^T$ and $\underline{A} = (\tilde{A}_1 \mathbf{e}_2, \tilde{A}_2 \mathbf{e}_2, \dots, \tilde{A}_{n+1} \mathbf{e}_2)$.

Equation (2.76) is based on the vertex \mathbf{X}_i . Expanding it to all vertices yields the final matrix equation

$$\underline{U} - \frac{\gamma - 1}{\gamma} \underline{P} \cdot \underline{J} = \underline{A} \cdot \underline{J} \quad (2.77)$$

where $\underline{J} = (\underline{J}_1, \underline{J}_2, \dots, \underline{J}_{n+1})$. By solving the matrix equation (2.77), the velocities on all vertices can be obtained.

Chapter 3

Subduction of a Newtonian sheet

In this chapter we study the subduction of a thin sheet with Newtonian rheology, as shown in Fig. 3.1. The sheet has viscosity η_2 and density ρ_2 , and sinks freely into a horizontally infinite layer of fluid with viscosity $\eta_1 \equiv \eta_2/\gamma$ and density $\rho_1 \equiv \rho_2 - \delta\rho$. The flow domain is bounded above by an impermeable free-slip (zero shear stress) surface $x_2 = 0$, and extends infinitely in the \mathbf{e}_2 -direction. The model domain is two-dimensional, i.e. the sheet extends infinitely in the direction normal to the plane of the figure. The coordinates parallel to and normal to the sheet's midsurface are s and z , respectively. In Lagrangian description, the coordinate parallel to the midsurface can be presented as $s(S, t)$ and there is a relationship $s'(S, t) = l(S, t)$. The distance from the sheet surface to the free-slip surface is d , forming a 'lubrication layer'. According to a standard result from lubrication theory, normal stresses greatly exceed shear stresses within the lubrication layer. The plate is thus free to move horizontally, but its sinking is impeded by a strong upward directed normal stress whose value throughout the plates inte-

rior (away from the ends of the lubrication layer) is $Hg\delta r$ (Ribe, 2010). The lubrication layer can therefore be regarded simply as a mechanism for maintaining the plate in a state of perfect local isostatic equilibrium while allowing it to move freely in response to the pull of a freely deforming slab.

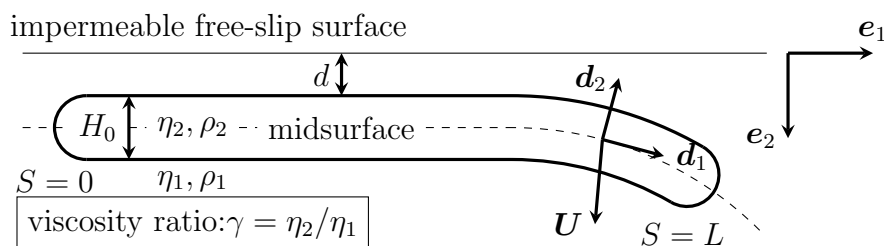


Figure 3.1: A thin sheet of viscous fluid immersed in a second fluid with a different viscosity.

3.1 Bending and stretching dissipation potentials of a Newtonian sheet

In the section 2.1, the essential thin-sheet theory has been presented. The velocity on the sheet can expressed by the velocity on the mid-surface:

$$u = -z \frac{\partial W}{\partial s} + Uh. \quad (3.1)$$

where $h = 1 - zK$. The remaining non-zero component of the stress tensor is defined as

$$\sigma_{ss} = \frac{4\eta_2}{h} \left(-z \frac{\partial^2 W}{\partial s^2} + h \frac{\partial U}{\partial s} - KW \right) = \frac{4\eta_2}{h} \left(\Delta - z \frac{\partial \omega}{\partial s} \right), \quad (3.2)$$

where Δ is the stretching rate, and $\frac{\partial \omega}{\partial s}$ is the bending rate.

The (rate of) dissipation potential per unit length of the sheet is

$$\phi(s) = \frac{1}{2} \int_{H/2}^{H/2} e_{ss} \sigma_{ss} dz \approx \frac{1}{2} \left[4\eta_2 H \Delta^2 + \frac{\eta_2 H^3}{3} (K\Delta - \partial\omega/\partial s)^2 \right]. \quad (3.3)$$

The first term in equation (3.3) is the stretching dissipation potential and the second term is the bending dissipation potential:

$$\phi_s(s) = \frac{1}{2} \cdot 4\eta_2 H \Delta^2, \quad (3.4)$$

$$\phi_b(s) = \frac{1}{2} \frac{\eta_2 H^3}{3} (K\Delta - \partial\omega/\partial s)^2 = \frac{1}{2} \frac{\eta_2 H^3}{3} \dot{K}^2. \quad (3.5)$$

$\partial\omega/\partial s - K\Delta$ is the curling rate on the midsurface, defined as the the rate of change of the midsurface curvature \dot{K} . The bending dissipation potential (3.5) suggests that the curling rate is a direct measure of the internal stresses that resist the bending of the sheet.

By analog to the theory of elasticity, the stretching dissipation potential can be written in the form $\phi_s = D\Delta^2/2$, where the stretching modulus D is

$$D = 4\eta_2 H. \quad (3.6)$$

Similarly, the bending dissipation potential can be defined as $\phi_b = B(\dot{K})^2/2$. Thus, the bending modulus B is

$$B = \frac{\eta_2 H^3}{3}. \quad (3.7)$$

Now we can transform the dissipation potential expression into the Lagrangian description, whereupon the stretching rate Δ becomes $d(S, t)$ and the bending rate \dot{K} becomes $e^b(S, t)$. The Rayleigh dissipation

potential of the whole sheet is

$$\mathcal{D}(t) = \mathcal{D}_s(t) + \mathcal{D}_b(t), \quad (3.8)$$

$$\mathcal{D}_s(t) = \int_0^L \frac{D(S,t)}{2l(S,t)} (d(S,t))^2 dS, \quad (3.9)$$

$$\mathcal{D}_b(t) = \int_0^L \frac{B(S,t)}{2l(S,t)} (e^b(S,t))^2 dS. \quad (3.10)$$

Here $D(S,t)$ and $B(S,t)$ are the Lagrangian stretching and bending moduli:

$$D(S,t) = 4\eta_2 H(S,t), \quad B(S,t) = 4\eta_2 I(S,t), \quad (3.11)$$

where $I(S,t) = (H(S,t))^3/12$ is the moment of inertia about an axis in the midsurface and in the \mathbf{d}_3 direction.

3.2 Numerical implementation

Based on the discrete geometrical quantities defined in 2.4, the discrete stretching and bending modulus $D_i(t)$ and $B_i(t)$ are respectively:

$$D^i(t) = 4\eta_2^i(t)H^i(t)/l^i, \quad (3.12)$$

$$B_i(t) = 4\left(\widetilde{\frac{\eta_2 I}{l}}\right)_i(t). \quad (3.13)$$

In (3.13) $\left(\widetilde{\frac{\eta_2 I}{l}}\right)_i$ is defined on a vertex as the average of the ones on adjoining segments:

$$\left(\widetilde{\frac{\eta_2 I}{l}}\right)_0 = \frac{\eta_2^0 I^0}{l^0}, \quad \left(\widetilde{\frac{\eta_2 I}{l}}\right)_i = \frac{1}{2} \left(\frac{\eta_2^{i-1} I^{i-1}}{l^{i-1}} + \frac{\eta_2^i I^i}{l^i} \right), \quad \left(\widetilde{\frac{\eta_2 I}{l}}\right)_{n+1} = \frac{\eta_2^n I^n}{l^n}, \quad (3.14)$$

$$I^i = \frac{(H^i)^3}{12}, \quad (3.15)$$

where I^i is the discrete moment of inertia. The dissipation potential can therefore be discretized as:

$$\mathcal{D}_s(t) = \frac{1}{2} \sum_{0 \leq i \leq n} D^i(t) (d^i(t))^2 \quad (3.16)$$

$$\mathcal{D}_b(t) = \frac{1}{2} \sum_{1 \leq i \leq n} B_i(t) (\mathbf{e}_i^b(t))^2 \quad (3.17)$$

The dissipation potential is a quadratic function of the velocity \underline{U} . It can therefore be represented by a symmetric matrix

$$\mathcal{D}(t) = \frac{1}{2} \underline{U} \cdot \underline{\mathcal{D}} \cdot \underline{U}, \quad (3.18)$$

$$\underline{\mathcal{D}} = \underline{\mathcal{D}}_s + \underline{\mathcal{D}}_b. \quad (3.19)$$

Explicit expressions for these contributions can be found by substituting the matrix representations (2.67)-(2.72) into the expressions (3.16) and (3.17) for the discrete dissipation potential:

$$\begin{aligned} \underline{\mathcal{D}}_s &= \sum_{0 \leq i \leq n} \underline{\mathcal{D}}_s^i = \sum_{0 \leq i \leq n} D^i(t) \underline{\mathcal{L}}_s^i \otimes \underline{\mathcal{L}}_s^i, \\ \underline{\mathcal{D}}_b &= \sum_{1 \leq i \leq n} \underline{\mathcal{D}}_b^i = \sum_{1 \leq i \leq n} B_i(t) \underline{\mathcal{L}}_i^b \cdot (\underline{\mathcal{L}}_i^b)^T, \end{aligned} \quad (3.20)$$

$$\underline{\mathcal{D}}_s^i = D^i(t) \begin{pmatrix} \underline{0} & \underline{0} & \underline{0} \\ \underline{0} & \hat{\underline{\mathcal{D}}}_s^i & \underline{0} \\ \underline{0} & \underline{0} & \underline{0} \end{pmatrix}, \quad \underline{\mathcal{D}}_b^i = B_i(t) \begin{pmatrix} \underline{0} & \underline{0} & \underline{0} \\ \underline{0} & \hat{\underline{\mathcal{D}}}_i^b & \underline{0} \\ \underline{0} & \underline{0} & \underline{0} \end{pmatrix}, \quad (3.21)$$

$$\hat{\underline{\mathcal{D}}}_s^i = \hat{\underline{\mathcal{L}}}_s^i \otimes \hat{\underline{\mathcal{L}}}_s^i, \quad \hat{\underline{\mathcal{D}}}_i^b = \hat{\underline{\mathcal{L}}}_i^b \cdot (\hat{\underline{\mathcal{L}}}_i^b)^T. \quad (3.22)$$

Since the potential contributions are in the sum of these sparse matrices $\underline{\mathcal{D}}_s^i$ and $\underline{\mathcal{D}}_b^i$ on each vertex or segment, the discrete stretching and bending potential matrices $\underline{\mathcal{D}}_s$ and $\underline{\mathcal{D}}_b$ are both band-diagonal. According to equations (2.70) and (3.22), the sparse matrix $\underline{\mathcal{D}}_s^i$ has a 6×6 non-zero

submatrix corresponding to the velocities \mathbf{U}_i and \mathbf{U}_{i+1} . By contrast, the bending potential $\underline{\underline{\mathcal{D}}}_i^b$ has a 9×9 non-zero submatrix corresponding to velocities at $\mathbf{X}_{i-1}, \mathbf{X}_i, \mathbf{X}_{i+1}$. The band structure of the potential matrices is shown in Fig. 3.2.

According to the equations (2.37) and (3.18), the matrix form of the viscous force \underline{P} can be simplified to

$$\underline{P} = -\frac{\partial \mathcal{D}(t)}{\partial \underline{U}} = -\underline{U} \cdot \underline{\underline{\mathcal{D}}} \quad (3.23)$$

Substituting the equation (3.23) into the discrete boundary integral thin sheet equation (2.77), we obtain the matrix equation for a Newtonian sheet:

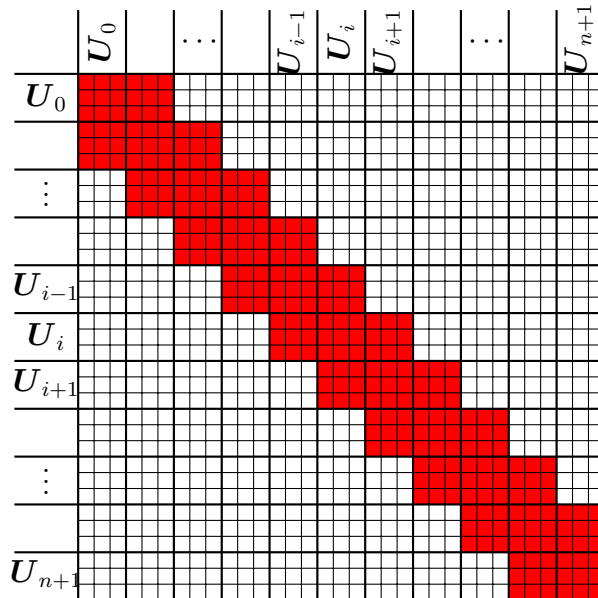
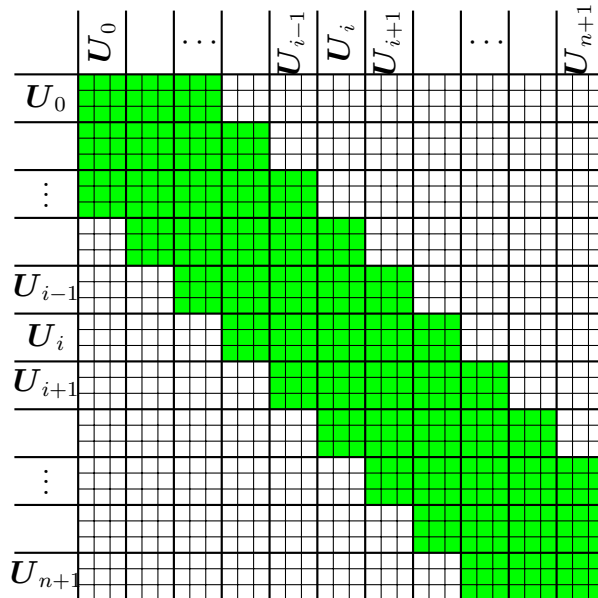
$$\underline{U} \cdot \left(\underline{I} + \frac{\gamma - 1}{\gamma} \underline{\underline{\mathcal{D}}} \cdot \underline{\underline{J}} \right) = \underline{A} \cdot \underline{J} \quad (3.24)$$

3.3 The Green's function for sheet subduction

For the geometry of Fig. 3.1, the free-slip surface (mirror symmetry) condition at $x_2 = 0$ can be automatically satisfied by adding to the infinite-fluid Green's function the corresponding Green's function for the image point located above the free surface. The resulting symmetrized form of \mathbf{J} no longer has a logarithmic singularity at $r \rightarrow \infty$, indicating that the presence of the boundary has resolved Stokes's paradox. The Green's function $\mathbf{J}_{ij} = \mathbf{J}(\mathbf{X}_j - \mathbf{X}_i)$ that satisfies the free-slip boundary conditions is

$$\begin{aligned} \mathbf{J}(\mathbf{X}_j - \mathbf{X}_i) &= J_{\alpha\beta}(\mathbf{X}_j - \mathbf{X}_i) \\ &= J_{\alpha\beta}^{(0)}(\mathbf{X}_j - \mathbf{X}_i) + (-1)^{\beta+1} J_{\alpha\beta}^{(0)}(\mathbf{X}_j + \mathbf{X}_i), \end{aligned} \quad (3.25)$$

$$J_{\alpha\beta}^{(0)}(\mathbf{r}) = \frac{1}{4\pi} \left(-\delta_{\alpha\beta} \ln r + \frac{r_\alpha r_\beta}{r^2} \right) \quad (3.26)$$

(a) $\underline{\underline{D}}_s$ for the stretching mode(b) $\underline{\underline{D}}_b$ for the bending modeFigure 3.2: Band structure of the dissipation matrices $\underline{\underline{D}}_s$ and $\underline{\underline{D}}_b$

where \mathbf{X}_i is the position of the point force, $-\mathbf{X}_i$ is the position of the image point force, $r = |\mathbf{r}|$, and $J_{\alpha\beta}^{(0)}$ is the Green's function for an infinite fluid.

In the discrete method, the value of the Green's function on the vertex is taken to be the average one near the node. The singular character of (3.25) when $i = j$ makes the equation (3.24) difficult to evaluate numerically. So to get the average Green's function near the singular point \mathbf{X}_i , the integral of the function $\mathbf{J}(\mathbf{X} - \mathbf{X}_i)$ is calculated near the vertex \mathbf{X}_i in the range $[\mathbf{X}_{i-1}, \mathbf{X}_{i+1}]$, and then the average value is obtained:

$$\mathbf{J}(\mathbf{X}_i - \mathbf{X}_i) = \frac{\int_{\mathbf{X}_{i-1}}^{\mathbf{X}_{i+1}} \mathbf{J}(\mathbf{X} - \mathbf{X}_i) d\mathbf{X}}{(l_{i-1} + l_i)}. \quad (3.27)$$

The integral is calculated using Gaussian quadrature, which avoids the singular point if the order of the quadrature is even.

An alternative method for handling the singularity is by using the regularized Stokeslet of Cortez (2001). Whereas the normal Stokeslet represents the flow due to a true point force, the regularized Stokeslet corresponds to the flow due to a force distributed over the interior of a small circle of radius ϵ according to

$$\mathbf{f}(\mathbf{x} - \mathbf{x}') = \frac{3\epsilon^3}{2\pi R^5} \mathbf{f}_0 \quad (3.28)$$

where $R = \sqrt{r^2 + \epsilon^2}$. A simple calculation shows that total (integrated over all space) magnitude of the force is \mathbf{f}_0 .

The explicit form of $J_{\alpha\beta}^{(0)}(\mathbf{r})$ is given by eqn. (10) of Cortez (2001), and is

$$J_{\alpha\beta}^{(0)}(\mathbf{r}) = \frac{1}{4\pi} \left[-\delta_{\alpha\beta} \ln(R + \epsilon) + \frac{R + 2\epsilon}{R(R + \epsilon)} \left(\epsilon \delta_{\alpha\beta} + \frac{r_\alpha r_\beta}{R + \epsilon} \right) \right] \quad (3.29)$$

Inspection shows that (3.29) reduces to (3.26) in the limit $\epsilon \rightarrow 0$. The regularized Green's function that satisfies the free-slip boundary conditions on $x_2 = 0$ is obtained by substituting (3.29) into (3.25).

3.4 Numerical solutions and analysis

First it is necessary to validate our boundary-integral/thin-sheet method (BITS) by comparing to the results of full boundary element method (BEM) calculations. The BEM code that we use is that of Ribe (2010). As a first test case, we consider a simple vertical sheet whose geometry is shown by the solid line in Fig. 3.3.

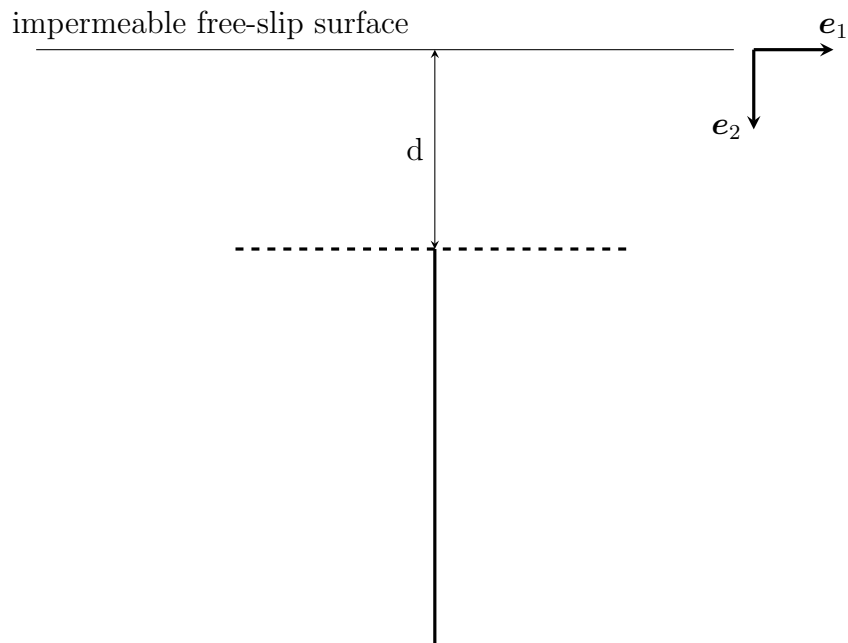


Figure 3.3: Geometry of the vertical (solid line) and horizontal (dashed line) sheets used to test the numerical BITS code.

3.4.1 Vertical sheet

By symmetry, a 2-D vertical sheet has only a single (vertical) component of velocity $U(s)$. As a test case, we use a sheet of length $L = 20H_0$ whose

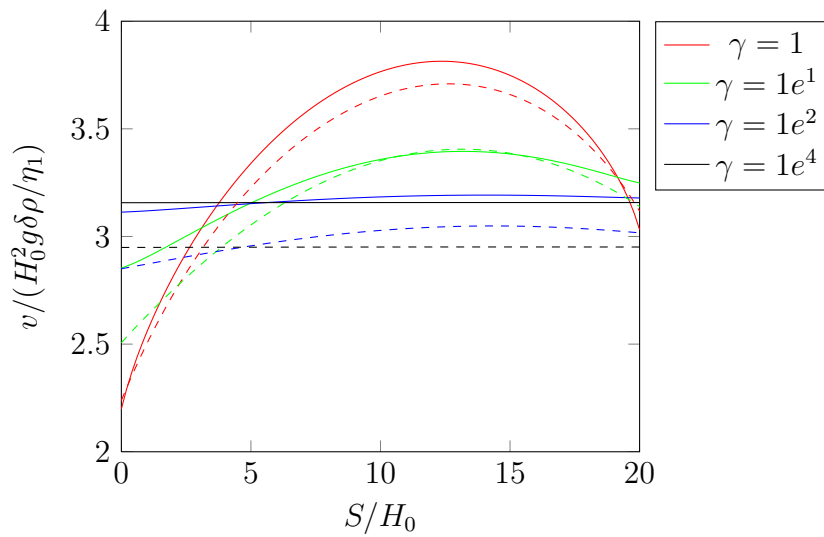


Figure 3.4: Velocity solutions for a vertical sheet at different viscosity ratios γ (BITS: solid line BEM: dashed line) with a length $L = 20H_0$ and a distance $d = 10H_0$ below the free surface

upper extremity is a distance $d = 10H_0$ below the free surface (Fig. 3.3). Fig. 3.4 shows $U(s)$ predicted by BITS for different viscosity ratios γ (solid lines) together with full BEM solutions (dashed lines). The agreement is reasonable, with errors up to 14%. In judging these results, it is important to remember that BITS is only accurate to $O(H_0/L)$, which is 0.05 in our test case. In each of the solutions for $\gamma \leq 10^2$, the slope changes sign somewhere on the sheet, indicating that the upper portion is in extension ($U'(S) > 0$) and the lower portion in compression ($U'(S) < 0$). Finally, for the largest viscosity ratio $\gamma = 10000$, the sheet behaves rigidly.

The BITS results in Fig. 3.4 were obtained using Gaussian quadrature to avoid the singular point. We now compare them with results obtained using regularized Stokeslets of different radii ϵ (Fig. 3.5). It is clear that the predictions converge to the Gaussian quadrature result as $\epsilon \rightarrow 0$.

Fig. 3.6 shows the effect of discretization number on the velocities of the vertical sheet. The geometry of the sheet is as shown in Fig. 3.3, and the viscosity contrast is $\gamma = 100$. Fig. 3.6a shows the results of the integral average method, and Fig. 3.6b shows the predictions of the regularized Stokeslet method. Both methods show good convergence, and $\delta S = 0.02H_0$ appears to be a reasonable choice.

3.4.2 Horizontal sheet

We now turn to the case of a horizontal sheet, the geometry of which is shown by the dashed line in Fig. 3.3. Fig. 3.7 shows the velocity vectors along the sheet for $\gamma = 10$ (Fig. 3.7(a)) and $\gamma = 10^5$ (Fig. 3.7(b)). In Fig. 3.7(a) the deformation is dominated by bending, and stretching is minor. In Fig. 3.7(b), the sheet behaves rigidly on account of the very large viscosity ratio.

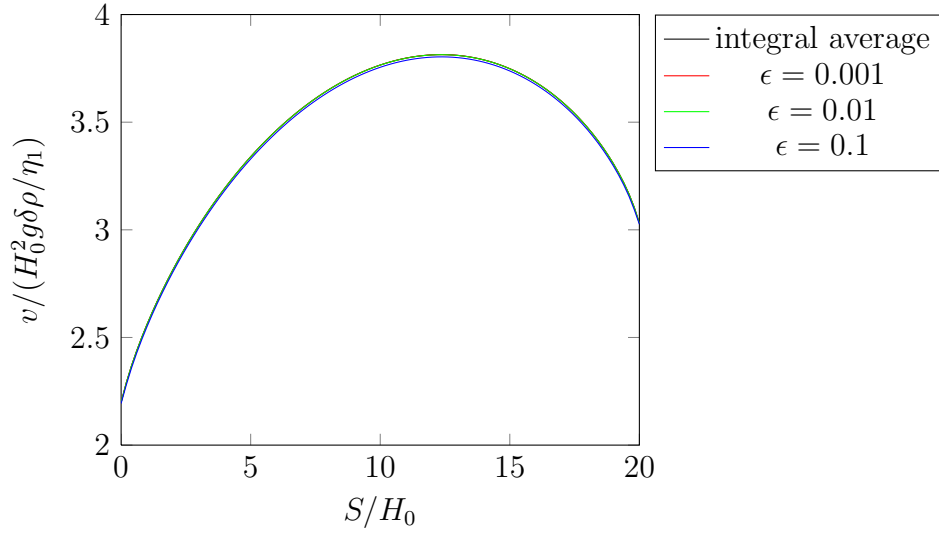
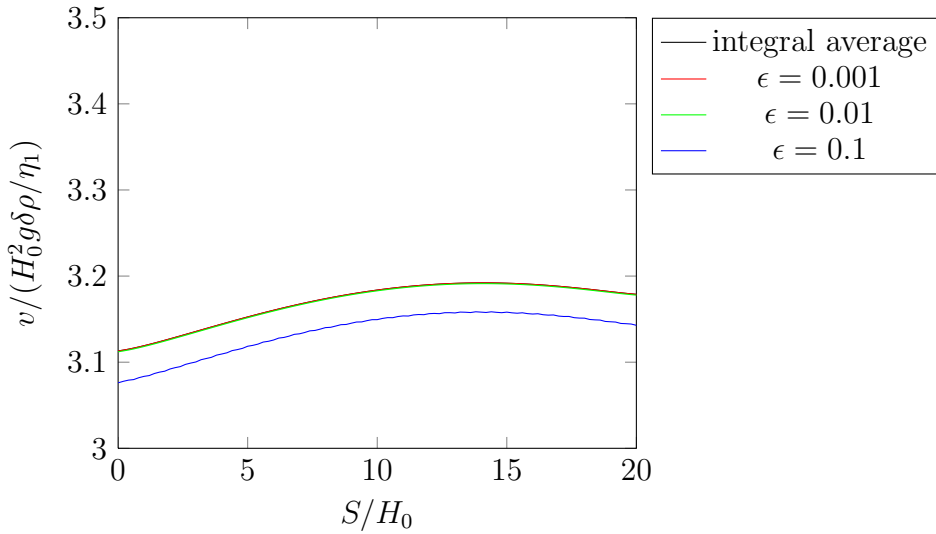
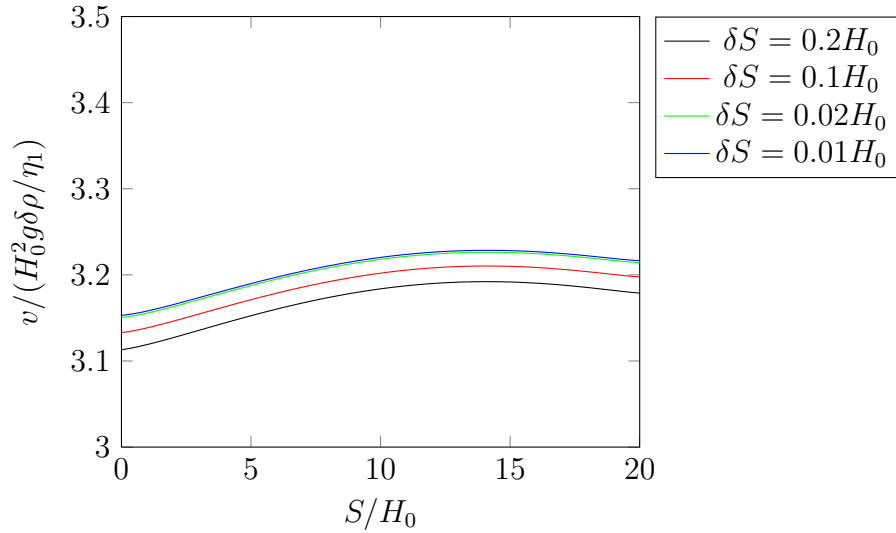
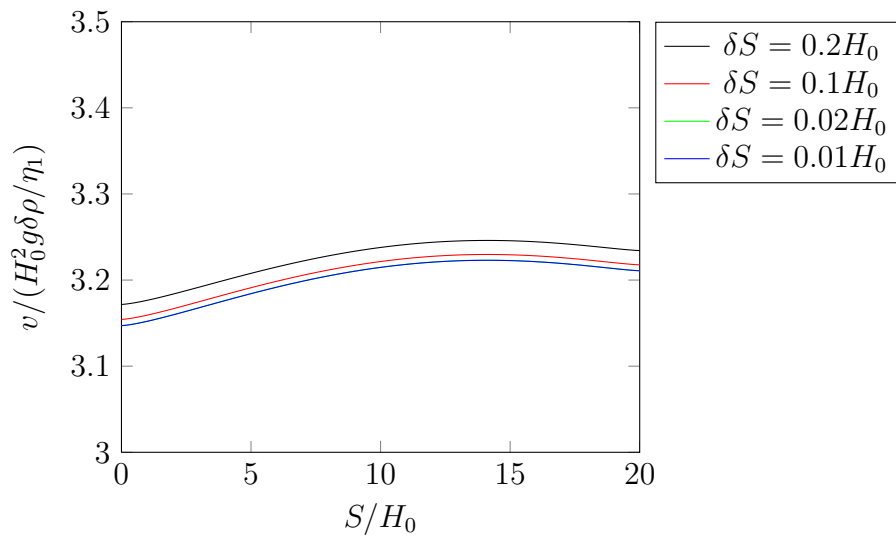
(a) $\gamma = 1$ (b) $\gamma = 100$

Figure 3.5: Vertical velocity $v/(H_0^2 g \delta \rho / \eta_1)$ predicted by BITS for the vertical sheet shown in Fig. 3.3 at $\gamma = 1$ and $\gamma = 100$, using the Gaussian quadrature average method and regularized Stokeslets with different values of ϵ .



(a) integral average method



(b) regularized Stokeslet method

Figure 3.6: Vertical velocities of a vertical sheet with $L = 20H_0$, $d = 10H_0$, $\gamma = 100$ and different discretization numbers. (a) Predictions using the integral average method. (b) predictions using the regularized Stokeslet method.

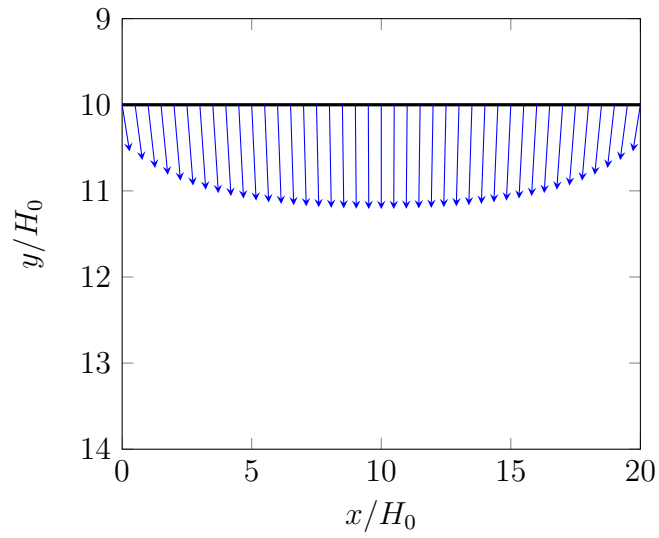
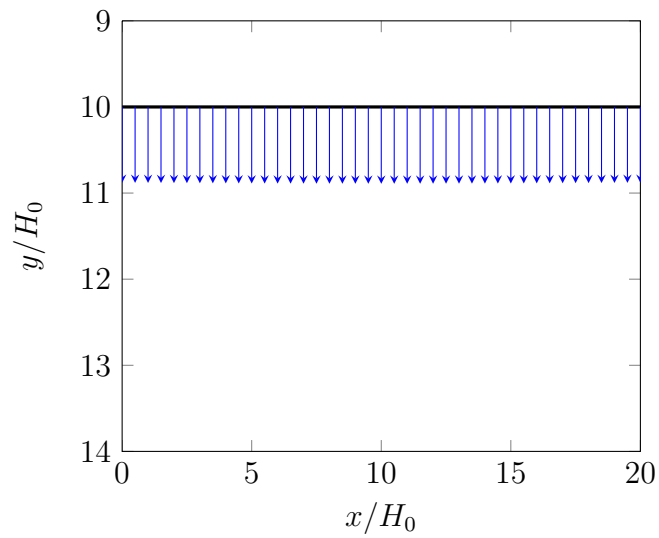
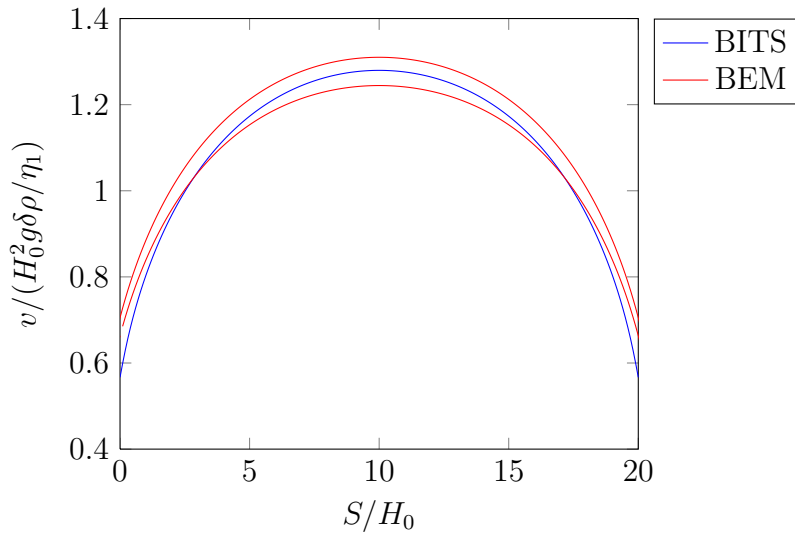
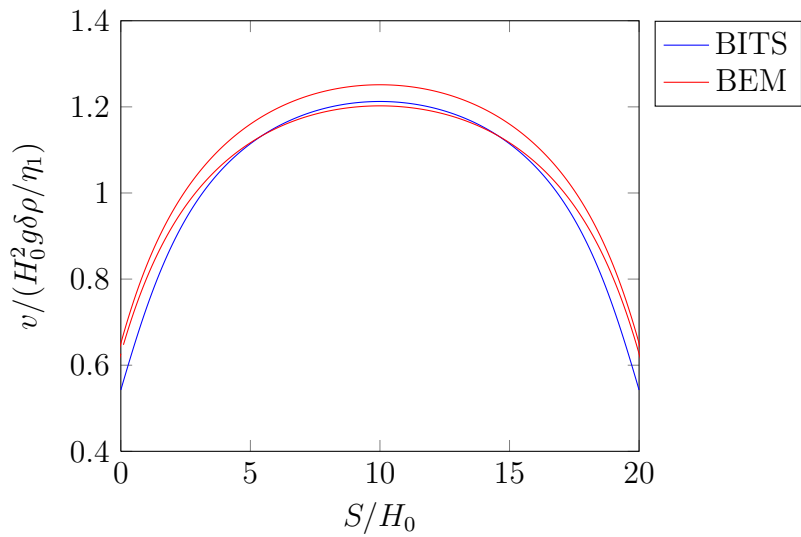
(a) $\gamma = 10$ (b) $\gamma = 10^5$

Figure 3.7: Velocity fields predicted by BITS for a sinking horizontal sheet with two different viscosity ratios γ .

Fig. 3.8 compares the vertical (\mathbf{e}_2 -direction) velocities of the sinking sheet predicted by the BITS (blue) and BEM (red) models, for four different viscosity ratios. Note that the velocities predicted by BITS are on the sheet's midsurface, whereas those predicted by BEM are on both the upper and lower surfaces. The BITS predictions agree well with those of BEM, the errors being comparable to those already seen for the vertical sheet. The errors are largest near the ends of the sheet, which is expected because the BITS model assumptions break down near the ends.

All the calculations above were for a horizontal sheet far away from the free surface ($d = 20H_0$). When the distance is small ($d < H_0$), greater resolution is required for accurate solutions. This is evident in Fig. 3.9 ($L = 20H_0, \gamma = 10000$) and Fig. 3.10 ($L = 40H_0, \gamma = 10000$). From Fig. 3.9(b), it is clear that the results are not reliable when n is small, especially for $n = 100$. But Fig. 3.9 and Fig. 3.10 show that the results converge with increasing resolution and that $\delta S = 0.02H_0$ is generally good enough for the BITS calculations. Moreover, for the horizontal sheet, the regularized Stokeslet is no longer compatible with the discrete method, in which the Green's function on the vertex is considered as the average value around the vertex. The Green's function value at the quasi-singular point changes with different radius ϵ of the regularized Stokeslet, so it is not suitable to be used as the average value nearby which is necessary in the discrete approach. That means the average Green's function varies at singular point with the radius ϵ , and the numerical solution failed to converge as ϵ decreased. Accordingly, the Gaussian quadrature average method will be used in all the following calculations.

(a) $\gamma = 1$ (b) $\gamma = 10$

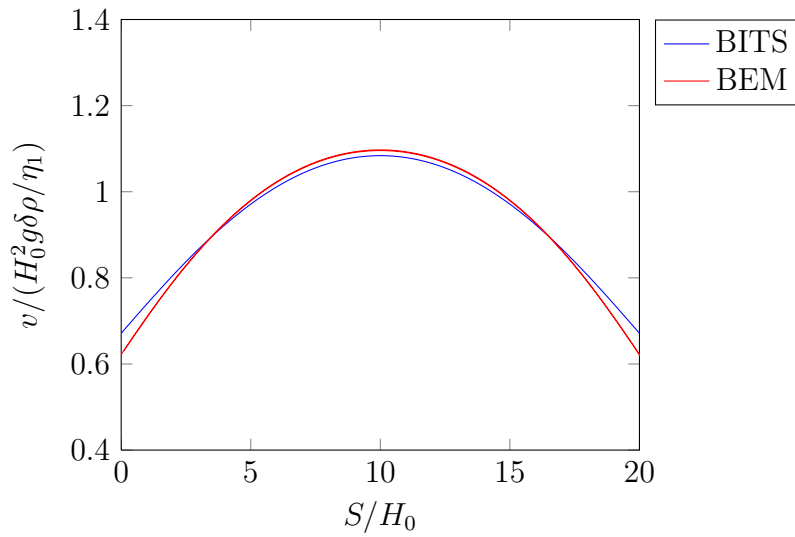
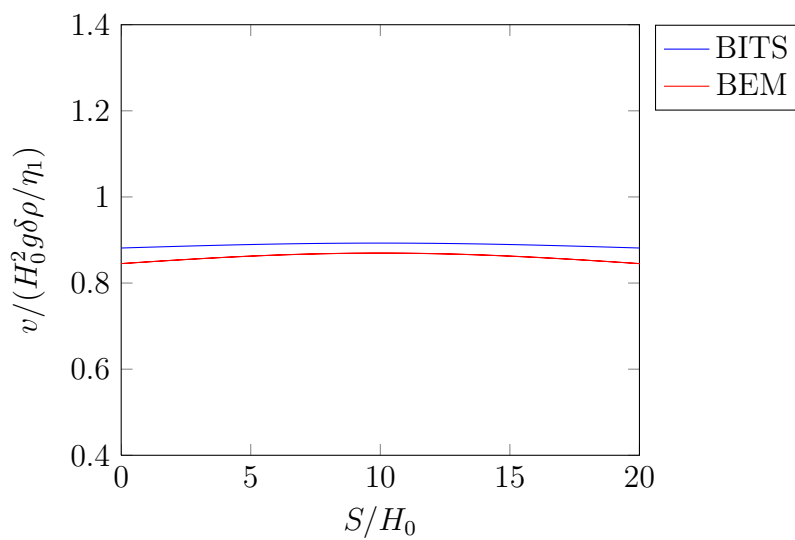
(c) $\gamma = 1000$ (d) $\gamma = 10^5$

Figure 3.8: The sinking velocity predicted by the BITS and BEM models for a horizontal sheet whose geometry is shown in Fig. 3.3. Results are shown for four different viscosity ratios γ .

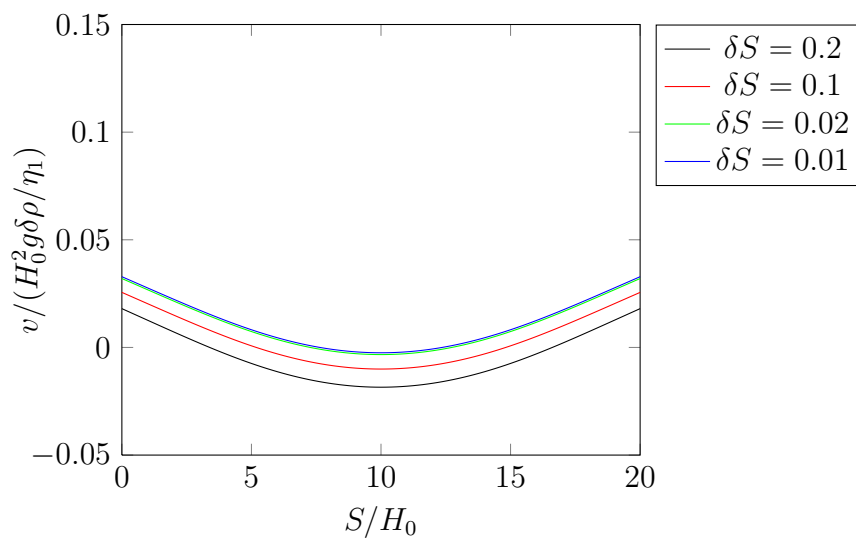
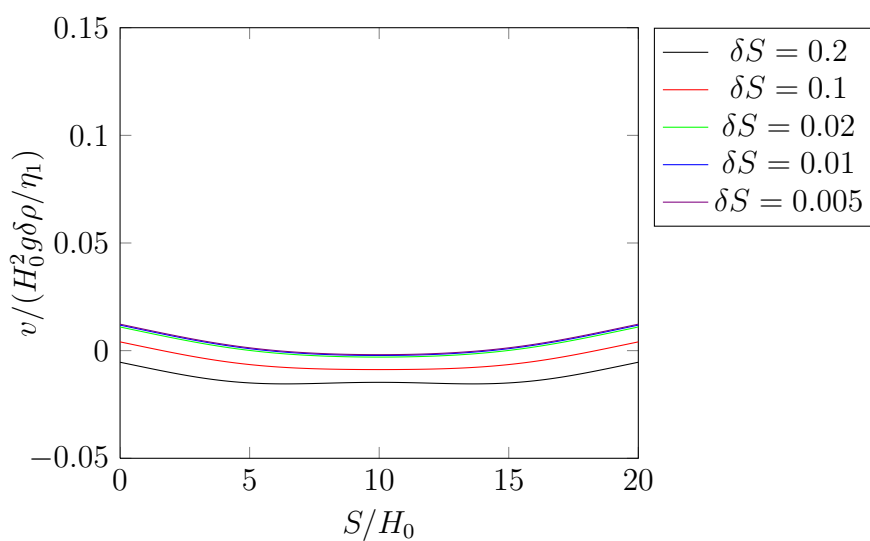
(a) $d = 1H_0$ (b) $d = 0.55H_0$

Figure 3.9: Sinking velocities of a horizontal sheet with $L = 20H_0$ and $\gamma = 10000$ as a function of discretization number, for two values of the lubrication layer thickness d .

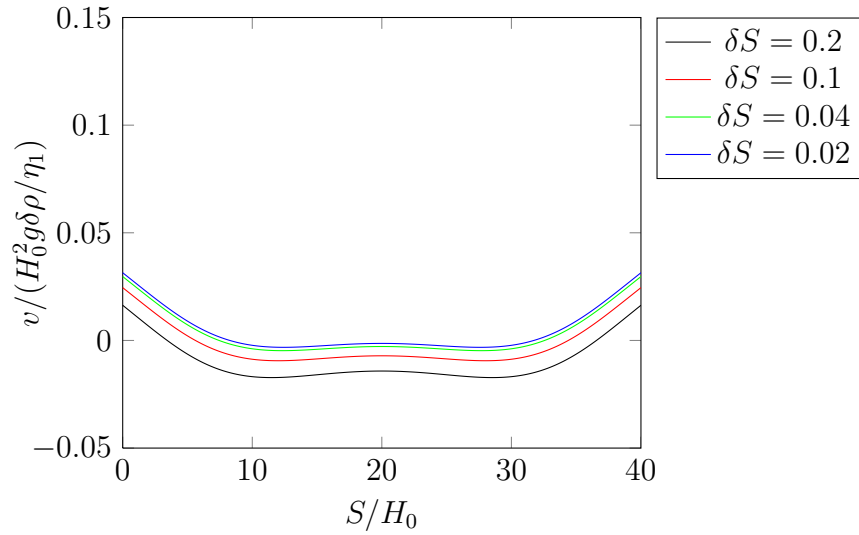
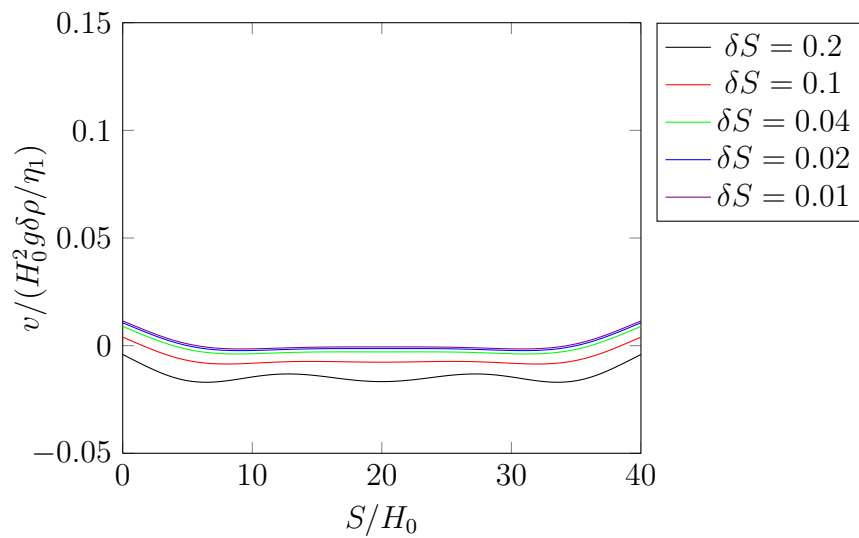
(a) $d = 1H_0$ (b) $d = 0.55H_0$

Figure 3.10: Sinking velocities of a horizontal sheet with $L = 40H_0$ and $\gamma = 10000$ as a function of discretization number, for two values of the lubrication layer thickness d .

3.4.3 Subduction of a bent sheet

Now that the BITS method is validated, we apply it to a simple model of geophysical subduction, in which one end of the sheet is pushed down into the ambient fluid with the slab length l_s and the system is allowed to evolve freely (Fig. 3.1). Fig. 3.11 shows the instantaneous velocity field of a sheet with $L = 40H_0$ and $d = H_0$ for different initial bending angles θ . The two subfigures are calculated with different discretization numbers. It appears that $\delta S = 0.02H_0$ is sufficient for our calculations, so this resolution will be used in all the cases that follow.

The effect of varying the thickness d of the lubrication layer is shown in Fig. 3.12. Comparing this with Fig. 3.11(a), we see that the smaller distance d decreases the sheet's subduction velocity. Moreover, when the distance d is very small, a finer discretization is required to keep the calculation accurate. Fig. 3.13 shows the instantaneous velocity field of a longer ($L = 60H_0$) sheet with all other parameters the same as before. Comparing these velocity fields with those for $L = 40H_0$, we see that the bending moment at the ends is nearly independent of the sheet length. Note that weak bending occurs at the left end of the sheet even though that end has not been pushed down into the ambient fluid.

The intensity of the bending can be quantified by the curling rate \dot{K} . In the discrete approach, the curling rate \dot{K} transforms to the bending rate e_b in Lagrangian description. The curling rate (bending rate) e_i^b on the midsurface is plotted in Fig. 3.14 for a sheet with $L = 40H_0$, $d = 0.5H_0$, and $\gamma = 100$. This figure shows that bending is confined to two boundary layers near the ends of the sheet, separated by a broad central region where no bending occurs. To interpret the above results physically, we need to identify the length scale that characterizes the principal bending region at the right end of the sheet. Referring to Fig. 3.14, we define the bending length l_b as the distance from the end

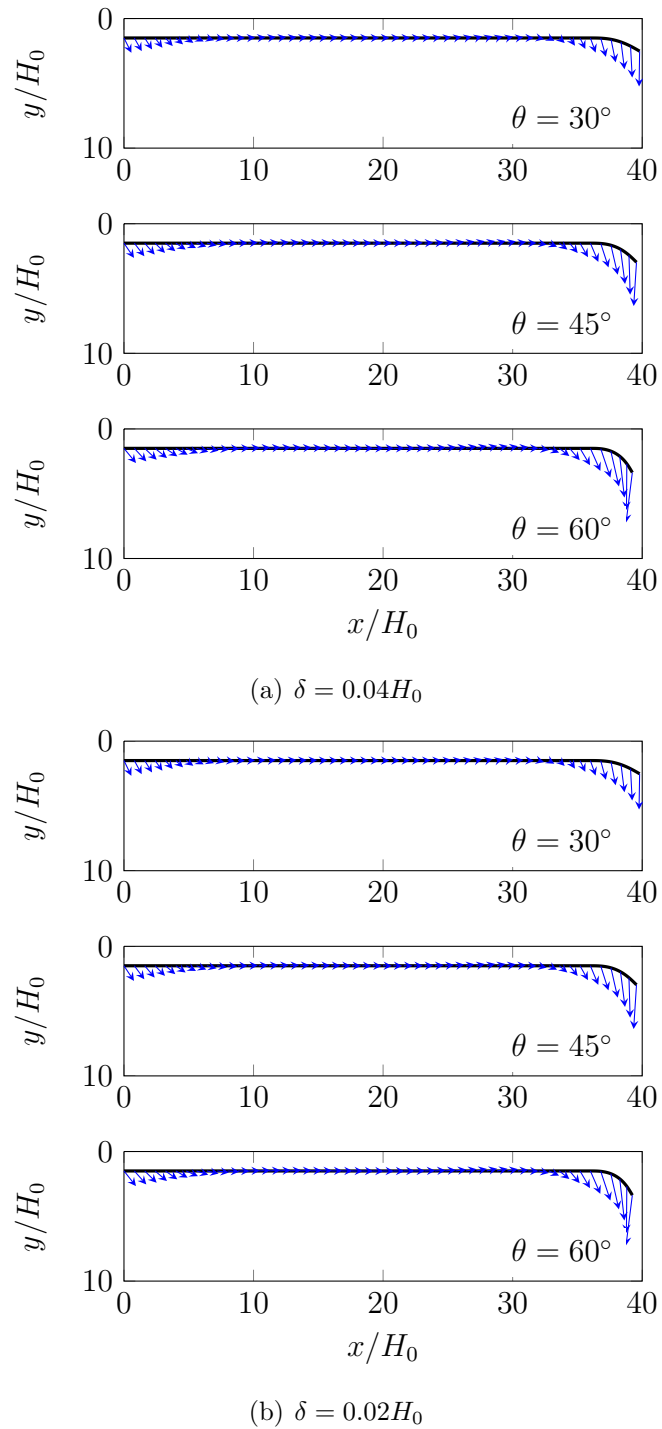


Figure 3.11: Instantaneous velocity field of a sheet with $L = 40H_0$, $\gamma = 1000$ and $d = H_0$, for two different resolutions.

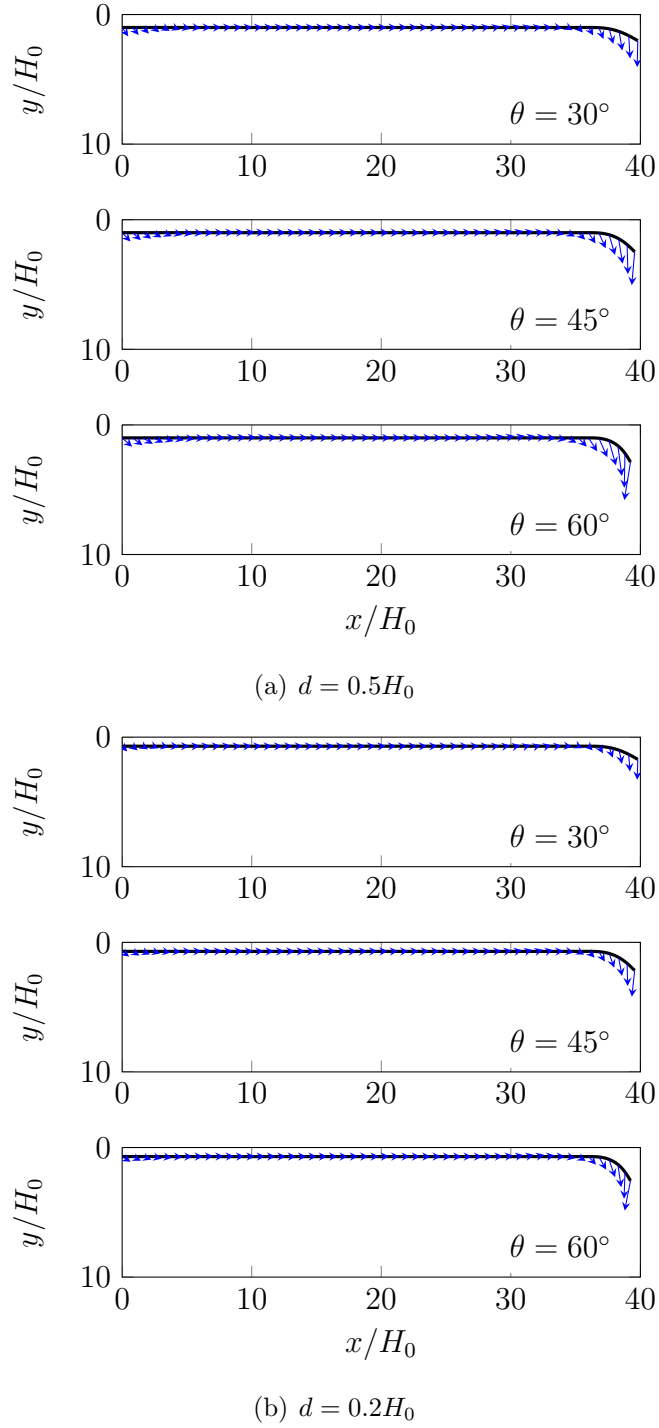


Figure 3.12: Instantaneous velocity field of a sheet with $L = 40H_0$, $\gamma = 1000$, and $\delta S = 0.02H_0$ for two values of the lubrication layer thickness.

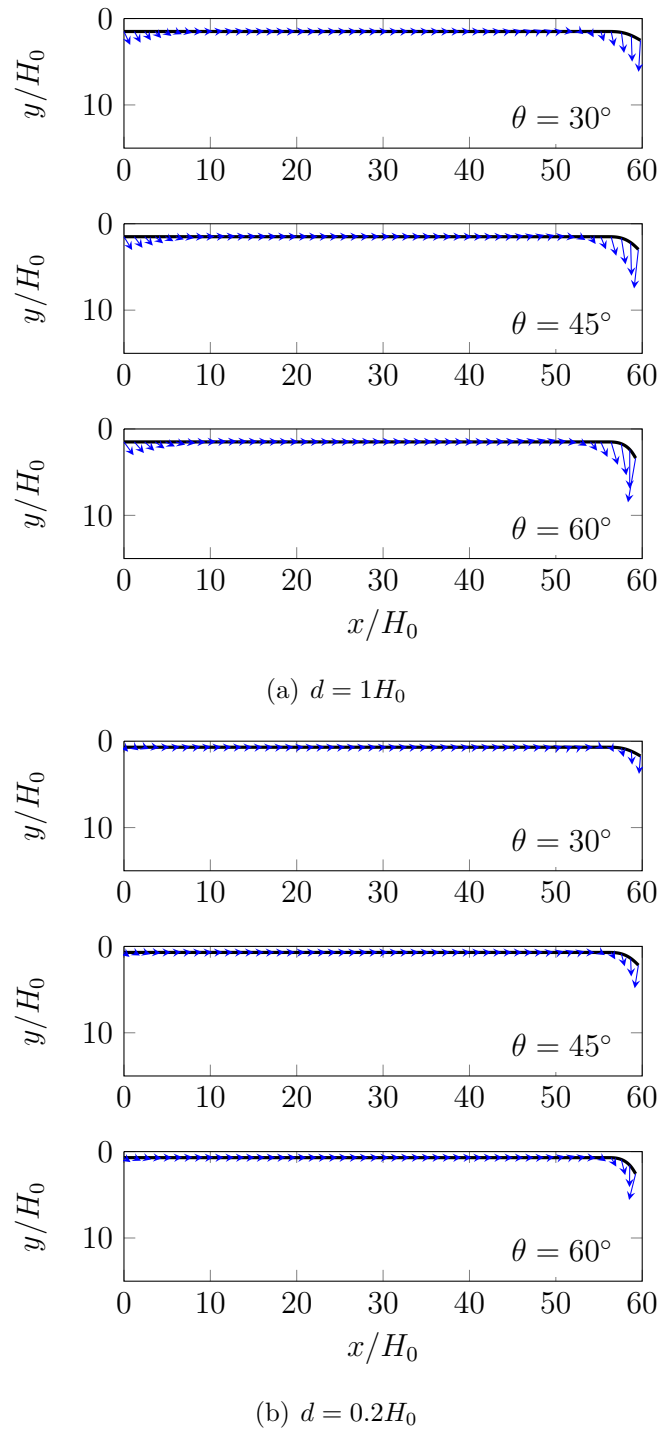


Figure 3.13: Instantaneous velocity field of a sheet with $L = 60H_0$, $\gamma = 1000$, and $\delta S = 0.02H_0$ for two values of the lubrication layer thickness.

of the slab to the point seaward of the trench where the curling rate vanishes. Next, consider the balance of forces acting on the bending portion of the sheet, i.e. the portion of length l_b . Let V be the vertical sinking speed of the leading end of the slab. The traction (normal plus shear) applied to the bending portion by the outer fluid $\sim \eta_1 V/l_b$, which when integrated over the length of the bending portion ($= l_b$) gives a total force $F_{\text{ext}} \sim \eta_1 V$. The internal traction that resists bending $\sim \eta_2 H^3 V/l_b^4$ (Ribe, 2001), which corresponds to a total force $F_{\text{int}} \sim \eta_2 H^3 V/l_b^3$. Finally, because the negative buoyancy of the horizontal part of the sheet is compensated by normal stresses in the lubrication layer, the effective buoyancy force $F_b \sim Hlg\delta\rho$ is due entirely to the slab of length l . In the limit of negligible bending resistance, the balance $F_b \sim F_{\text{ext}}$ implies that V scales as the Stokes sinking speed

$$V \sim \frac{Hlg\delta\rho}{\eta_1} = V_{\text{Stokes}}. \quad (3.30)$$

Moreover, the ratio of the internal and external viscous forces is

$$\frac{F_{\text{int}}}{F_{\text{ext}}} \sim \gamma \left(\frac{H}{l_b} \right)^3 = \text{St}. \quad (3.31)$$

The quantity St is a dimensionless measure of the ‘stiffness’ of a subducting sheet (Ribe, 2010), and determines whether the sinking speed is controlled by the mantle viscosity ($\text{St} \leq 1$) or by the viscosity of the sheet itself ($\text{St} \gg 1$). Fig. 3.15 shows a plot of the dimensionless sinking speed V/V_{Stokes} versus St for the results obtained with $L = 60H_0$, $d = 0.2H_0$ and different values of γ and l_s/H_0 . For each value of θ_0 , the numerical predictions of V collapse onto a single master curve with two limits: a ‘Stokes’ limit $\text{St} < 0.1$, and a ‘flexural’ limit $\text{St} > 3$. In the Stokes limit, the sinking speed is controlled entirely by the viscosity η_1 of the outer fluid, whereas it is controlled by the inner viscosity η_2 in the flexural limit.

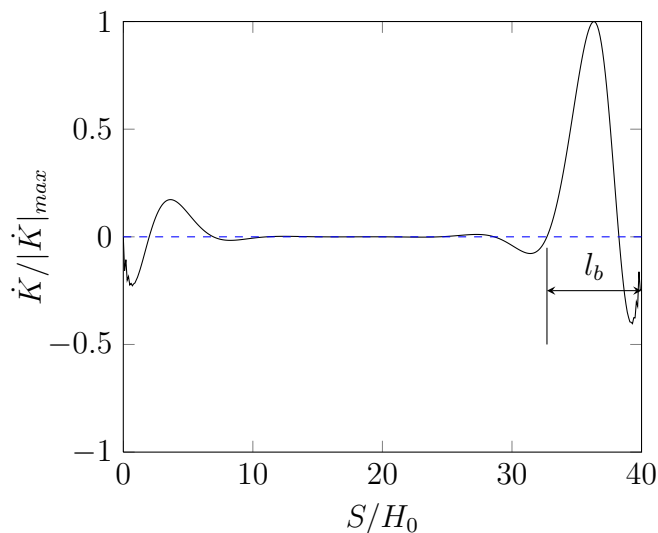


Figure 3.14: The curling rate of a bent sheet with $L = 40H_0$, $\gamma = 100$ and $d = 0.5H_0$

The solutions discussed above were all instantaneous solutions valid at a moment when the sheet had a given geometry. We now turn to time-dependent simulations. The evolution of the sheet's shape is governed by the two differential equations. For given right-hand sides of the above equations, the velocity is advanced in time using a simple Euler scheme, viz.,

$$\mathbf{X}_{new} = \mathbf{X} + \mathbf{U} \cdot dt, \quad (3.32)$$

and the thickness of the sheet is calculated in the discrete approach (see (2.61)). Repeating this procedure, we obtain the time evolution of the sheet's shape. Fig. 3.16 shows subduction of a sheet with $L = 40H_0$ and $\gamma = 1000$ from $t = 0$ to $t = 35\tau_0$, where $\tau_0 = \eta_1/g\delta\rho H_0$ is the time scale used to nondimensionalize the equations. And Fig. 3.15 shows subduction of a sheet with $L = 40H_0$ and $\gamma = 100$ from $t = 0$ to $t = 35\tau_0$. The weak subduction of the trailing edge of the sheet has

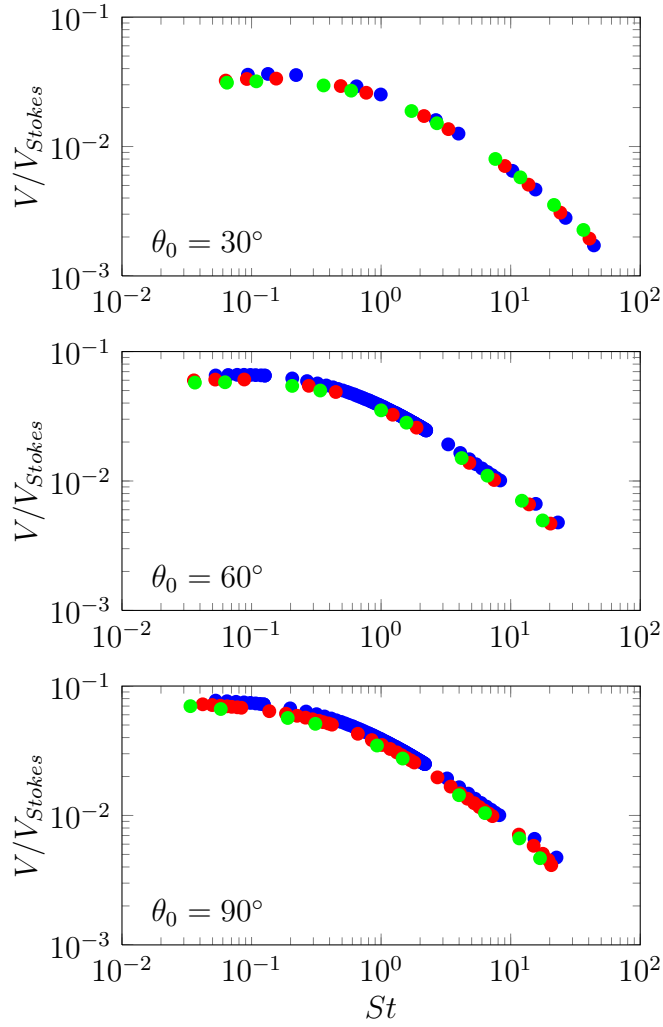
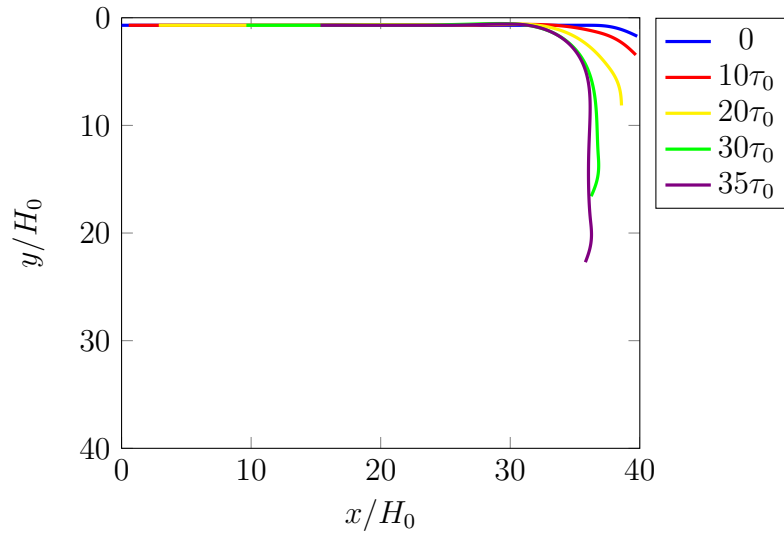
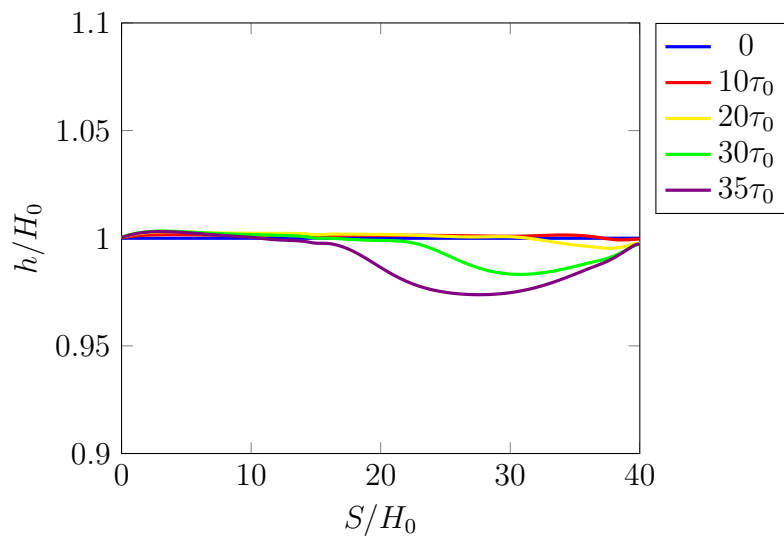


Figure 3.15: Dimensionless sinking speed V/V_{Stokes} of the slab as a function of the sheet stiffness St , for three different values of the dip θ_0 . Solutions with $L = 60H_0$ and $d = 0.2H_0$ are shown for different values of γ and l_s/H_0 . Blue: $l_s/H_0 = 4$, red: $l_s/H_0 = 6$, green: $l_s/H_0 = 8$.

been suppressed by straightening out the end of the sheet after each time step, using the algorithm of Li and Ribe (2012), appendix B.

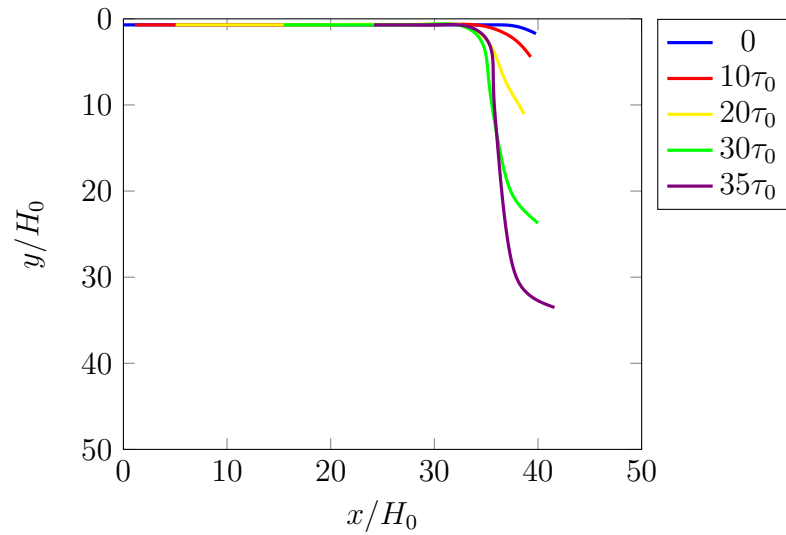


(a) Sheet shape

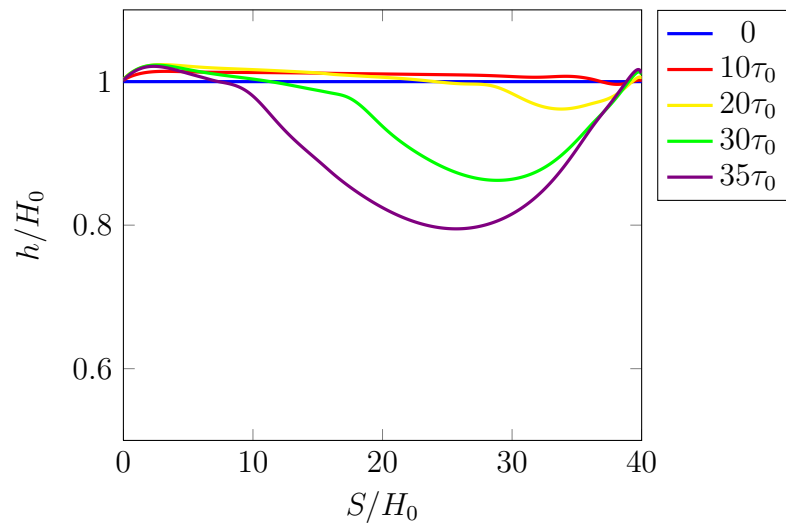


(b) Sheet thickness

Figure 3.16: Shape (a) and thickness (b) of a sheet with $L = 40H_0$, $d = 0.2H_0$, $\theta_0 = 30^\circ$ and $\gamma = 1000$ at different times from 0 to $35\tau_0$.



(a) Sheet shape



(b) Sheet thickness

Figure 3.17: Shape (a) and thickness (b) of a sheet with $L = 40H_0$, $d = 0.2H_0$, $\theta_0 = 30^\circ$ and $\gamma = 100$ at different times from 0 to $35\tau_0$.

Chapter 4

Parallel code for three dimensional multiphase flow

In this chapter, we briefly present the new parallel solver BLUE for fully three-dimensional multiphase flows developed by Shin, Chergui, and Juric (2014). The solver runs on a variety of computer architectures from laptops to supercomputers and on 131072 threads or more (limited only by the availability of threads). The code is wholly written by the authors in Fortran 2003 and uses a domain decomposition strategy for parallelization with MPI.

4.1 Mathematical formulation

Here, we will describe the basic solution procedure for the Navier-Stokes equations with a brief explanation of the interface method. The governing equations for transport of an incompressible two-phase flow can be

expressed by a single field formulation as follows:

$$\nabla \cdot \mathbf{u} = 0, \quad (4.1)$$

$$\rho \left(\frac{\partial \mathbf{u}}{\partial t} + \mathbf{u} \cdot \nabla \mathbf{u} \right) = -\nabla P + \rho \mathbf{g} + \nabla \cdot \mu (\nabla \mathbf{u} + \nabla \mathbf{u}^T) + \mathbf{F}. \quad (4.2)$$

where \mathbf{u} is the velocity, P is the pressure, \mathbf{g} is the gravitational acceleration, and \mathbf{F} is the local surface tension force at the interface. \mathbf{F} can be described by the hybrid formulation

$$\mathbf{F} = \sigma \kappa_H \nabla I, \quad (4.3)$$

where σ is the surface tension coefficient, I is the indicator function which is zero in one phase and unity in the other phase. Numerically I is resolved with a sharp but smooth transition across 3 to 4 grid cells. κ_H is twice the mean interface curvature field calculated on the Eulerian grid using:

$$\kappa_H = \frac{\mathbf{F}_L \cdot \mathbf{G}}{\sigma \mathbf{G} \cdot \mathbf{G}}, \quad (4.4)$$

where

$$\mathbf{F}_L = \int_{\Gamma(t)} \sigma \kappa_f \mathbf{n}_f \delta_f(\mathbf{x} - \mathbf{x}_f) ds, \quad (4.5)$$

$$\mathbf{G} = \int_{\Gamma(t)} \mathbf{n}_f \delta_f(\mathbf{x} - \mathbf{x}_f) ds. \quad (4.6)$$

Here \mathbf{x}_f is a parametrization of the interface $\Gamma(t)$, and $\delta_f(t)$ is a Dirac distribution that is non-zero only when $\mathbf{x} = \mathbf{x}_f$. \mathbf{n}_f is the unit normal vector to the interface and ds is the length of the interface element. κ_f is again twice the mean interface curvature, but obtained from the Lagrangian interface structure. The geometric information, unit normal \mathbf{n}_f and length of the interface element ds in \mathbf{G} , \mathbf{F} are computed directly from the Lagrangian interface and then distributed onto an Eulerian grid using the discrete delta function.

The indicator function I is essentially a numerical Heaviside function and is generated using a vector distance function computed directly from the tracked interface. I is found by solving the Poisson equation

$$\nabla^2 I = \nabla \cdot \int_{\Gamma(t)} \mathbf{n}_f \delta(\mathbf{x} - \mathbf{x}_f) ds. \quad (4.7)$$

The details following Peskin's (Peskin, 1977) well known immersed boundary approach and a description of our procedure for calculating the force \mathbf{F} and constructing the function field \mathbf{G} and indicator function I can be found in Shin and Juric (2002); Shin et al. (2005); Shin and Juric (2007); Shin (2007); Shin and Juric (2009a,b); Shin et al. (2011).

The Lagrangian elements of the interface are advected by integrating

$$\frac{d\mathbf{x}_f}{dt} = \mathbf{V} \quad (4.8)$$

with a second order Runge-Kutta method where the interface velocity \mathbf{V} is interpolated from the Eulerian velocity. Material properties such as density or viscosity are defined in the entire domain with the indicator function as $I(\mathbf{x}, t)$. For example:

$$b(\mathbf{x}, t) = \mathbf{b}_1 + (\mathbf{b}_2 - \mathbf{b}_1)I(\mathbf{x}, t), \quad (4.9)$$

where the subscripts 1 and 2 stand for the respective phases.

4.2 Numerical method

This section is organized as follows. At first, we describe the level contour interface reconstruction method (LCRM) dealing with the interface in multiphase flows in 4.2.1. Then, we show how to realise the level contour interface reconstruction method (LCRM) for parallel processing in 4.2.2. Finally in 4.2.3, we briefly describe the the complete solution procedure in this parallel code for three dimensional multiphase flows.

4.2.1 Interface treatment

Due to the complex dynamics of interface motion, it is extremely difficult to formulate an accurate and general numerical scheme for multiphase flow simulations, especially in three-dimensions. Among the variety of numerical techniques and grid structures for handling flows in the presence of interfaces are those which use a stationary underlying Eulerian/Cartesian grid for the primary velocity-pressure variables with an additional technique for interface treatment. The latter can be either on the same Eulerian grid (thus capturing the interface) or based on a supplemental overlying moving grid (which tracks the interface), and both have become popular due to their relative simplicity and efficiency. Variants and hybrids of these basic Front Tracking or Front Capturing methods are widely used in multiphase applications. The basic idea in Front Tracking is that one tracks the motion of the interface explicitly using a separate discretized representation of the interface which moves with it. In Front Capturing one uses an additional field variable such as a volume function (VOF) or distance function (Level Set) to follow the interface motion implicitly.

Nowadays, hybrid methods which retain only the desirable characteristics of both Front Tracking and Front Capturing approaches have become popular (Sussman and Puckett, 2000; Coyajee and Boersma, 2009; Enright et al., 2002; Aulisa et al., 2003). We shall use one such hybrid method, the Level Contour Reconstruction Method (LCRM). The LCRM retains the usual features of classic Front Tracking: to represent the interface with a triangular surface element mesh, to calculate the surface tension and advect it. A major advantage of the LCRM, compared with standard Front Tracking, is that all the interfacial elements are implicitly instead of logically connected. The LCRM periodically reconstructs the interface elements using a computed distance function

field, a field such as the one used by the Level Set method, thus allowing an automatic treatment of interface element restructuring and topology changes without the need for logical connectivity between interface elements as was necessary in the original Front Tracking method. It is important to note that this distance function field plays no role whatsoever in the actual advection of the interface as it centrally does in the original Level Set method. We never need to solve an advection equation for the distance function. The LCRM thereby avoids the need for special corrective procedures to conserve mass such as Level Set reinitialization. An additional important benefit of the LCRM approach is that all operations are local to an individual triangular element independent of other elements. This principle of locality renders the LCRM particularly attractive for parallel computing since it carries over to distributed processing on local subdomains and thus its implementation on distributed processors is rather straightforward.

Here we briefly describe the basic concept behind the LCRM and recent major improvements which include the use of high order interpolation, a vector valued distance function and tetra-marching in the interface reconstruction procedure. A more detailed description of these new features can be found in S. Shin and D. Juric (Shin and Juric, 2002; Shin et al., 2005; Shin and Juric, 2007; Shin, 2007; Shin and Juric, 2009a,b; Shin et al., 2011). The LCRM reconstructs the Lagrangian triangular interface elements by drawing constant contour surfaces of a distance function field as in Fig. 4.1 (shown for two-dimensions). Lines of constant contour can be drawn on the level contour field of the scalar distance function ϕ , at each reconstruction cell. These lines in each reconstruction cell share common end points and thus form implicitly connected surface elements across neighboring Eulerian grid cells. In the three dimensional case, a rectangular grid cell (Fig. 4.2(a)) will be divided into five tetrahedral reconstruction cells as in Fig. 4.2(b). For

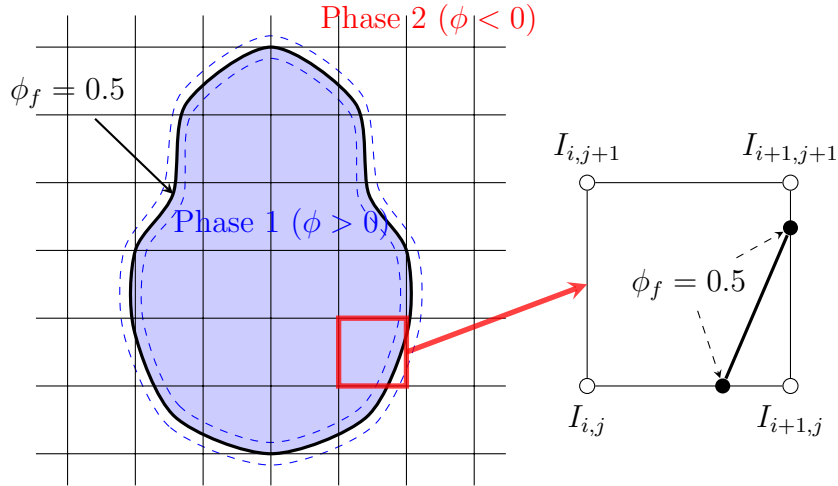


Figure 4.1: Level contour reconstruction in a 2D calculation. Interfaces are reconstructed by linear approximation of the $\phi_f = 0.5$ contour in each grid cell. The two endpoints of this contour line form the endpoints of one new interface element. Adjacent elements are physically linked but not logically connected.

each tetrahedral reconstruction cell, the interface reconstruction will be performed on cell faces similar to the 2D procedure above. After locating contour lines on the four faces of a tetrahedral reconstruction cell, the edges of contour faces can be obtained. Using the reconstructed edge lines, we can generate triangular elements as in Fig. 4.2(c). Since identical reconstructed edge lines are shared by neighboring reconstruction cells, all interface elements are implicitly connected without any logical connectivity. In order to ensure continuous reconstructed faces for the entire simulation domain, a tetra-marching orientation for the reconstructing tetrahedral cells is used as in Fig. 4.2(d).

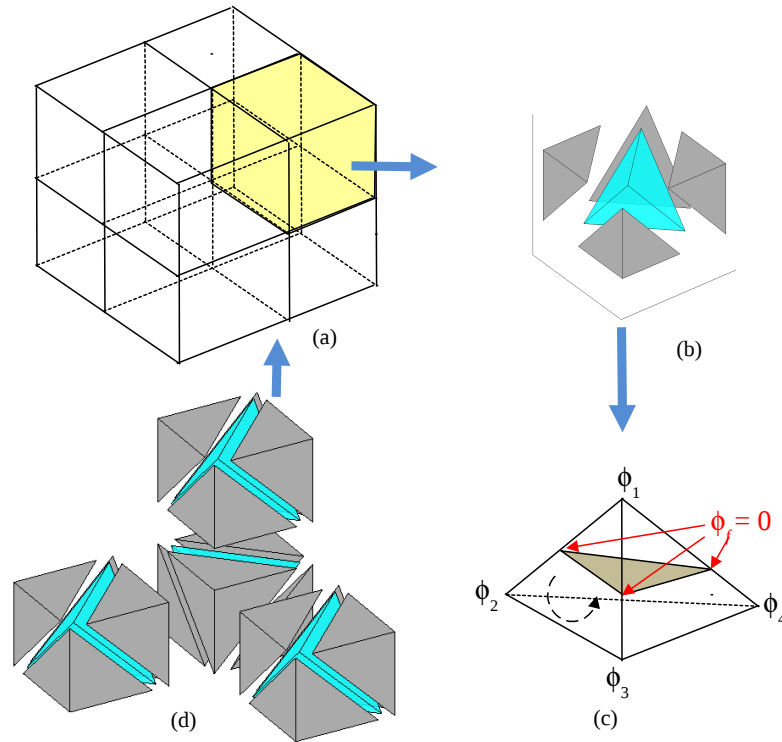


Figure 4.2: Procedure for LCRM in three-dimensions: (a) Eulerian grid structure (b) grid subdivision for tetrahedral reconstruction cell (c) interface element reconstruction in a tetrahedral cell (d) tetra-marching procedure for continuous interface interconnection.

4.2.2 Extended interface for parallel processing

In order to take advantage of the increased speed of modern high performance computing resources, numerical methods for multiphase flows, the treatment of interfaces and Navier-Stokes solvers must be adapted to multi-thread distributed processing and memory architecture.

Domain decomposition whereby the physical simulation domain (Fig. 4.3(a)) is subdivided into subdomains (Fig. 4.3(b)) each associated with

a dedicated processing thread is relatively straightforward to implement for Eulerian/Cartesian meshes. Field variable data exchange takes place across neighboring subdomains via a boundary buffer zone. But with the existence of a moving Lagrangian interface grid as in the LCRM we need to apply an extended interface concept which uses additional buffer cells to store and exchange interface data necessary to the LCRM. As illustrated in Fig. 4.4, a subdomain is defined with two types of buffer zone: (1) a buffer zone for exchange of boundary data as before and (2) a new buffer zone for an extended interface which contains interface elements that extend beyond the physical subdomain boundary. There is an important difference in the way that some of the data is handled in these two buffer zones. In the boundary buffer zone, data is exchanged to adjacent subdomains in order to provide necessary boundary information overlap for the field variable solutions.

In the extended interface buffer zone, each subdomain independently uses the Lagrangian interface information that is stored locally in its subdomain/buffer to perform interface operations and periodically apply the interface reconstruction procedure. The key advantage of the extended interface buffer is that interface operations are kept local to a subdomain and its buffer. Thus each subdomain/buffer handles tracking and operations on the Lagrangian interface elements (such as surface tension calculation) independently of the other subdomains. Since it is the boundary condition buffer that provides necessary field data such as the velocity field necessary for the Lagrangian element advection in the extended interface buffer and likewise for adjacent subdomain/buffers, the interface elements in the overlapping interface buffer zones will follow the same path independently. (This feature, which eases the task of parallelization greatly, can be viewed as having been inherited from the original LCRM philosophy of keeping operations local to an interface element or in this case local to a subdomain.) Finally since the inter-

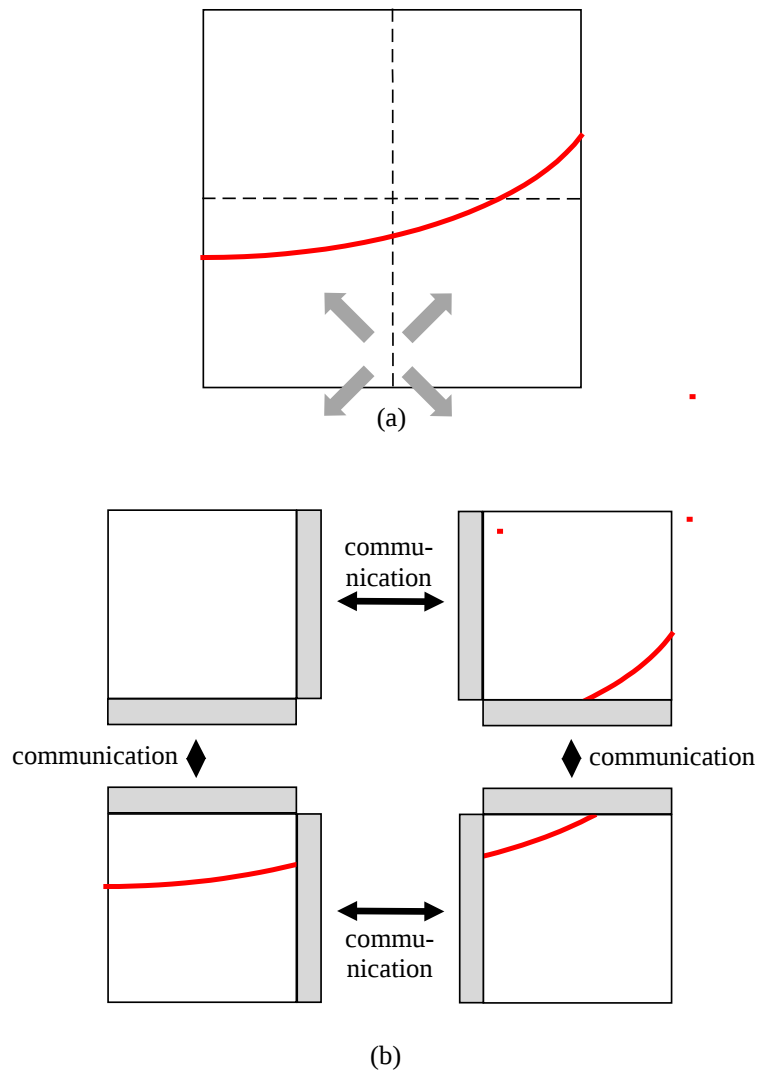


Figure 4.3: Domain decomposition concept for distributed processing.

face must be reconstructed periodically, distance function values are also communicated in the extended interface buffer to adjacent subdomains in order to ensure interface connectivity across subdomains.

4.2.3 Solution procedure in parallel computing

The code structure consists essentially of two main modules: (1) a module for solution of the incompressible Navier-Stokes equations and (2) a module for the interface solution including tracking the phase front, initialization and reconstruction of the interface when necessary. The parallelization of the code is based on an algebraic domain decomposition technique. The code is written in Fortran 2003 and communications are managed by data exchange across adjacent subdomains via the Message Passing Interface (MPI) protocol. The Navier-Stokes solver computes the primary variables of velocity \mathbf{u} and pressure P on a fixed and uniform Eulerian mesh by means of Chorin's projection method (Chorin, 1968). Depending on the physical problem, numerical stability requirements and user preferences, the user has a choice of explicit or implicit time integration to either first or second-order. For the spatial discretization we use the well-known staggered mesh, MAC method (Harlow et al., 1965). The pressure and the distance function are located at cell centers while the components of velocity are located at cell faces. All spatial derivatives are approximated by standard second-order centered differences.

Another important issue in parallel computing for incompressible flow, in addition to the interface treatment, is solving the elliptic Poisson equation for the pressure. The projection method leads to a Poisson problem for the pressure which, for two-phase discontinuous density flows, is non-separable:

$$\nabla \cdot \left(\frac{\nabla P}{\rho} \right) = S, \quad (4.10)$$

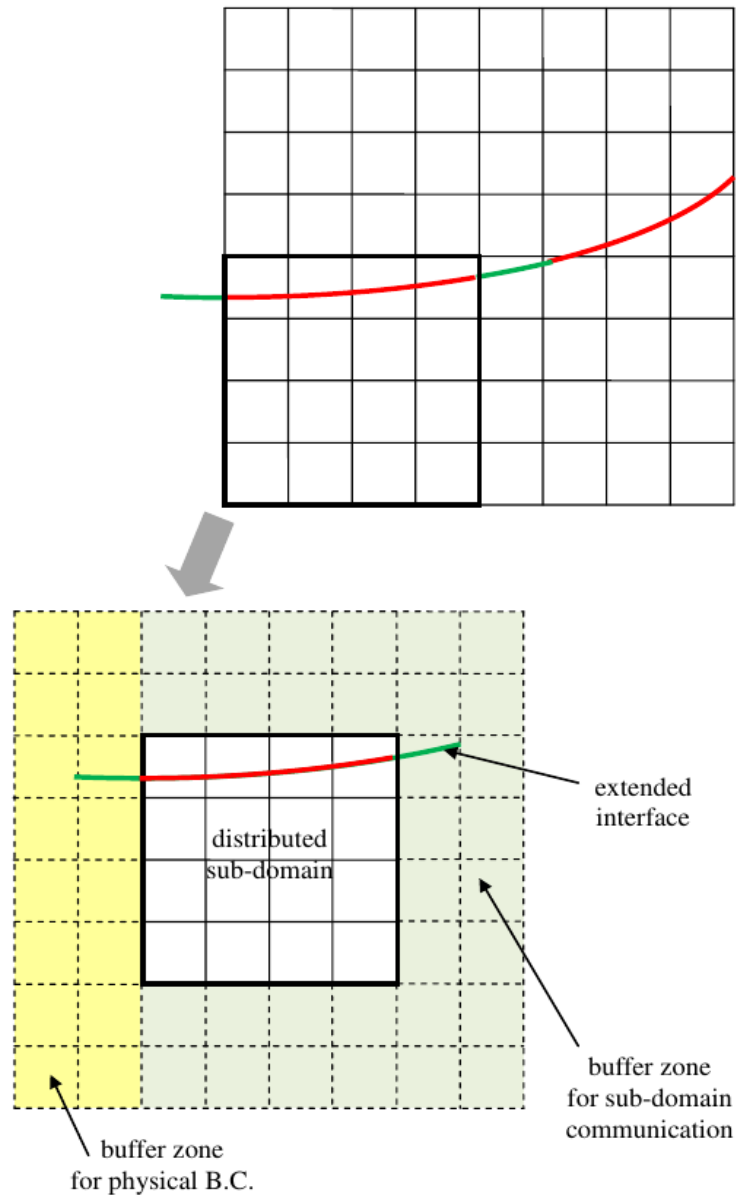


Figure 4.4: Extended interface concept using buffer zone for distributed processing with the LCRM.

where the density field ρ is discontinuous since $\rho = \rho_1$ in phase 1 and $\rho = \rho_2$ in phase 2. The source term S is a function of the non-projected velocities and interfacial tension.

For single phase flow, the Poisson problem is separable and the conventional multigrid approach (Briggs et al., 2000), especially for distributed computing, has become quite attractive due to its near ideal efficiency compared with other iterative gradient based methods. However, in two-phase flows with large density differences between fluids, the conventional multigrid technique becomes less efficient and often fails to converge. Thus one of the most challenging issues, besides modeling the dynamics of the interface between the two fluid phases, is the efficient solution of the pressure equation for high density ratio.

In the BLUE code a modified parallel 3D V-cycle multigrid solver based on the work of Kwak and Lee (Kwak and Lee, 2003) has been developed. The solver incorporates a parallel multigrid procedure whose restriction and prolongation operators are not associated with each other, contrary to common usage. This method has been successfully implemented to solve 3D elliptic equations where coefficients can be highly discontinuous. The procedure can handle large density discontinuities up to density ratios of $O(10^5)$. The key features of the modified multigrid implementation can be summarized as follows:

- 1) Cell-centered second-order finite difference approximation of equation 4.10.
- 2) Harmonic approximation of the discontinuous coefficient $1/\rho$.
- 3) Linear interpolation of the residual during the restriction process.
- 4) Cell flux conservation of the error on coarse grids during the prolongation process.
- 5) Parallel Red-Black SOR technique to relax the linear systems on fine grids.
- 6) Solution of the error using a parallel GMRES algorithm on the

coarsest grid.

In the following chapter we will investigate viscous folding in diverging microchannels with the parallel solver BLUE for fully three-dimensional two-phase flows.

Chapter 5

Simulation of viscous folding in diverging microchannels

In this chapter we use the parallel multi-phase flow code BLUE to perform a numerical study of viscous folding in diverging microchannels. Due to the high viscosity contrast and very low Reynolds numbers involved, direct numerical simulations are very challenging and to our knowledge these are the first three-dimensional direct parallel numerical simulations of viscous threads in micro channels.

Viscous folding is observed in daily life, for example, when we pour honey, molten chocolate, or shampoo onto a flat surface. It has been extensively studied since the pioneering work of Taylor (1969), who recognized that a longitudinal compressive stress is a necessary condition for the folding instability. In recent years, the folding of viscous threads in diverging microchannels has been systematically investigated by Cubaud and Mason (2006a). Their purpose was to devise a strategy to enhance mixing by using viscous folding to increase the specific surface area of an interface between two fluids. Motivated by their work, we perform numerical simulations of microfluidic viscous folding as a function of the

flow rate ratio and the viscosity ratio between the two fluids, as well as the divergence angle of the channel.

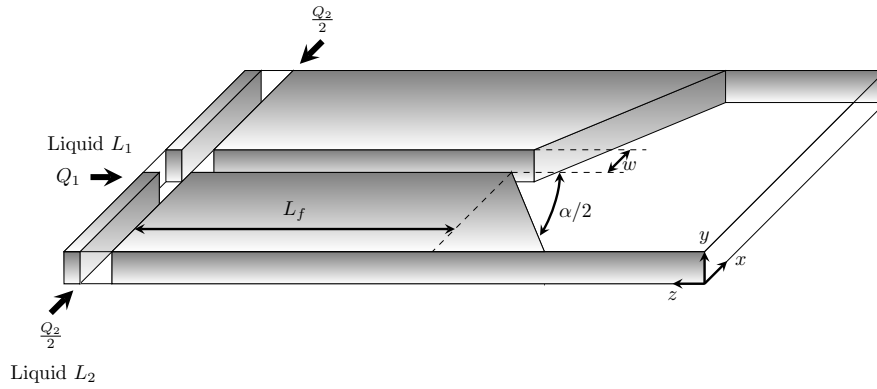


Figure 5.1: The calculation domain of the microchannel. The width of the inlets and the microchannel is $w = 0.25$ mm and the length of the focusing microchannel is L_f .

Fig. 5.1 shows the computational domain, which is similar to that used by Cubaud and Mason (Cubaud and Mason, 2006a). The geometry is composed of two subdomains: the flow-focusing part and the flow-diverging part. The more viscous liquid L_1 with viscosity η_1 is injected into the channel from the center inlet at a volumetric rate Q_1 , and the less viscous liquid L_2 with viscosity η_2 from two side inlets at a total volumetric rate Q_2 . The dimensions of the simulation domain are $2 \text{ mm} \times 0.25 \text{ mm} \times 5 \text{ mm}$. The width of the inlets and the microchannel is $w = 0.25$ mm. We use an open boundary condition on the outlet.

Some important dimensionless numbers are defined as follows:

$$\chi = \frac{\eta_1}{\eta_2}, \quad (5.1)$$

$$\phi = \frac{Q_1}{Q_2}, \quad (5.2)$$

$$\text{Re}_1 = \frac{\rho_1 L V_1}{\eta_1}, \quad (5.3)$$

$$\text{Re}_2 = \frac{\rho_2 L V_2}{\eta_2}, \quad (5.4)$$

$$\text{Ca}_1 = \frac{\gamma \bar{V}}{\eta_1}, \quad (5.5)$$

$$\text{Ca}_2 = \frac{\gamma \bar{V}}{\eta_2}. \quad (5.6)$$

The characteristic length scale $L = 0.5w$, and the characteristic velocities in Reynolds numbers V_1 and V_2 are the average velocities and can be calculated from the volume flow flux and geometry parameters $V_1 = Q_1/w^2$ and $V_2 = 0.5Q_2/w^2$. The capillary numbers are calculated in the long focusing channel, the characteristic velocity is $\bar{V} = (Q_1 + Q_2)/w^2$. Furthermore, we designed different channel geometries with two different diverging angles $\alpha = \pi$ and $\alpha = \pi/2$ for the main chamber.

A reference simulation (case 1) is chosen and its detailed parameters and dimensionless numbers are shown in the Table 5.1.

In our parameter study, five simulations are performed. The dimensionless quantities for these cases are given in Table 5.2. In all 5 simulations the capillary number Ca_1 is kept constant at 330.64, the surface tension force is small compared to the viscous force for the liquid L_1 . All the simulations are implemented using 64 ($4 \times 2 \times 8$) computational cores (subdomains) in parallel, and for each subdomain we use a $64 \times 32 \times 64$ mesh resolution. Thus the global mesh resolution for the domain is $256 \times 64 \times 512$.

Variables	Units	Values
ρ	kg/mm ³	0.8×10^{-6}
η_1	kg/mm/s	4864.28×10^{-6}
η_2	kg/mm/s	2.24×10^{-6}
Q_1	mm ³ /s	0.83333
Q_2	mm ³ /s	10
γ	kg/s ²	2.55×10^{-3}
Re ₁		2.74×10^{-4}
Re ₂		3.57
Ca ₁		330.64
Ca ₂		0.15
ϕ		1/12
χ		2174
α		$\pi/2$

Table 5.1: Dimensional and nondimensional parameters for the simulation case 1 with $\chi = 2174$, $\phi = 1/12$ and $\alpha = \pi/2$.

As a first qualitative demonstration of our model and the parallel code BLUE, a simulation at one half of this resolution is carried out. The velocity field for the case 2 is presented in Fig. 5.2. Starting from the upstream injection point, liquid L_1 begins to focus and detach from the upper and lower walls, becomes a thin thread and then folds in the diverging region. All of the subsequent simulations shown and analysed in the following sections use the full mesh resolution of $256 \times 64 \times 512$. Due to the high viscosity contrast and very low Reynolds number, each simulation took about 6 months of computing time on 64 cores of the parallel machine Ada (IBM x3750-M4) at the IDRIS computing center in Orsay, France (approximately 270 000 core hours per simulation).

cases	Re_1	ϕ	χ	α
1 (reference)	2.74×10^{-4}	1/12	2174	$\pi/2$
2	1.64×10^{-3}	1/12	2174	$\pi/2$
3	2.74×10^{-4}	1/12	1000	$\pi/2$
4	2.74×10^{-4}	1/5	2174	$\pi/2$
5	2.74×10^{-4}	1/12	2174	π

Table 5.2: Dimensional and nondimensional parameters for the 5 simulations

5.1 Thread formation

Recent advances in microfluidic technology have led to the emergence of micro total analysis systems (μ -TAS) or lab-on-a-chip (LOC) devices designed for biochemistry, biophysics and medical fields, including biological and chemical assays, drug delivery, drug screening for example (Whitesides and Stroock, 2001; Stone et al., 2004; Vilkner et al., 2004; Squires and Quake, 2005; Atencia and Beebe, 2005). The hydrodynamic focusing technique provides an effective means of controlling the passage of chemical reagent or bio-samples through microfluidic channels and has given rise to many studies aimed at understanding its physical mechanisms. Various flow-geometry relationships have been studied to create different effects, including the influence of the channel aspect ratio (Lee et al., 2006), the injection geometry for detaching the central stream from the walls (Simonnet and Groisman, 2005; Chang et al., 2007), the fluid driving mechanisms (Stiles et al., 2005) and the effect of small and moderate viscosity contrasts between the fluids (Wu and Nguyen, 2005).

In our simulations, the threads are also produced by hydrodynamic focusing. The liquid L_1 is injected from a central channel, and liquid L_2 that ensheath the liquid L_1 are introduced from side channels. Downstream from the junction, the fluids flow side by side, and the width

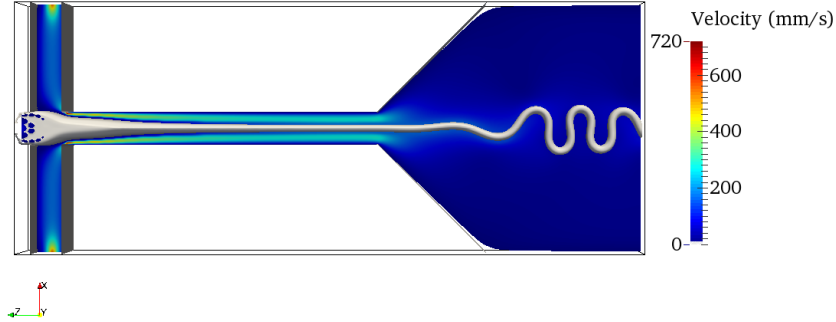
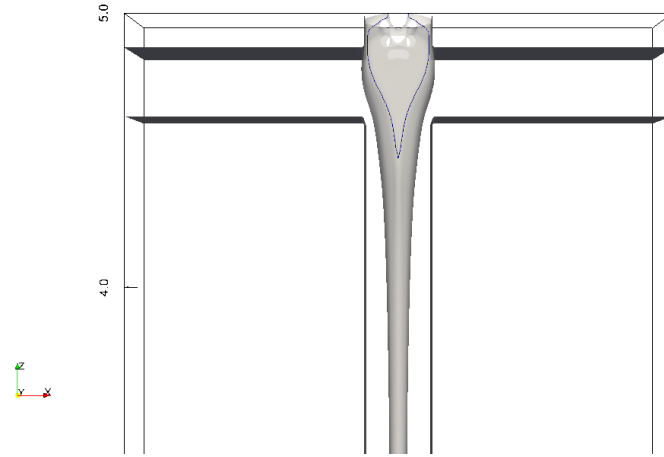


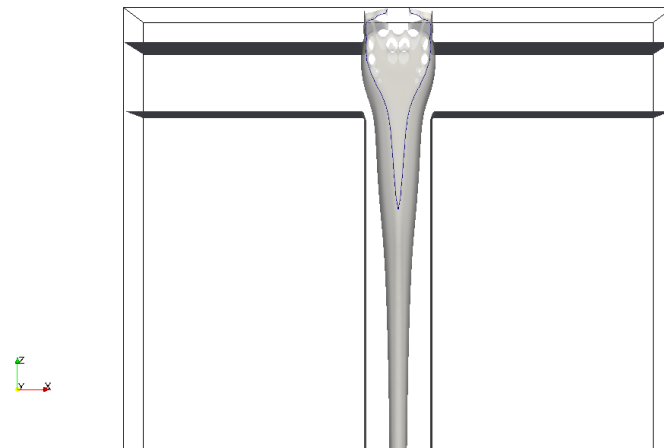
Figure 5.2: Velocity field on the channel midsurface with $Re_1 = 1.64 \times 10^{-3}$, $\chi = 2174$, $\phi = 1/12$ and $\alpha = \pi/2$ (case 2) using a low resolution $128 \times 32 \times 256$.

and location of the stream can be controlled through the injection flow rates. The more viscous liquid L_1 passes the junction and begins to detach from the top and bottom walls. The contact lines of different simulations are shown as the thin lines in Fig. 5.3. The irregular shapes on the thread near the inlet are due to graphical artefacts. The contact line has a ‘V’-like shape which is strongly stretched at the bottom. The hydrodynamic focusing depends on the viscosity ratio, the flow rate ratio and the Reynolds numbers. By contrast, the divergence angle α at the downstream part has almost no effect on the focusing, as shown in Fig. 5.3(a) and Fig. 5.3(d). When the viscosity ratio χ is low, the contact line becomes a true ‘V’ shape (Fig. 5.3(c)). The smaller flow flux rate ϕ and larger Reynolds number Re_2 lengthen the ‘V’ shape, i.e. the liquid L_1 takes longer to detach from the walls and form the thread.

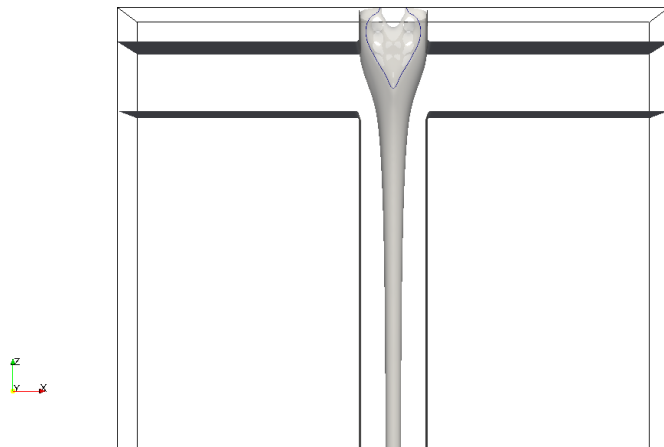
Fig. 5.4 shows cross sections across the channel width and the chan-



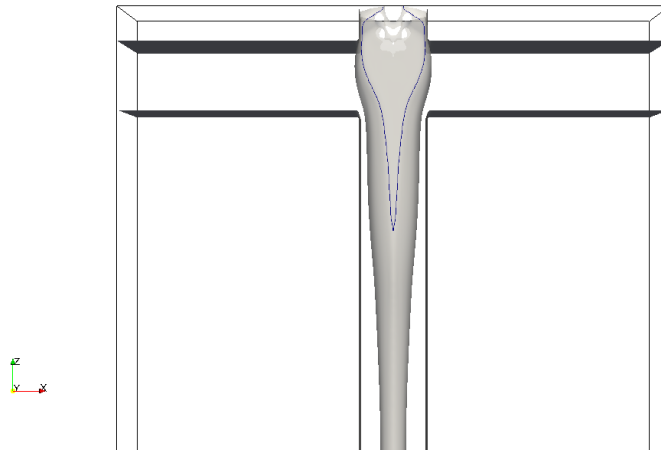
(a) case 1



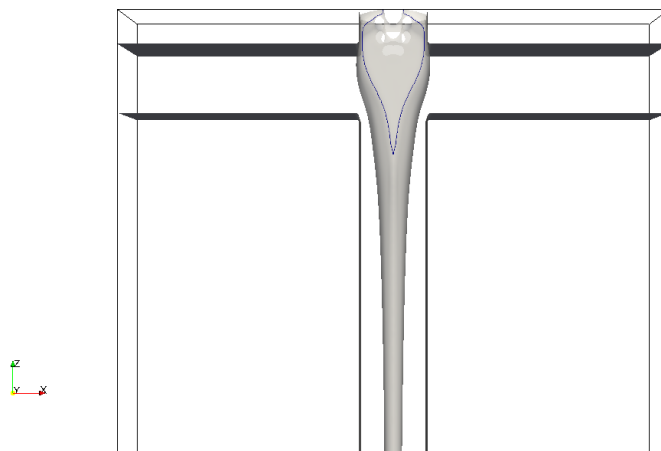
(b) case 2



(c) case 3



(d) case 4



(e) case 5

Figure 5.3: Formation of viscous threads by hydrodynamic focusing and contact line detachment (thin lines) from the channel walls. The irregular shapes on the thread near the inlet are due to graphical artefacts.

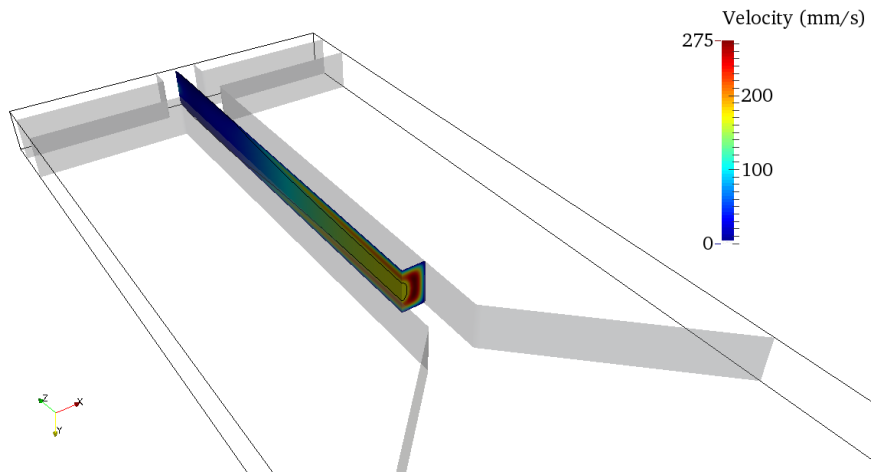
nel depth of the three-dimensional velocity fields of hydrodynamic focusing (case 2). The liquid jet L_1 detaches from the walls, becomes thinner, and then forms a thread. Moreover, the flow of the liquid L_1 in the long microchannel is a plug flow and ensheathed by liquid L_2 .

To analyse the focusing process more clearly, four cross sections across the depth at different positions $z = 2.2$ mm, $z = 2.5$ mm, $z = 3$ mm, $z = 4$ mm are shown in Fig. 5.5. The liquid L_1 flows at an almost uniform velocity (plug flow) at the beginning of hydrodynamic focusing and is accelerated by the side flow. The thread becomes thinner (from Fig. 5.5(a) to Fig. 5.5(c)) and then is nearly stable (from Fig. 5.5(c) to Fig. 5.5(d)). Similarly, from $z = 4$ mm to $z = 2.2$ mm, the velocity contour changes dramatically at first, then slowly and at last becomes almost stable. Furthermore, the cross section of the thread is an ellipse rather than a circle. The minor axis of the thread ϵ_1 and the major axis of the thread ϵ_2 along the flow direction up to the diverging point are plotted in Fig. 5.6. From Fig. 5.6, the stable minor axis and major axis of the thread are $\epsilon_1 = 0.0565$ and $\epsilon_2 = 0.103$. Also, we find that liquid L_1 detaches completely from the walls at the distance $z = 4.2$ mm. The minor axis and major axis of the thread as well as the ratios ϵ_1/w , ϵ_2/w and ϵ_1/ϵ_2 for all 5 cases are listed in Table 5.3.

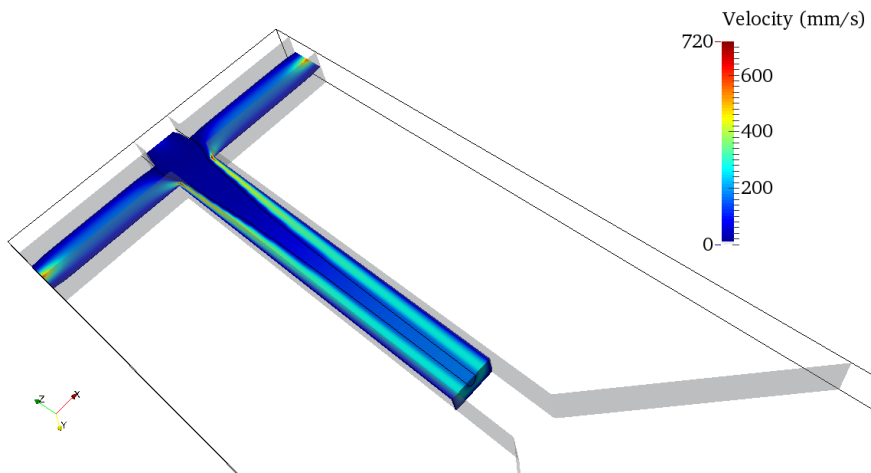
cases	ϵ_1	ϵ_2	ϵ_1/w	ϵ_2/w	ϵ_1/ϵ_2	ϵ_s/w
1 (base case)	0.0573	0.0836	0.2292	0.3344	0.69	0.06
2	0.0565	0.103	0.226	0.412	0.55	0.073
3	0.0578	0.057	0.2312	0.228	1.01	0.041
4	0.088	0.111	0.352	0.444	0.793	0.123
5	0.064	0.088	0.256	0.352	0.73	0.0707

Table 5.3: The stable ϵ_1 , ϵ_2 , ϵ_1/w , ϵ_2/w and ϵ_1/ϵ_2 for all 5 cases

The velocity profile for the annular flow in a circular tube can be di-



(a) cross section across the channel depth



(b) cross section across the channel width

Figure 5.4: Three-dimensional velocity fields of hydrodynamic focusing with $Re_1 = 1.64 \times 10^{-3}$, $\phi = 1/12$, $\chi = 2174$, $\alpha = \pi/2$ (case 2) showing cross section across the channel width and cross section across the channel depth. The black line is the thread interface.

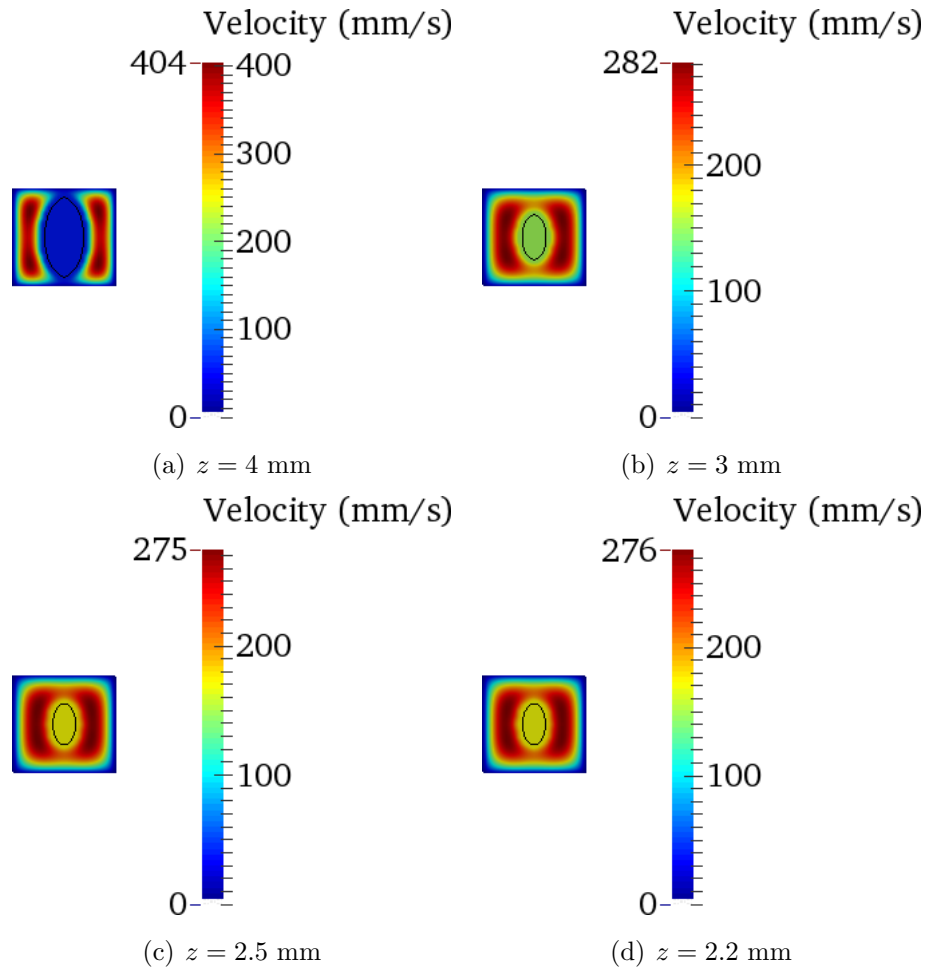


Figure 5.5: The velocity contour of cross sections across the depth at different positions $z = 2.2$ mm, $z = 2.5$ mm, $z = 3$ mm, $z = 4$ mm for case 2 ($\text{Re}_1 = 1.64 \times 10^{-3}$, $\phi = 1/12$, $\chi = 2174$, $\alpha = \pi/2$), the black line is the thread interface.

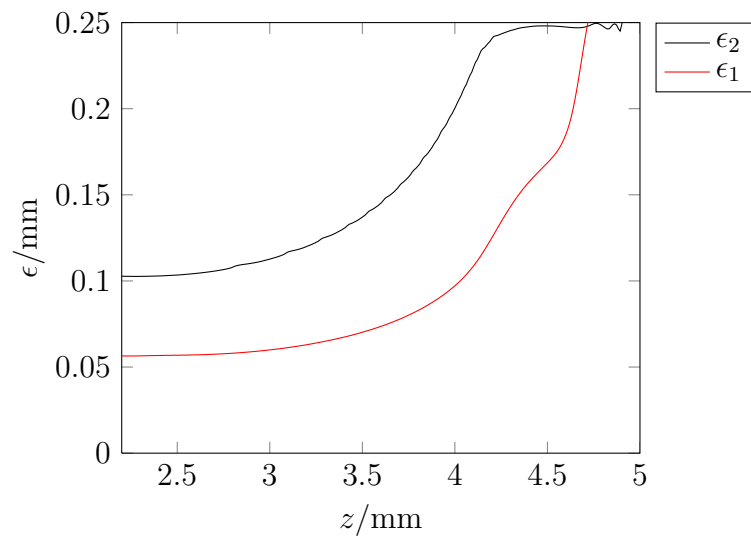


Figure 5.6: The minor axis ϵ_1 and major axis ϵ_2 of the thread along the flow direction for case 2 ($\text{Re}_1 = 1.64 \times 10^{-3}$, $\phi = 1/12$, $\chi = 2174$, $\alpha = \pi/2$)

rectly calculated from the Stokes equations (Joseph and Renardy, 1993). Its dimensionless form is:

$$u_1 = \frac{1}{\chi}(c^2 - r^2) + 1 - c^2, \quad \text{for } 0 \leq r \leq c, \quad (5.7)$$

$$u_2 = 1 - r^2, \quad \text{for } c \leq r \leq 1, \quad (5.8)$$

where the radial coordinate r and the core radius c are normalized by R , and $u_i = V_i(4\eta_2)/[(\nabla P)R^2]$ is the dimensionless velocity in region i , ∇P is the pressure gradient, and V_i is the velocity in region i . The relationship between c and the flow rate ratio $\phi = Q_1/Q_2$ of each liquid is calculated by integrating equations (5.7) and (5.8) across the area of each region, yielding:

$$\phi = \frac{c^4(\chi^{-1} - 2) + 2c^2}{(1 - c^2)^2}. \quad (5.9)$$

In the regime associated with small threads $c \ll 1$ and large viscosity ratios $\chi \ll 1$, a simple scaling for the thread can be found: $c \sim (\phi/2)^{0.5}$. Although this analysis is only valid for a circular tube, it gives a simple estimate for the behavior of core annular flows as a function of the viscosity contrast. For the case of a square microchannel of width w , $c = \epsilon_c/w$ for comparing circular diameter and square cross section instead of $c = \epsilon_c/R$ is used to show the relation between c and ϕ . Here in our simulations the thread cross section is an ellipse, both ϵ_1/w and ϵ_2/w are compared with the prediction ϵ_c/w based on circular cross section assumption. Cubaud's experiments (Cubaud and Mason, 2006a) suggest that the thread minor-axis (diameter) ϵ_1/w was independent of χ and followed $\epsilon_1/w \sim \phi^{0.6}$. In Cubaud's experiments they took photos from above with a high speed camera, so that only the minor-axis (diameter) ϵ_1 of the thread could be measured (Thus it is not clear whether the thread cross section was circular or not). In Fig. 5.7, the estimating lines $\epsilon_c/w \sim (\phi/2)^{0.5}$, $\epsilon_1/w \sim \phi^{0.6}$ and values ϵ_1/w , ϵ_2/w from our simulations

are presented. When ϕ is small, the two power-law predictions are close. The slope of ϵ_1/w from our simulation results agree well with both power-law relationships $\epsilon_1/w \sim \phi^{0.6}$ and $\epsilon_c/w \sim (\phi/2)^{0.5}$. But for the major axis ϵ_2 of the thread, it seems more complicated: ϵ_2/w depends on not only the flow rate ratio ϕ but also other parameters such as the viscosity ratio χ . With the same ϕ , the lower viscosity ratio χ decreases the semi major axis and the thread cross section looks more circular.

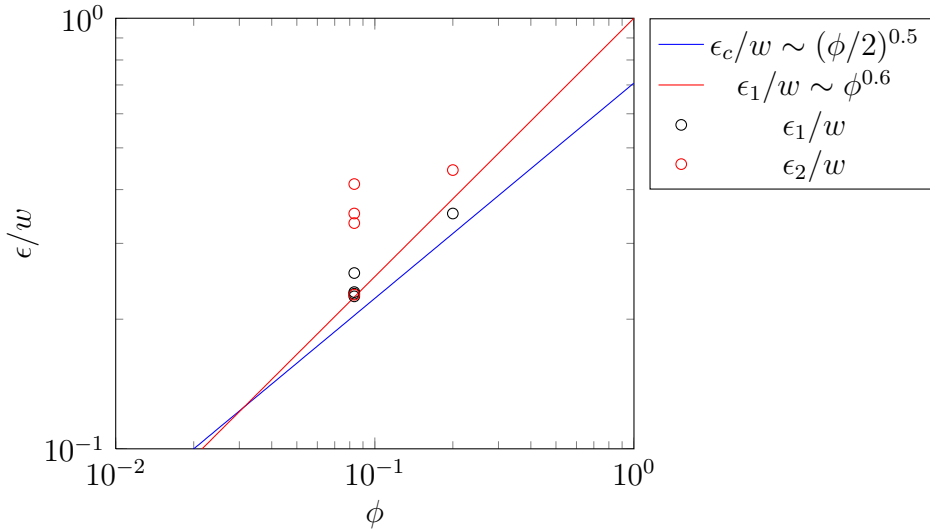


Figure 5.7: Downstream evolution of core diameter ϵ/w versus flow rate ratio ϕ for a thread in plug flow in a square microchannel. The red and blue lines are the power-law predictions, the circle marks are our simulation results.

Lee et al. (2006) analyzed theoretically the hydrodynamic focusing effect inside rectangular microchannels. According to their study, the relationship between ϵ/w and ϕ is

$$\frac{\epsilon}{w} = \frac{\phi}{\lambda(\phi + 1)}, \quad (5.10)$$

λ is a parameter depending on the aspect ratio of the rectangular microchannel Λ and the width of the focused stream ϵ . Two particular cases exist for pressure-driven flow in rectangular channels. The first case involves an aspect ratio of $\Lambda \rightarrow \infty$. In this case, a parabolic velocity profile is formed across the channel width and is independent of the position across the channel height. Under these conditions, $\lambda = 1.5$, assuming $\epsilon/w \ll 1$. The second case involves an aspect ratio $\Lambda \rightarrow 0$. In this case, a parabolic velocity profile is formed across the channel height and is independent of the position across the channel width, $\lambda = 1.0$. It is noted that in the study of Lee et al. (Lee et al., 2006) the sample liquid L_1 didn't detach from the top and bottom walls. Once the liquid L_1 detaches from the walls, its width will become larger due to surface tension. To compare our results with Lee's study, the equivalent widths ϵ_s are calculated (a rectangle $\epsilon_s \times w$ with the same area) and ϵ_s/w is listed in Table 5.3. In our simulations, the aspect ratio of the microchannel is $\Lambda = 1$ between these two particular cases. In Fig. 5.8, the two limiting relations and the results of our simulations are plotted. It is apparent that a good agreement exists between the two sets of results.

5.2 Folding instability

The thread produced by hydrodynamic focusing continues to flow in the diverging region and a folding instability appears as shown in Fig. 5.2. The velocity profile before the diverging point has an important effect on the folding instability. According to the discussion above, the velocity field becomes almost stable near the diverging point. So we can fix the cross section at the position $z = 2.5$ mm to compare the velocity profiles of different cases.

Fig. 5.9 shows the flow patterns at different times for the reference

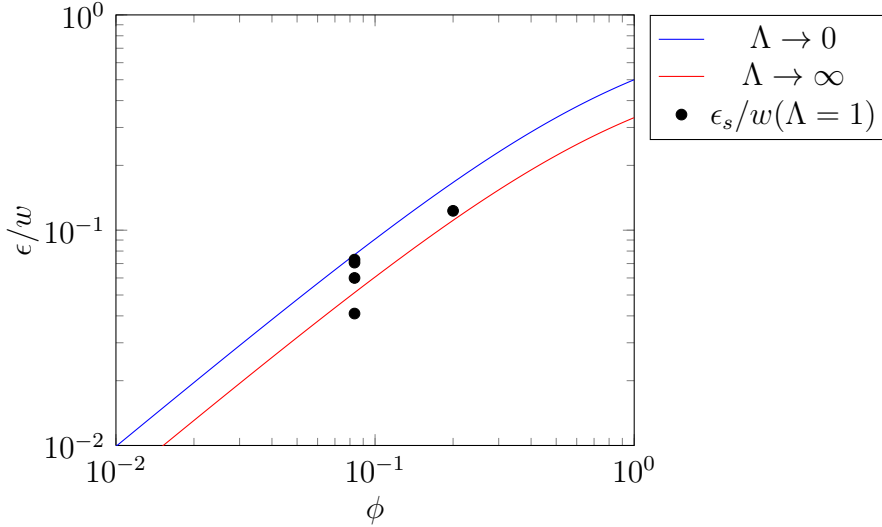
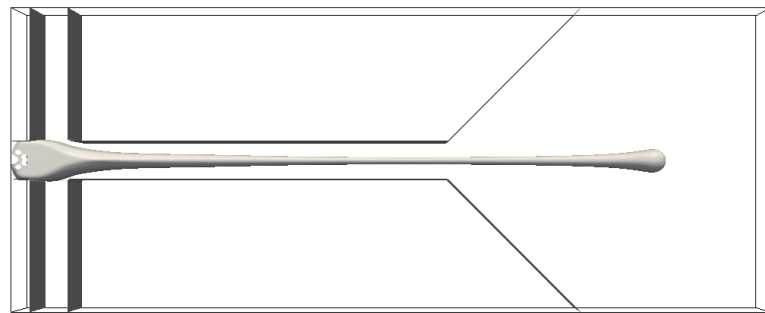


Figure 5.8: Evolution of core diameter ϵ/w versus flow rate ratio ϕ for a thread in plug flow in a square microchannel.

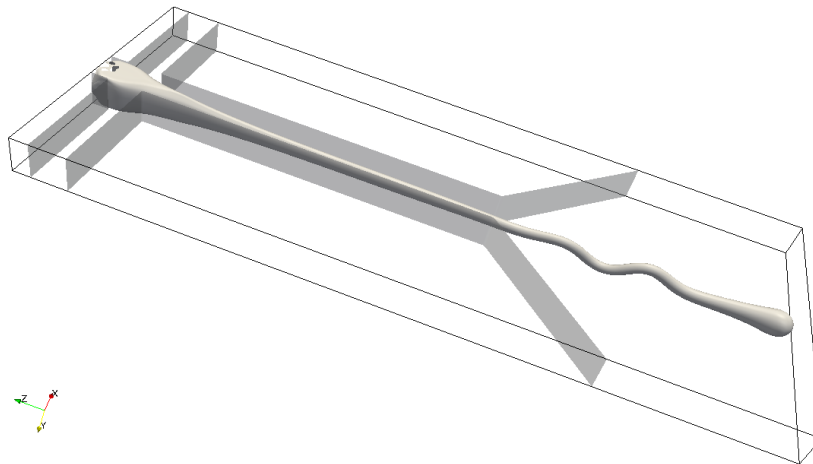
case 1 with $\text{Re}_1 = 2.74 \times 10^{-4}$, $\phi = 1/12$, $\chi = 2174$, $\alpha = \pi/2$. The thread begins to fold about an axis in the y -direction in Fig. 5.9(b), and then the folding plane rotates in Fig. 5.9(c). The folding slowly transforms from the y -direction to the x -direction. In Fig. 5.9(d) the new folds appear mainly in the x -direction. The velocity profiles along the mid-line (x -direction) of the cross section at $z = 2.5$ mm are shown in Fig. 5.10.

The plots at different times in Fig. 5.10 suggest that the velocity profile changes slightly at the onset of the buckling instability and then become stable again. (The plug flow velocity of liquid L_1 increases slightly when the buckling starts.) Although similar figures for the other four cases are not shown here, the same trend exists for all five cases.

In other simulation cases, the flow patterns are different from the base simulation case 1. For simulation case 2 ($\text{Re}_1 = 1.64 \times 10^{-3}$, $\phi =$



(a) $t = 0.178\text{s}$



(b) $t = 0.198\text{s}$

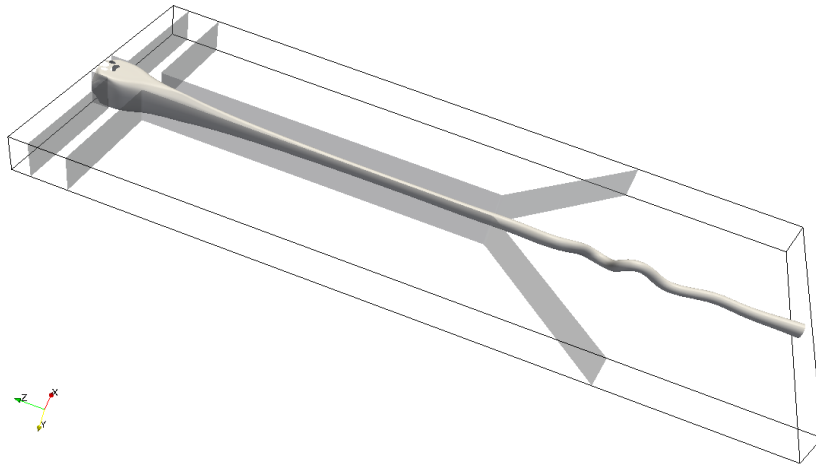
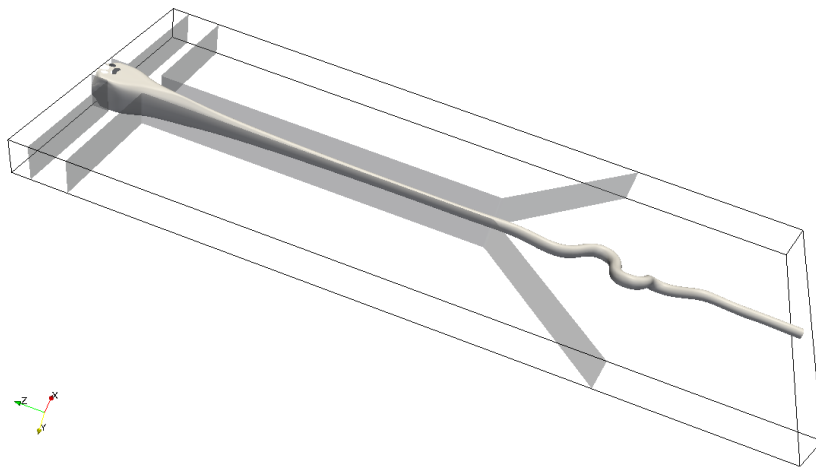
(c) $t = 0.213\text{s}$ (d) $t = 0.228\text{s}$

Figure 5.9: The flow patterns at different times for case 1 with $\text{Re}_1 = 2.74 \times 10^{-4}$, $\phi = 1/12$, $\chi = 2174$, $\alpha = \pi/2$.

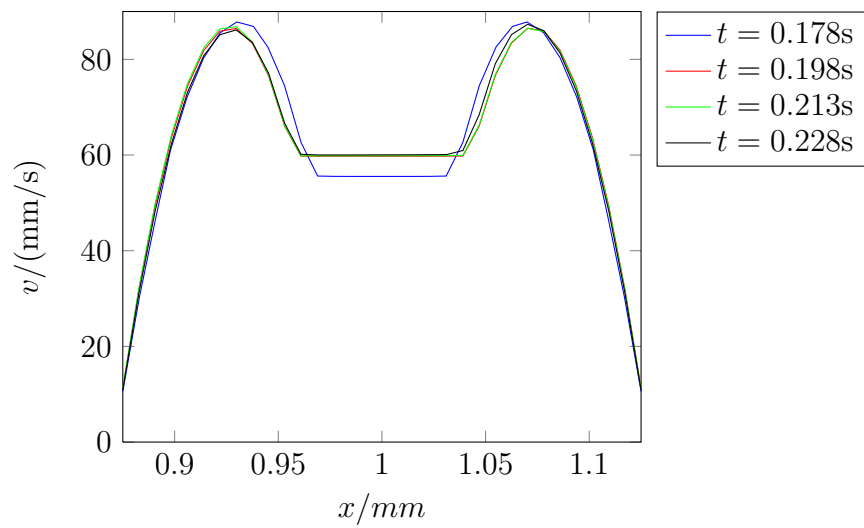


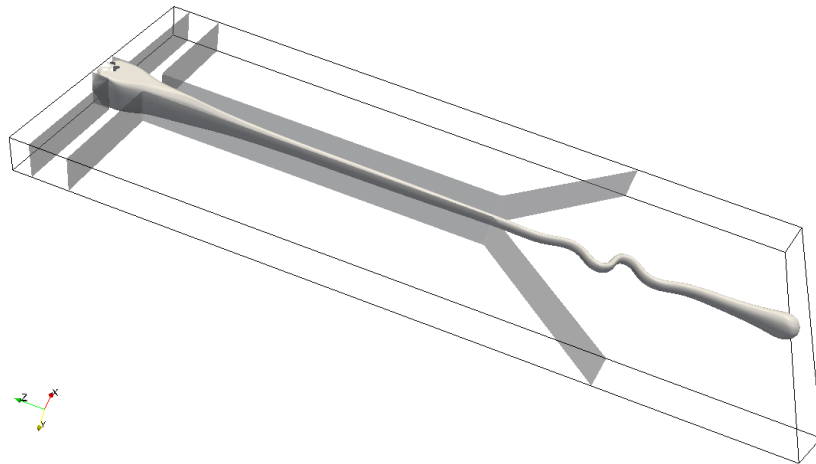
Figure 5.10: The velocities along the middle line of the cross section at $z = 2.5$ mm at different times corresponding to the flow patterns in Fig. 5.9.

$1/12, \chi = 2174, \alpha = \pi/2$), as shown in Fig. 5.11(a), the thread begins to fold in the x -direction. The folding frequency and amplitude then vary slightly after the thread exits the computation domain in Fig. 5.11(b), and finally, the folding frequency and amplitude become stable in Fig. 5.11(d) and 5.11(e). It is noted that the folding only happens in the x -direction.

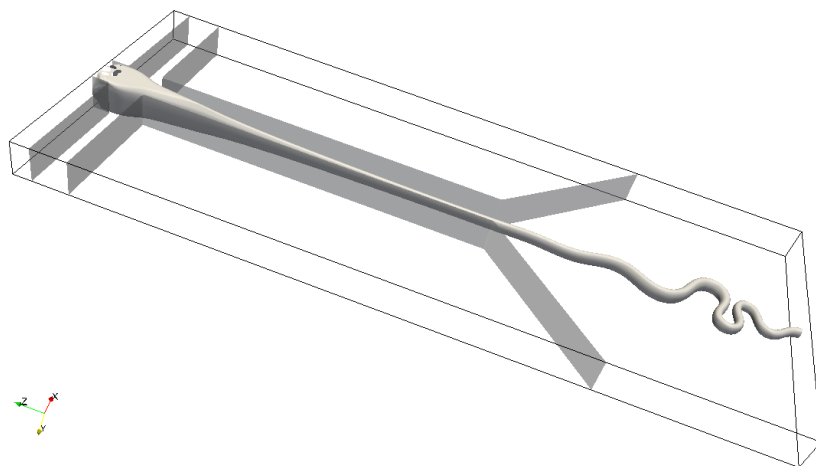
In case 3 with $\text{Re}_1 = 2.74 \times 10^{-4}, \phi = 1/12, \chi = 1000, \alpha = \pi/2$, the onset of folding appears in the y -direction in Fig. 5.12(b). For this case, there are not only folding instability but also strong shrinking when the thread suffers the compressible stress. The thread is squeezed, so that the thread becomes fatter and the folding wavelength decreases as the thread flows downstream (from Fig. 5.12(b) to 5.12(c)). Consequently, the amplitude of newly appearing folds decreases to 0 slowly and its wavelength becomes larger. Finally, the folding phenomenon disappears and the thread is completely straight.

When $\text{Re}_1 = 2.74 \times 10^{-4}, \phi = 1/12, \chi = 2174, \alpha = \pi$ in case 5, the folding instability occurs in the y -direction then twists towards the x -direction in Fig. 5.13. This is similar to the phenomenon in reference case 1, transition from folding in the y -plane to the x -plane.

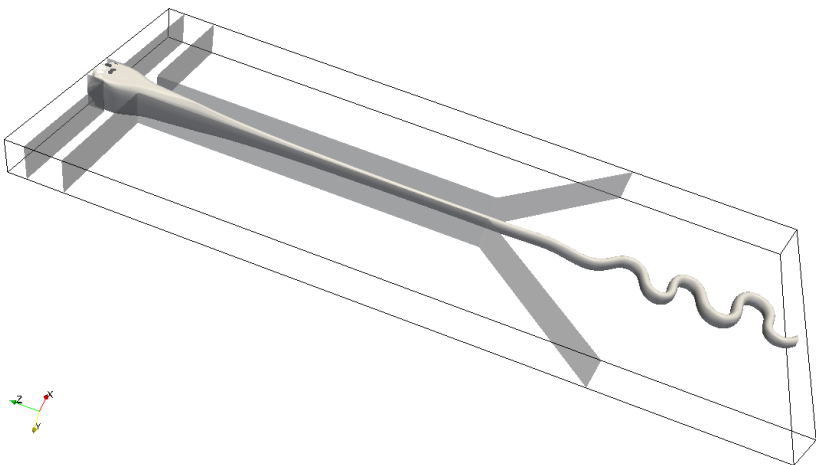
It is assumed that the different patterns of folding or buckling depend on the velocity profile and the thread shape on the cross section. As discussed above the velocity profile is stable after the onset of buckling, the velocity contours and the interface between the thread L_1 and surrounding fluid at $z = 2.5$ mm are presented in Fig. 5.14. The velocities along the mid-line (depth, y -direction) and the center line (width, x -direction) are plotted in Fig. 5.15. The folding is induced by the viscous compressional stress. The velocity of the flow in the long focusing channel and near the diverging point is nearly in the z -direction, i.e.



(a) $t = 0.066\text{s}$



(b) $t = 0.079\text{s}$



(c) $t = 0.085\text{s}$

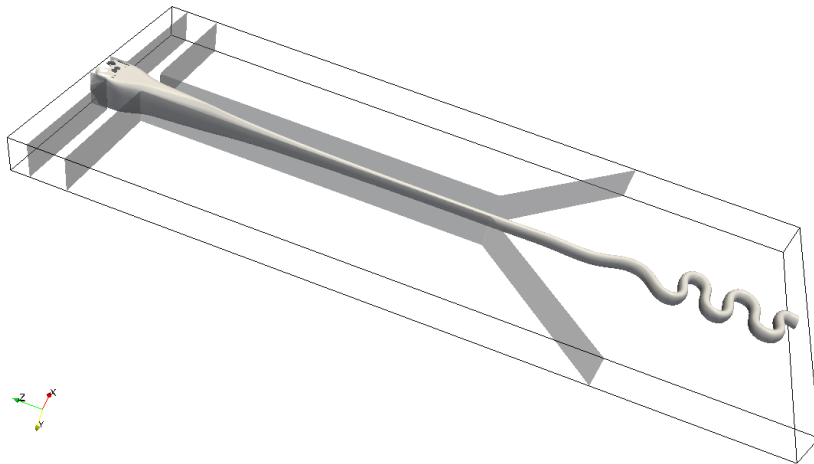
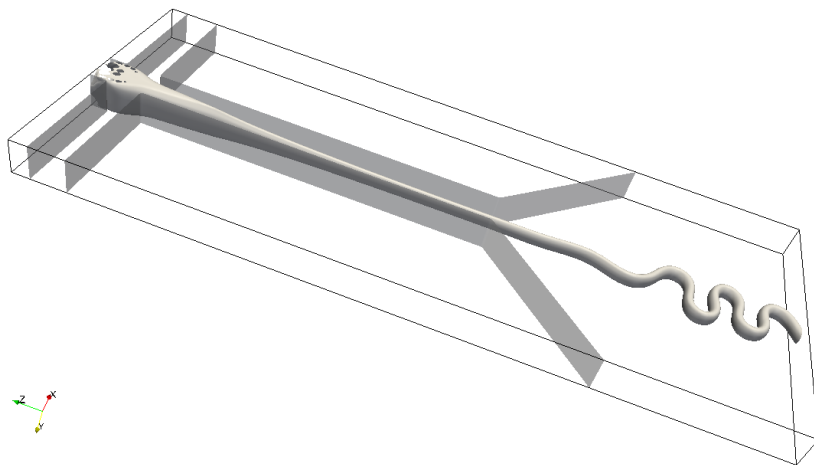
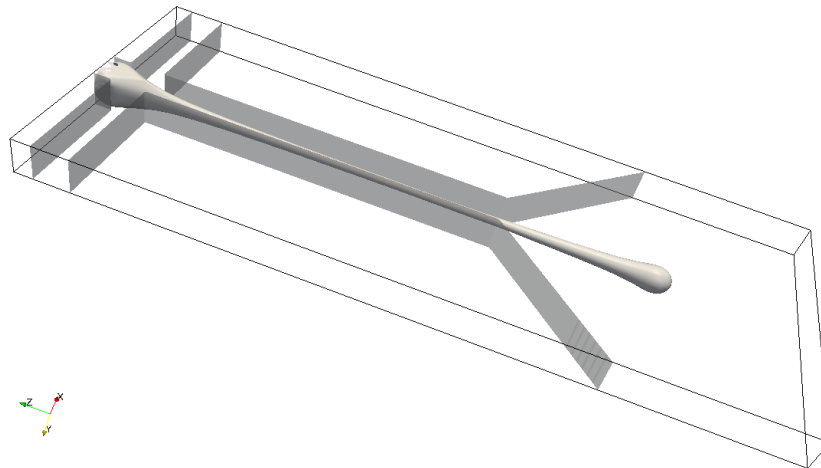
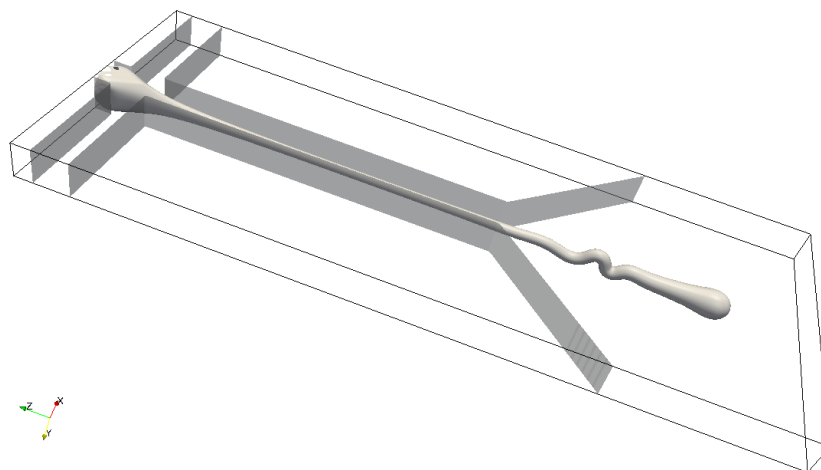
(d) $t = 0.106\text{s}$ (e) $t = 0.146\text{s}$

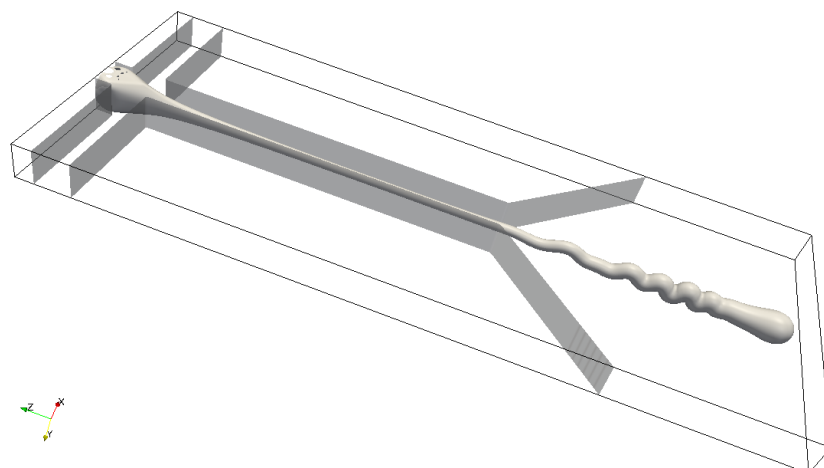
Figure 5.11: The flow patterns at different times for case 2 with $\text{Re}_1 = 1.64 \times 10^{-4}$, $\phi = 1/12$, $\chi = 2174$, $\alpha = \pi/2$.



(a) $t = 0.123\text{s}$



(b) $t = 0.144\text{s}$



(c) $t = 0.181\text{s}$

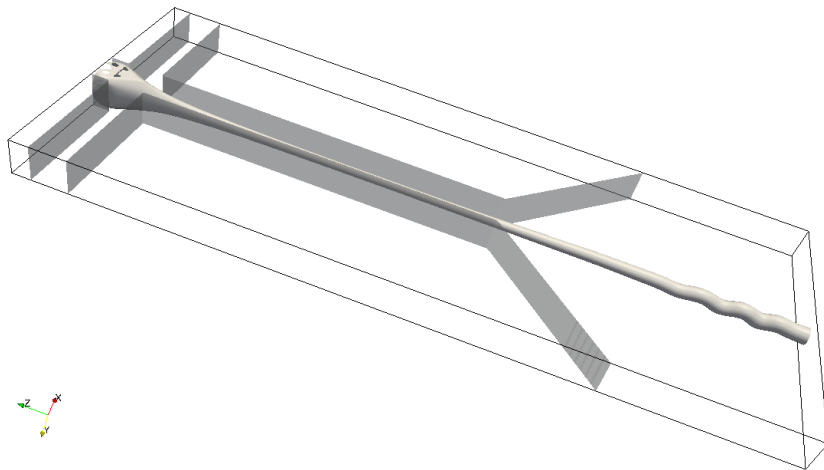
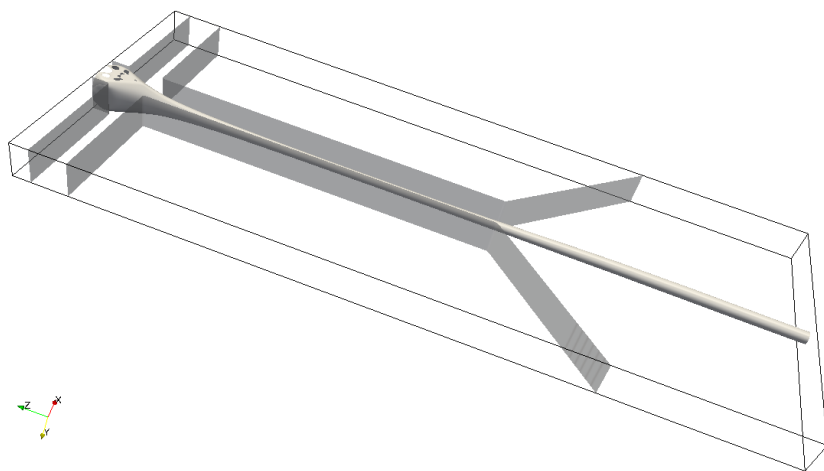
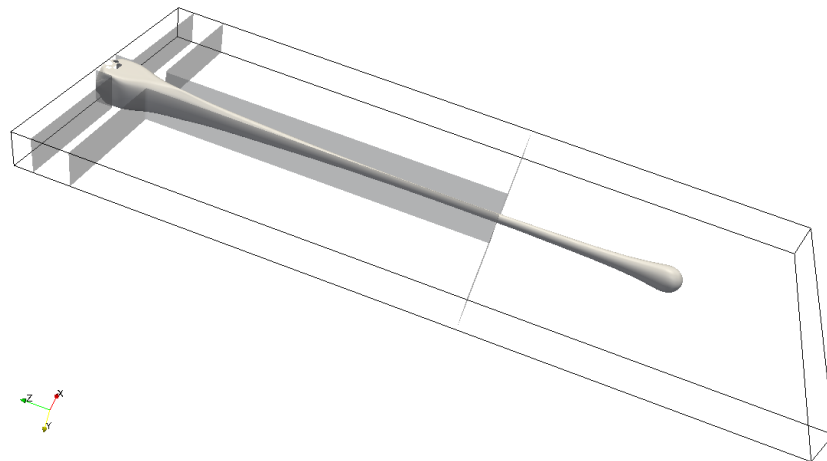
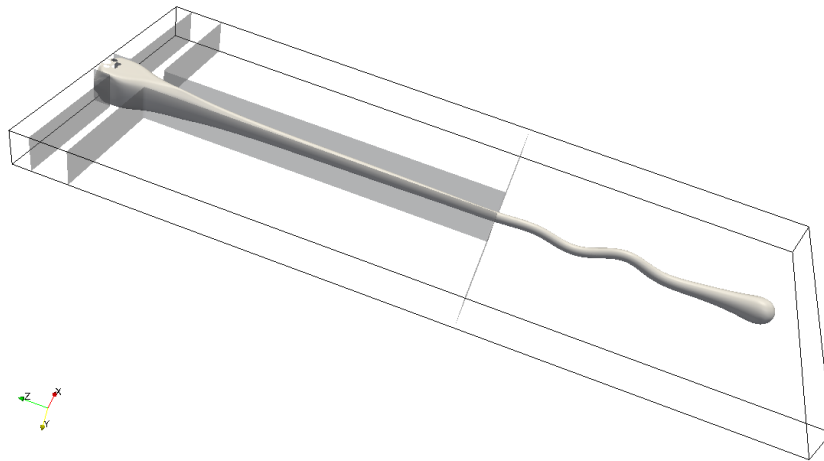
(d) $t = 0.219\text{s}$ (e) $t = 0.239\text{s}$

Figure 5.12: The flow patterns at different times for case 3 with $\text{Re}_1 = 2.74 \times 10^{-4}$, $\phi = 1/12$, $\chi = 1000$, $\alpha = \pi/2$.



(a) $t = 0.173s$



(b) $t = 0.193s$

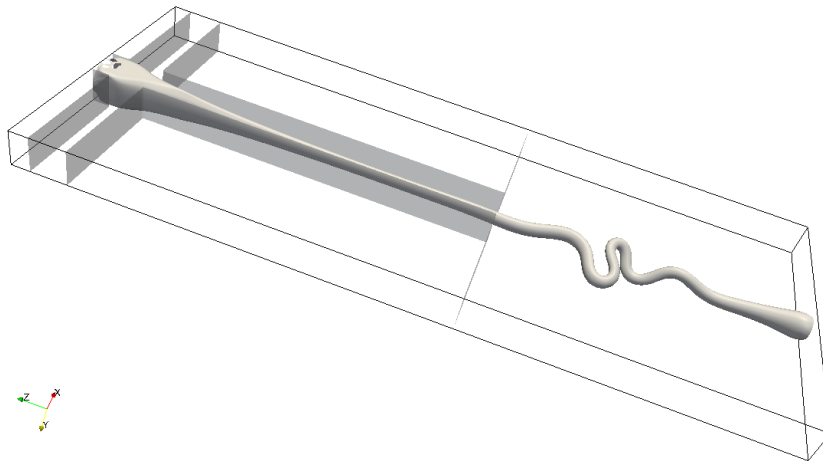
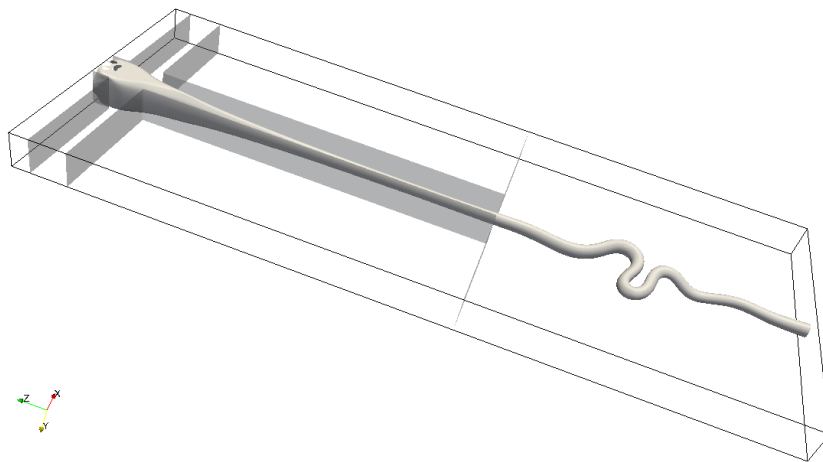
(c) $t = 0.215\text{s}$ (d) $t = 0.224\text{s}$

Figure 5.13: The flow patterns at different times for case 5 with $\text{Re}_1 = 2.74 \times 10^{-4}$, $\phi = 1/12$, $\chi = 1000$, $\alpha = \pi$

$\mathbf{u} = (0, 0, u_z)$. Thus the non-zero components in the viscous stress are

$$\sigma_{xz} = \frac{1}{2}\eta_i \frac{\partial u_z}{\partial x}, \quad (5.11)$$

$$\sigma_{yz} = \frac{1}{2}\eta_i \frac{\partial u_z}{\partial y}, \quad (5.12)$$

$$\sigma_{zz} = -p + \eta_i \frac{\partial u_z}{\partial z}, \quad (5.13)$$

where η_i is the viscosity of liquid L_1 or L_2 . On the cross section of the thread the viscous stress is longitudinal stress, $\sigma_{xz} = \sigma_{yz} = 0$ due to the plug flow. In Chung's study (Chung et al., 2010), the longitudinal stress is defined as $2\eta_i u_z / 0.5w$ along the centerline. In their Fig. 4(d) (Chung et al., 2010), the longitudinal stress is highly compressional. Here, our simulations are 3-dimensional, the longitudinal stress is proportional to the derivatives $\partial u_z / \partial z$. The derivatives $\partial u_z / \partial z$ of the velocity u_z with respect to z along the thread are shown in Fig. 5.16, it is clear the longitudinal stress is compressional in the diverging region, especially near the diverging point.

On the thread interface, the viscous force per unit area by liquid L_2 can be obtained by $\boldsymbol{\sigma} \cdot \mathbf{n}$, where \mathbf{n} is the unit normal vector to the interface. Since the major axis and minor axis become stable near the diverging point, the unit normal vector is in the x - y plane $\mathbf{n} = (n_x, n_y, 0)$. Thus, the viscous force per unit area on the interface is

$$\mathbf{f}_{in} = \boldsymbol{\sigma} \cdot \mathbf{n} = (0, 0, \sigma_{xz}n_x + \sigma_{yz}n_y) = \frac{1}{2}\eta_2(0, 0, \frac{\partial u_z}{\partial n}). \quad (5.14)$$

The viscous force on the interface is proportional to the normal derivative $\partial u_z / \partial n$. Then the bending moment on the cross section of the thread induced by the viscous force on the interface can be calculated,

it has two components

$$\omega_x = \frac{1}{2}\eta_2 \int_C \frac{\partial u_z}{\partial n} (y(s) - y_c) ds, \quad (5.15)$$

$$\omega_y = \frac{1}{2}\eta_2 \int_C \frac{\partial u_z}{\partial n} (x(s) - x_c) ds. \quad (5.16)$$

Where the integrals are done along the bounding line of cross section C , x_c, y_c are the coordinates of the center on the cross section. Here the bending moment is presented by the integral part, i.e. $M_x = 2\omega_x/\eta_2$ and $M_y = 2\omega_y/\eta_2$. For case 1 with $\text{Re}_1 = 2.74 \times 10^{-4}$, $\phi = 1/12$, $\chi = 2174$, $\alpha = \pi/2$, the bending moments of the thread M_x and M_y on the cross section at $z = 1.7$ mm are plotted from the onset of the folding instability in Fig. 5.17. At first the moment M_x dominates, the cross section rotates about the x -axis resulting in folding in the y -direction. And then the moment M_y increases, the folding slowly transforms via twisting to folding in the x -direction. When the ratio ϵ_1/ϵ_2 of the thread is much less than 1 the moment M_x is always very small compared to M_y , so that the folding only appears in the x -direction. This is just what we observe in simulation case 2 (similar bending moments over time are presented in Fig. 5.18).

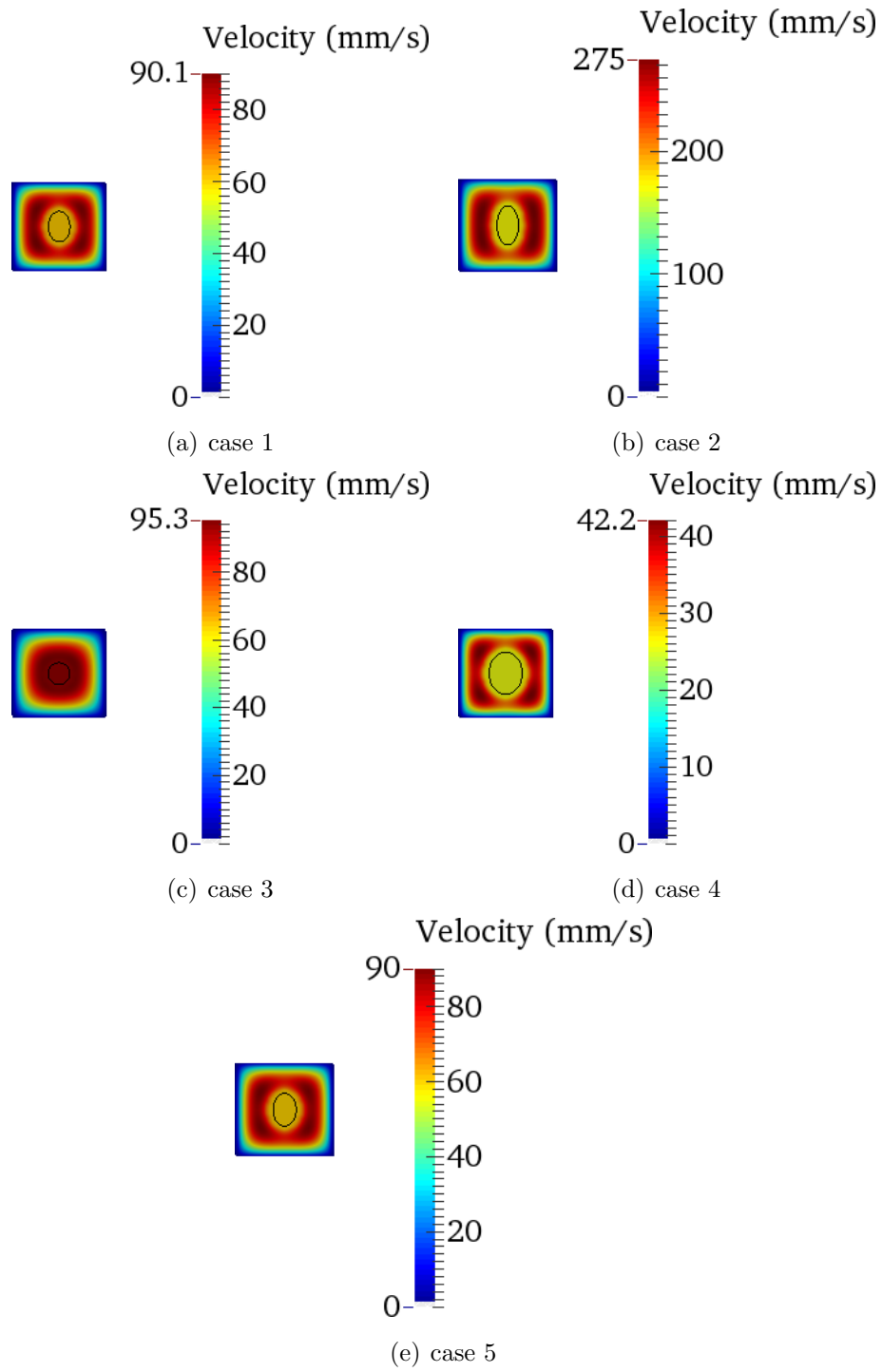


Figure 5.14: The velocity contour and thread shape (black line) at $z = 2.5$ mm before the diverging point for the 5 cases

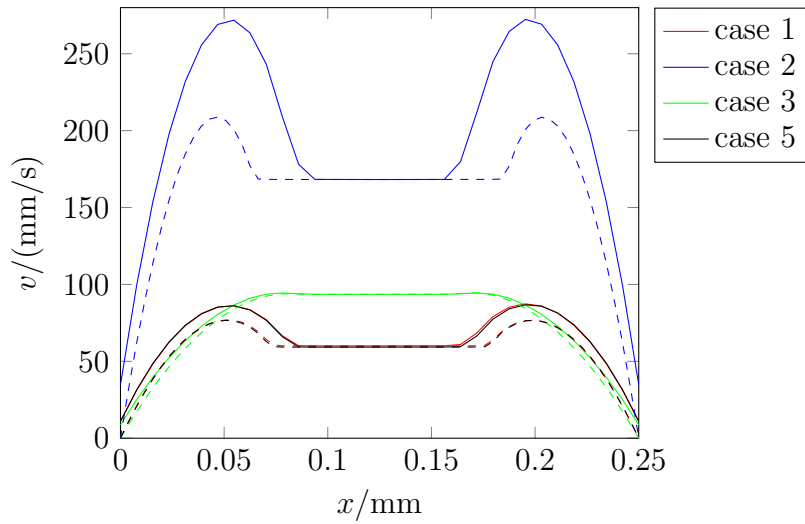


Figure 5.15: The velocities along the center line (solid line) and mid-line (dashed line) on the cross section at $z = 2.5$ mm for different cases.

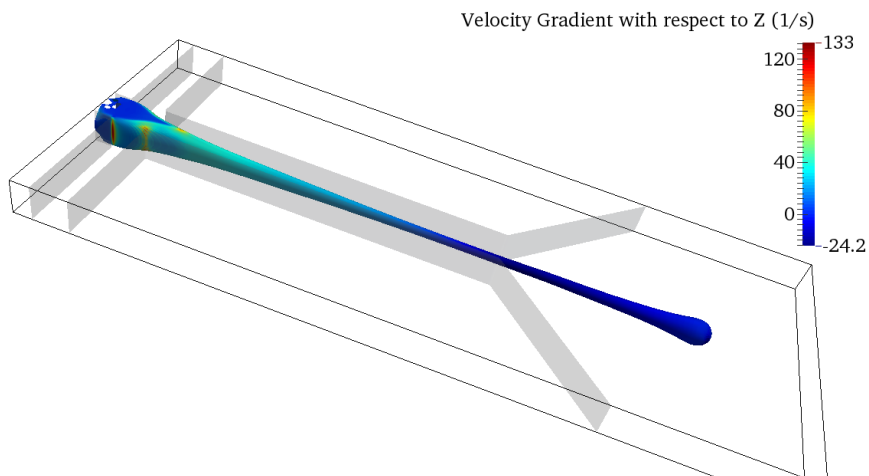
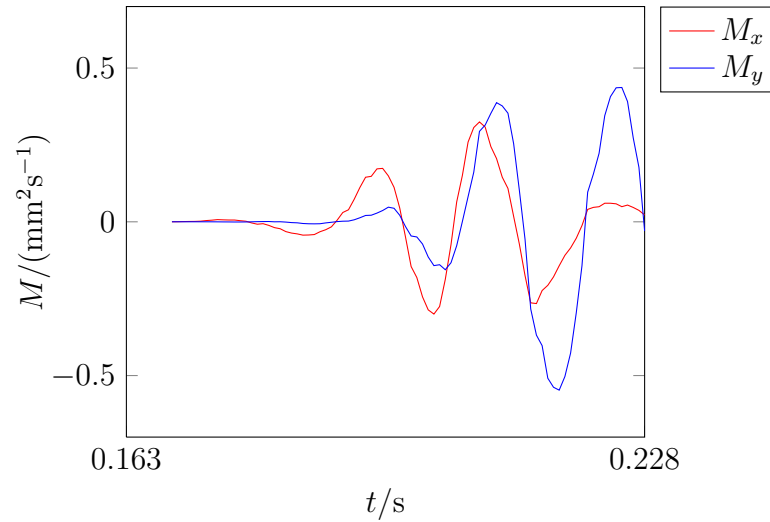
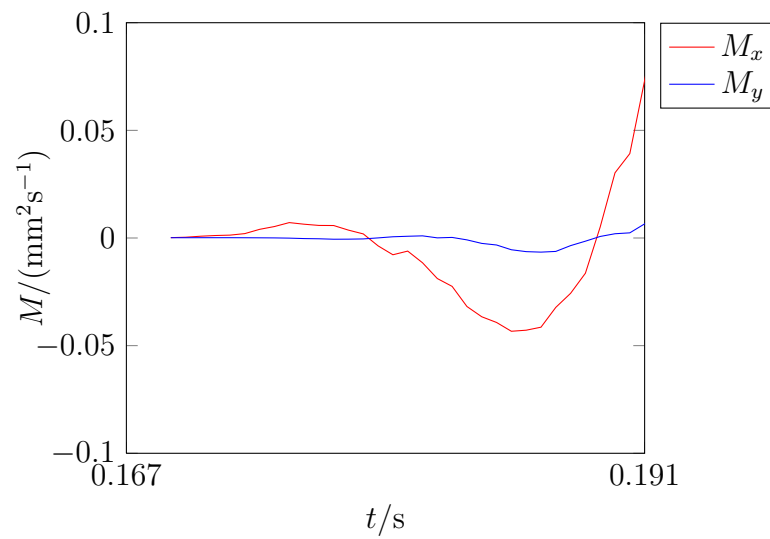


Figure 5.16: The derivatives $\partial v_z / \partial z$ of the velocity v_z on the thread interface before onset of folding at $t = 0.178$ s for case 1 with $\text{Re}_1 = 2.74 \times 10^{-4}$, $\phi = 12$, $\chi = 2174$, $\alpha = \pi/2$.



(a) From $t = 0.163$ s to $t = 0.228$ s



(b) From $t = 0.167$ s to $t = 0.191$ s

Figure 5.17: The bending moment at $z = 1.7$ mm for case 1 with $\text{Re}_1 = 2.74 \times 10^{-4}$, $\phi = 1/12$, $\chi = 2174$, $\alpha = \pi/2$ when the folding instability occurs.

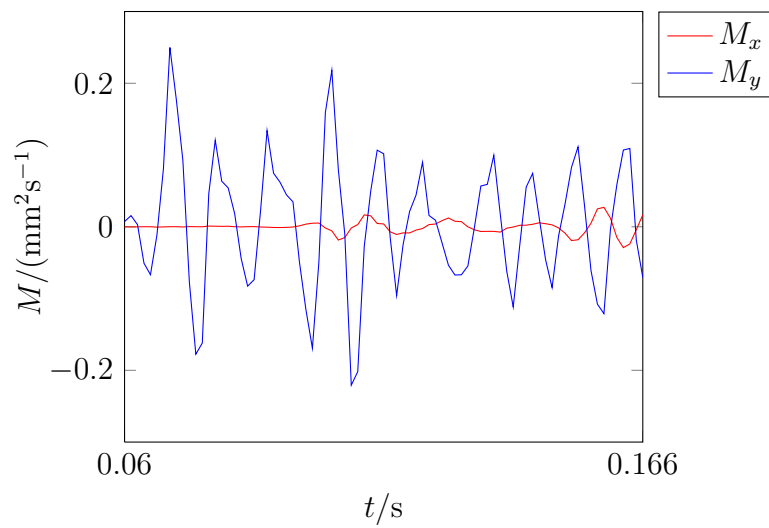


Figure 5.18: The bending moment at $z = 1.7$ mm for case 2 with $\text{Re}_1 = 1.64 \times 10^{-3}$, $\phi = 1/12$, $\chi = 2173$, $\alpha = \pi/2$ when the folding instability occurs.

Chapter 6

Conclusion

6.1 Summary of results obtained

In this thesis, we have investigated the hydrodynamics of thin (sheet-like) and slender (filamentary) bodies of viscous fluid immersed in a second fluid. The viscosity ratio of the two fluids could be very large, up to more than 1000. Two examples were studied: the subduction of oceanic lithosphere on Earth, and viscous folding in diverging microchannels. Though their physical scales are very different, there is a common characteristic Reynolds number $Re \ll 1$ for both cases. Thus inertia can be neglected in the dynamics.

To model the subduction of oceanic lithosphere, we studied the two-dimensional subduction of a thin viscous sheet in a half-space of another fluid, bounded above by an impermeable free-slip surface (i.e., a plane of mirror symmetry). By combining the force balance for the thin sheet with a boundary integral representation of the outer flow, a hybrid boundary integral-thin sheet method (BITS) is built in the form of an integral equation for the velocities on the sheet's midsurface. To solve this equation, a discrete approach is implemented by adapting a

discrete model for thin viscous threads developed by B. Audoly and co-workers Audoly et al. (2013). In the discrete approach, all the variables are represented in a Lagrangian framework and the Rayleigh dissipation potential (Torby, 1984) is introduced to describe the internal viscous stress in the sheet. An asymptotic thin-sheet formulation is used to derive the expressions of both stretching and bending dissipation potentials during subduction. Finally, the integral equation is rewritten as a matrix equation for the velocities on the discrete vertices along the sheet's midsurface. Given the sheet's geometry, the instantaneous (quasi-static) velocity on the midsurface is obtained by solving the matrix equation.

To validate BITS, we first compared our predictions for a vertical sheet with the results of a full boundary-element method (BEM), and found reasonable agreement consistent with the errors introduced by the thin-sheet approximation. To handle the weakly singular kernel in the BITS equation, we used both an integral average procedure and the method of regularized Stokeslets (Cortez, 2001). For the vertical sheet, both methods work well, and the predictions with the regularized Stokeslet agree with those obtained using the integral average when the characteristic radius of the regularized Stokeslet tends to zero. We also analyzed the effect of the discretization on the vertical sheet solution, finding that BITS shows good convergence as the number of elements increases. We then considered a horizontal sheet, and found that the BITS method performed well compared to the BEM solutions. However, when the sheet's distance from the free surface is small, higher resolution is required to obtain accurate solutions. Moreover, the solutions failed to converge using the regularized Stokeslet approach, and so we used the integral average approach for the remainder of this study.

After validating the BITS method, we used it to study the instantaneous subduction of a bent sheet comprising a long horizontal part (the 'plate') and a shorter part (the 'slab') bent downward into the am-

bient fluid. A suite of instantaneous flow solutions for different values of the length of the slab, its inclination, and the distance d of the plate from the free surface were first obtained. The numerical solutions show that the smaller d decreases the sheet's subduction velocity and requires a finer discretization. Moreover, the bending moment at the ends is nearly independent of the sheet length. A simple scaling analysis of a subducting sheet suggests that $V/V_{\text{Stokes}} = \text{fct}(St)$, where V is the (vertical) sinking speed of the slab, V_{Stokes} is the slab's characteristic Stokes sinking speed, and St is the sheet's 'flexural stiffness'. We confirm this prediction by showing that numerical solutions of BITS obtained for different slab lengths and viscosity ratios collapse onto a master curve for each assumed value of the inclination. The curves have two limits: a limit $St \leq 1$ for which the sinking speed is controlled by the viscosity of the ambient mantle, and a limit $St \gg 1$ in which it is controlled by the viscosity of the sheet itself (bending resistance). Finally, we performed time-dependent simulations for the evolution of the sheet's shape and thickness. For moderate viscosity ratios (≈ 200 -1000), the sheet thins somewhat as it sinks, but not enough to lead to the 'slab breakoff' that is observed in several subduction zones on Earth (see 'Future perspectives' below).

In the second example, the parallel code BLUE for multi-phase flows was used to simulate three-dimensional viscous folding in diverging microchannels. The code BLUE, developed by S. Shin and thesis co-supervisors D. Juric and J. Chergui, treats the free interface with a parallel Lagrangian front tracking method. Inspired by T. Cubaud's experiments (Cubaud and Mason, 2006a), the calculation domain is a micro rectangle of dimensions 2 mm \times 0.25 mm \times 5 mm. The more viscous liquid L_1 with viscosity η_1 is injected into the channel from the center inlet at a volumetric rate Q_1 , and the less viscous liquid L_2 with viscosity η_2 from two side inlets at a total volumetric rate Q_2 . Liquid

L_1 takes the form of a thin filament due to hydrodynamic focusing in the long channel that leads to the main chamber. This thread, flowing into the main chamber becomes unstable to a folding instability due to the longitudinal compressive stress applied to it by the diverging flow of liquid L_2 . Given the long computation times for such a low Reynolds number flow, we were limited to a parameter study comprising five simulations in which the flow rate ratio, the viscosity ratio, the Reynolds number, and the shape of the channel were varied relative to a reference model.

The hydrodynamic focusing technique provides an effective means of controlling the passage of chemical reagent or bio-samples through microfluidic channels and has given rise to many studies aimed at understanding its physical mechanisms. In our simulations, The contact line where liquid L_1 detaches from the channel walls forms a 'V'-shape and depends on the viscosity ratio, the flow rate ratio and the Reynolds number. The divergence angle α of the main chamber has almost no effect on the focusing. The thread of liquid L_1 in the long microchannel is a plug flow, ensheathed by liquid L_2 . The shape and velocity of the thread vary dramatically at first, then evolve slowly and finally achieve a nearly stable state, which implies that the hydrodynamic focusing phase is complete. Moreover, the cross section of the thread is elliptical rather than circular. The minor and major axes of the thread, ϵ_1 and ϵ_2 respectively are measured for the five simulations. There is a power law relation between the dimensionless minor axis ϵ_1/w and the flow ratio ϕ and our results are in good agreement with experimental and theoretical predictions of other researchers. For the major axis ϵ_2 , the situation is more complicated. The lower viscosity ratio χ decreases the major axis and the thread cross section appears more circular. Additionally, the interfacial tension plays important role in the thread formation after the liquid L_1 detaches from walls.

Unlike the previous two-dimensional simulations of Chung et al. (2010), our simulations are fully three-dimensional and thus do not constrain the axis along which the folding instability could occur. We find that the initial folding axis can be either parallel or perpendicular to the narrow dimension of the chamber. In the former case, the folding slowly transforms via twisting to perpendicular folding, or the folds may disappear altogether. The direction of folding onset is determined by the velocity profile and ellipticity of the thread cross section in the channel that feeds the main microfluidic chamber. The bending moment on the thread cross section, calculated from the velocity profile and the ellipticity, clearly account for the folding direction. When the ratio of semi-major to semi-minor axes is sufficiently large, the folding always occurs perpendicular to the narrow dimension of the chamber.

Due to the high viscosity contrast and very low Reynolds numbers involved, direct numerical simulations of this two-phase flow are very challenging and to our knowledge these are the first three-dimensional direct parallel numerical simulations of viscous threads in microchannels. However, since the computational time for these simulations is quite long, especially for such viscous threads, the simulations present only the early time onset of the buckling instability of the threads, thus long-time comparisons with experiments for quantities such as folding amplitude and frequency are limited.

6.2 Future perspectives

- In the coming year we intend to pursue an extended version of the BITS model in which the rheology of the sheet is non-Newtonian. Unlike the full boundary-element method (BEM), in which each fluid must have a uniform Newtonian viscosity, BITS can incorpo-

rate nonlinear rheology because the flow inside the sheet has a simple form corresponding to stretching plus bending. Our principal motivation for developing a nonlinear BITS model is the geophysical phenomenon of ‘slab detachment’, in which the subducting oceanic lithosphere breaks off in the Earth’s upper mantle (e.g., in the Mediterranean region). Slab detachment is inferred from seismic tomography, and is indicated by the presence of anomalously hot material where the cold sinking slab would otherwise be. In terms of fluid mechanics, slab detachment corresponds to a necking or tearing instability, and the breakoff itself corresponds to a finite-time singularity. Unsurprisingly, our Newtonian BITS calculations displayed only moderate (a few percent) slab thinning at depths corresponding to the Earth’s upper mantle. However, we speculate that non-Newtonian (shear thinning) rheology will lead to enhanced localized thinning and catastrophic breakoff. Our goal will be to understand the fine structure of this instability and to determine the conditions under which it can occur (since it evidently does not occur in all terrestrial subduction zones.)

- To understand the viscous buckling instability in diverging microchannels better, more simulations with a larger range of viscosity ratio χ , Reynolds number Re_2 , flow rate ratio ϕ and with different channel geometries will be implemented. In T. Cubaud’s experiments, there are many kinds of buckling instability patterns: stable, folding, subfolding and heterogeneous deposition to name a few. In our three dimensional simulations, the folding is not constrained to occur along one axis. With further simulations, a phase diagram of flow pattern as a function of the above parameters χ , Re_1 and ϕ can be obtained and the effect of these parameters on the folding frequency can be studied (when the folding instability

occurs). In the future, we can perform more complicated simulations where, for example, the flow rates of less viscous fluid entering from the two side inlets are unequal and thus will enable simulations of hydrodynamic focusing and buckling instability under asymmetric conditions. Moreover, the diverging microchannel can be extended to a diverging-converging microchannel. We can also study the hydrodynamic focusing in a micro geometry which consists of four microchannels with square section of identical width h forming a cross channel. Over a wide range of fluid properties and flow parameters different flow patterns such as threads, jetting or dripping have been observed. These studies will provide a basis for studying flow behavior with viscous industrial, complex fluids in microfluidic systems and biological fluids. Understanding the hydrodynamics of two phase flows with large viscosity ratios is helpful in precisely manipulating soft materials composed of reactive solvents and solutes in micro- and nano-devices.

Bibliography

- J. Atencia and D. J. Beebe. Controlled microfluidic interfaces. *Nature*, 437(7059):648–655, 2005.
- B. Audoly, N. Clauvelin, P.-T. Brun, M. Bergou, E. Grinspun, and M. Wardetzky. A discrete geometric approach for simulating the dynamics of thin viscous threads. *Journal of Computational Physics*, 253:18–49, 2013.
- E. Aulisa, S. Manservigi, and R. Scardovelli. A mixed markers and volume-of-fluid method for the reconstruction and advection of interfaces in two-phase and free-boundary flows. *Journal of Computational Physics*, 188(2):611–639, 2003.
- N. Bellahsen, C. Faccenna, and F. Funiciello. Dynamics of subduction and plate motion in laboratory experiments: insights into the plate tectonics behavior of the earth. *Journal of Geophysical Research: Solid Earth*, 110(B1), 2005.
- F. Bottausci, I. Mezić, C. D. Meinhart, and C. Cardonne. Mixing in the shear superposition micromixer: three-dimensional analysis. *Philosophical Transactions of the Royal Society of London A: Mathematical, Physical and Engineering Sciences*, 362(1818):1001–1018, 2004.
- W. L. Briggs, V. E. Henson, and S. McCormick. A multigrid tutorial. *siam. Philadelphia, USA*, 2000.

- M. R. Bringer, C. J. Gerdts, H. Song, J. D. Tice, and R. F. Ismagilov. Microfluidic systems for chemical kinetics that rely on chaotic mixing in droplets. *Philosophical Transactions of the Royal Society of London A: Mathematical, Physical and Engineering Sciences*, 362(1818):1087–1104, 2004.
- B. A. Buffett and D. B. Rowley. Plate bending at subduction zones: Consequences for the direction of plate motions. *Earth and Planetary Science Letters*, 245(1):359–364, 2006.
- F. Capitanio and G. Morra. The bending mechanics in a dynamic subduction system: Constraints from numerical modelling and global compilation analysis. *Tectonophysics*, 522:224–234, 2012.
- F. Capitanio, G. Morra, and S. Goes. Dynamic models of downgoing plate-buoyancy driven subduction: Subduction motions and energy dissipation. *Earth and Planetary Science Letters*, 262(1):284–297, 2007.
- F. Capitanio, G. Morra, and S. Goes. Dynamics of plate bending at the trench and slab-plate coupling. *Geochemistry, Geophysics, Geosystems*, 10(4), 2009.
- C.-C. Chang, Z.-X. Huang, and R.-J. Yang. Three-dimensional hydrodynamic focusing in two-layer polydimethylsiloxane (pdms) microchannels. *Journal of Micromechanics and Microengineering*, 17(8):1479, 2007.
- Z. Chen, M. Bown, B. OSullivan, J. MacInnes, R. Allen, M. Mulder, M. Blom, and R. vant Oever. Performance analysis of a folding flow micromixer. *Microfluidics and nanofluidics*, 6(6):763–774, 2009.
- A. J. Chorin. Numerical solution of the navier-stokes equations. *Mathematics of computation*, 22(104):745–762, 1968.

- H.-P. Chou, M. A. Unger, and S. R. Quake. A microfabricated rotary pump. *Biomedical Microdevices*, 3(4):323–330, 2001.
- C. Chung, D. Choi, J. M. Kim, K. H. Ahn, and S. J. Lee. Numerical and experimental studies on the viscous folding in diverging microchannels. *Microfluidics and Nanofluidics*, 8(6):767–776, 2010.
- C. P. Conrad and B. H. Hager. Effects of plate bending and fault strength at subduction zones on plate dynamics. *Journal of Geophysical Research*, 104(B8):17551–17571, 1999.
- C. P. Conrad and B. H. Hager. Mantle convection with strong subduction zones. *Geophysical Journal International*, 144(2):271–288, 2001.
- R. Cortez. The method of regularized stokeslets. *SIAM Journal on Scientific Computing*, 23(4):1204–1225, 2001.
- E. Coyajee and B. J. Boersma. Numerical simulation of drop impact on a liquid–liquid interface with a multiple marker front-capturing method. *Journal of Computational Physics*, 228(12):4444–4467, 2009.
- J. Cruickshank. Low-reynolds-number instabilities in stagnating jet flows. *Journal of fluid mechanics*, 193:111–127, 1988.
- J. Cruickshank and B. Munson. An energy loss coefficient in fluid buckling. *Physics of Fluids (1958-1988)*, 25(11):1935–1937, 1982a.
- J. Cruickshank and B. Munson. The viscous-gravity jet in stagnation flow. *Journal of Fluids Engineering*, 104(3):360–362, 1982b.
- J. Cruickshank and B. Munson. A theoretical prediction of the fluid buckling frequency. *Physics of Fluids (1958-1988)*, 26(4):928–930, 1983.
- T. Cubaud and T. G. Mason. Folding of viscous threads in diverging microchannels. *Physical review letters*, 96(11):114501, 2006a.

- T. Cubaud and T. G. Mason. Folding of viscous threads in microfluidics. *Physics of Fluids*, 18(9):091108, 2006b.
- T. Cubaud, M. Tatineni, X. Zhong, and C.-M. Ho. Bubble dispenser in microfluidic devices. *Physical Review E*, 72(3):037302, 2005.
- E. Di Giuseppe, J. Van Hunen, F. Funiciello, C. Faccenna, and D. Giardini. Slab stiffness control of trench motion: Insights from numerical models. *Geochemistry, Geophysics, Geosystems*, 9(2), 2008.
- A. Enns, T. W. Becker, and H. Schmeling. The dynamics of subduction and trench migration for viscosity stratification. *Geophysical Journal International*, 160(2):761–775, 2005.
- D. Enright, R. Fedkiw, J. Ferziger, and I. Mitchell. A hybrid particle level set method for improved interface capturing. *Journal of Computational physics*, 183(1):83–116, 2002.
- C. Faccenna, A. Heuret, F. Funiciello, S. Lallemand, and T. W. Becker. Predicting trench and plate motion from the dynamics of a strong slab. *Earth and Planetary Science Letters*, 257(1):29–36, 2007.
- F. Funiciello, C. Faccenna, D. Giardini, and K. Regenauer-Lieb. Dynamics of retreating slabs: 2. insights from three-dimensional laboratory experiments. *Journal of Geophysical Research: Solid Earth (1978–2012)*, 108(B4), 2003a.
- F. Funiciello, G. Morra, K. Regenauer-Lieb, and D. Giardini. Dynamics of retreating slabs: 1. insights from two-dimensional numerical experiments. *Journal of Geophysical Research: Solid Earth (1978–2012)*, 108(B4), 2003b.
- F. Funiciello, M. Moroni, C. Piromallo, C. Faccenna, A. Cenedese, and H. A. Bui. Mapping mantle flow during retreating subduction: Laboratory models analyzed by feature tracking. *Journal of Geophysical*

- Research: Solid Earth (1978–2012)*, 111(B3), 2006.
- F. Funiciello, C. Faccenna, A. Heuret, S. Lallemand, E. Di Giuseppe, and T. Becker. Trench migration, net rotation and slab–mantle coupling. *Earth and Planetary Science Letters*, 271(1):233–240, 2008.
- S. Goes, F. A. Capitanio, and G. Morra. Evidence of lower-mantle slab penetration phases in plate motions. *Nature*, 451(7181):981–984, 2008.
- R. Griffiths and J. Turner. Folding of viscous plumes impinging on a density or viscosity interface. *Geophysical Journal International*, 95(2):397–419, 1988.
- M. Habibi, S. Hosseini, M. Khatami, and N. Ribe. Liquid supercoiling. *Physics of Fluids (1994-present)*, 26(2):024101, 2014.
- F. H. Harlow, J. E. Welch, et al. Numerical calculation of time-dependent viscous incompressible flow of fluid with free surface. *Physics of fluids*, 8(12):2182, 1965.
- W. R. Jacoby. Model experiment of plate movements. *Nature*, 242(122):130–134, 1973.
- W. R. Jacoby. Paraffin model experiment of plate tectonics. *Tectonophysics*, 35(1):103–113, 1976.
- D. D. Joseph and Y. Renardy. *Fundamentals of two-fluid dynamics: Part II: Lubricated Transport, Drops and Miscible Liquids*. Springer Science & Business Media, 1993.
- T. G. Kang, M. A. Hulsen, P. D. Anderson, J. M. den Toonder, and H. E. Meijer. Chaotic advection using passive and externally actuated particles in a serpentine channel flow. *Chemical Engineering Science*, 62(23):6677–6686, 2007a.
- T. G. Kang, M. A. Hulsen, P. D. Anderson, J. M. d. Toonder, and H. E. Meijer. Chaotic mixing induced by a magnetic chain in a rotating

- magnetic field. *Physical Review-Section E-Statistical Nonlinear and Soft Matter Physics*, 76(6):66303–66303, 2007b.
- C. Kincaid and R. Griffiths. Laboratory models of the thermal evolution of the mantle during rollback subduction. *Nature*, 425(6953):58–62, 2003.
- C. Kincaid and P. Olson. An experimental study of subduction and slab migration. *Journal of Geophysical Research: Solid Earth (1978–2012)*, 92(B13):13832–13840, 1987.
- D. Y. Kwak and J. S. Lee. Multigrid algorithm for cell-centred finite difference method ii : Discontinuous coefficient case. *Department of Mathematics, KAIST, Taejon Korea*, pages 305–701, 2003.
- O. Ladyzhenskaya. *The mathematical theory of incompressible viscous flows*. Gordon and Breach, New York, 1963.
- G.-B. Lee, C.-C. Chang, S.-B. Huang, and R.-J. Yang. The hydrodynamic focusing effect inside rectangular microchannels. *Journal of Micromechanics and Microengineering*, 16(5):1024, 2006.
- Z.-H. Li and N. M. Ribe. Dynamics of free subduction from 3-d boundary element modeling. *Journal of Geophysical Research: Solid Earth (1978–2012)*, 117(B6), 2012.
- L. Mahadevan, W. S. Ryu, and A. D. Samuel. Fluid’rope trick’investigated. *Nature*, 392(6672):140–140, 1998.
- M. Maleki, M. Habibi, R. Golestanian, N. Ribe, and D. Bonn. Liquid rope coiling on a solid surface. *Physical review letters*, 93(21):214502, 2004.
- V. Manea and M. Gurnis. Subduction zone evolution and low viscosity wedges and channels. *Earth and Planetary Science Letters*, 264(1): 22–45, 2007.

- V. C. Manea, M. Pérez-Gussinyé, and M. Manea. Chilean flat slab subduction controlled by overriding plate thickness and trench rollback. *Geology*, 40(1):35–38, 2012.
- K. Meleson, S. Graves, and T. G. Mason. Formation of concentrated nanoemulsions by extreme shear. *Soft Materials*, 2(2-3):109–123, 2004.
- G. Morra, K. Regenauer-Lieb, and D. Giardini. Curvature of oceanic arcs. *Geology*, 34(10):877–880, 2006.
- G. Morra, P. Chatelain, P. Tackley, and P. Koumoutsakos. Earth curvature effects on subduction morphology: Modeling subduction in a spherical setting. *Acta Geotechnica*, 4(2):95–105, 2009.
- P. Paik, V. K. Pamula, and R. B. Fair. Rapid droplet mixers for digital microfluidic systems. *Lab on a Chip*, 3(4):253–259, 2003a.
- P. Paik, V. K. Pamula, M. G. Pollack, and R. B. Fair. Electrowetting-based droplet mixers for microfluidic systems. *Lab on a Chip*, 3(1):28–33, 2003b.
- C. S. Peskin. Numerical analysis of blood flow in the heart. *Journal of computational physics*, 25(3):220–252, 1977.
- C. Piromallo, T. Becker, F. Funicello, and C. Faccenna. Three-dimensional instantaneous mantle flow induced by subduction. *Geophysical Research Letters*, 33(8), 2006.
- M. Pollack, A. Shenderov, and R. Fair. Electrowetting-based actuation of droplets for integrated microfluidics. *Lab on a Chip*, 2(2):96–101, 2002.
- N. Ribe. Bending and stretching of thin viscous sheets. *Journal of Fluid Mechanics*, 433:135–160, 2001.
- N. M. Ribe. Coiling of viscous jets. In *Proceedings of the Royal Society of London A: Mathematical, Physical and Engineering Sciences*, volume

460, pages 3223–3239, 2004.

- N. M. Ribe. Bending mechanics and mode selection in free subduction: A thin-sheet analysis. *Geophysical Journal International*, 180(2):559–576, 2010.
- N. M. Ribe, J. R. Lister, and S. Chiu-Webster. Stability of a dragged viscous thread: Onset of stitching in a fluid-mechanical sewing machine. *Physics of Fluids*, 18(12):124105, 2006.
- A. Rida and M. Gijs. Manipulation of self-assembled structures of magnetic beads for microfluidic mixing and assaying. *Analytical chemistry*, 76(21):6239–6246, 2004.
- W. Schellart. Kinematics of subduction and subduction-induced flow in the upper mantle. *Journal of Geophysical Research: Solid Earth (1978–2012)*, 109(B7), 2004a.
- W. Schellart. Quantifying the net slab pull force as a driving mechanism for plate tectonics. *Geophysical Research Letters*, 31(7), 2004b.
- W. Schellart. Kinematics and flow patterns in deep mantle and upper mantle subduction models: Influence of the mantle depth and slab to mantle viscosity ratio. *Geochemistry, Geophysics, Geosystems*, 9(3), 2008.
- W. Schellart, J. Freeman, D. Stegman, L. Moresi, and D. May. Evolution and diversity of subduction zones controlled by slab width. *Nature*, 446(7133):308–311, 2007.
- W. Schellart, D. Stegman, R. Farrington, J. Freeman, and L. Moresi. Cenozoic tectonics of western North America controlled by evolving width of Farallon slab. *Science*, 329(5989):316–319, 2010.
- H. Schmeling, A. Babeyko, A. Enns, C. Faccenna, F. Funiciello, T. Gerya, G. Golabek, S. Grigull, B. Kaus, G. Morra, et al. A bench-

- mark comparison of spontaneous subduction models: towards a free surface. *Physics of the Earth and Planetary Interiors*, 171(1):198–223, 2008.
- S. Shin. Computation of the curvature field in numerical simulation of multiphase flow. *Journal of Computational Physics*, 222(2):872–878, 2007.
- S. Shin and D. Juric. Modeling three-dimensional multiphase flow using a level contour reconstruction method for front tracking without connectivity. *Journal of Computational Physics*, 180(2):427–470, 2002.
- S. Shin and D. Juric. High order level contour reconstruction method. *Journal of mechanical science and technology*, 21(2):311–326, 2007.
- S. Shin and D. Juric. A hybrid interface method for three-dimensional multiphase flows based on front tracking and level set techniques. *International Journal for Numerical Methods in Fluids*, 60(7):753–778, 2009a.
- S. Shin and D. Juric. Simulation of droplet impact on a solid surface using the level contour reconstruction method. *Journal of mechanical science and technology*, 23(9):2434–2443, 2009b.
- S. Shin, S. Abdel-Khalik, V. Daru, and D. Juric. Accurate representation of surface tension using the level contour reconstruction method. *Journal of Computational Physics*, 203(2):493–516, 2005.
- S. Shin, I. Yoon, and D. Juric. The local front reconstruction method for direct simulation of two-and three-dimensional multiphase flows. *Journal of Computational Physics*, 230(17):6605–6646, 2011.
- S. Shin, J. Chergui, and D. Juric. A solver for massively parallel direct numerical simulation of three-dimensional multiphase flows. *arXiv preprint arXiv:1410.8568*, 2014.

- C. Simonnet and A. Groisman. Two-dimensional hydrodynamic focusing in a simple microfluidic device. *Applied Physics Letters*, 87(11):114104, 2005.
- M. Skorobogatiy and L. Mahadevan. Folding of viscous sheets and filaments. *EPL (Europhysics Letters)*, 52(5):532, 2000.
- T. M. Squires and S. R. Quake. Microfluidics: Fluid physics at the nanoliter scale. *Reviews of modern physics*, 77(3):977, 2005.
- D. Stegman, J. Freeman, W. Schellart, L. Moresi, and D. May. Influence of trench width on subduction hinge retreat rates in 3-d models of slab rollback. *Geochemistry, Geophysics, Geosystems*, 7(3), 2006.
- D. Stegman, R. Farrington, F. Capitanio, and W. Schellart. A regime diagram for subduction styles from 3-d numerical models of free subduction. *Tectonophysics*, 483(1):29–45, 2010a.
- D. Stegman, W. Schellart, and J. Freeman. Competing influences of plate width and far-field boundary conditions on trench migration and morphology of subducted slabs in the upper mantle. *Tectonophysics*, 483(1):46–57, 2010b.
- T. Stiles, R. Fallon, T. Vestad, J. Oakey, D. Marr, J. Squier, and R. Jimenez. Hydrodynamic focusing for vacuum-pumped microfluidics. *Microfluidics and Nanofluidics*, 1(3):280–283, 2005.
- H. A. Stone, A. D. Stroock, and A. Ajdari. Engineering flows in small devices: microfluidics toward a lab-on-a-chip. *Annu. Rev. Fluid Mech.*, 36:381–411, 2004.
- A. D. Stroock, S. K. Dertinger, A. Ajdari, I. Mezić, H. A. Stone, and G. M. Whitesides. Chaotic mixer for microchannels. *Science*, 295(5555):647–651, 2002a.
- A. D. Stroock, S. K. Dertinger, G. M. Whitesides, and A. Ajdari. Pat-

- terning flows using grooved surfaces. *Analytical Chemistry*, 74(20):5306–5312, 2002b.
- M. Sussman and E. G. Puckett. A coupled level set and volume-of-fluid method for computing 3d and axisymmetric incompressible two-phase flows. *Journal of Computational Physics*, 162(2):301–337, 2000.
- G. Taylor. Instability of jets, threads, and sheets of viscous fluid. In *Applied Mechanics*, pages 382–388. Springer, 1969.
- B. Tchavdarov, A. Yarin, and S. Radev. Buckling of thin liquid jets. *Journal of Fluid Mechanics*, 253:593–615, 1993.
- M. F. Tome and S. Mckee. Numerical simulation of viscous flow: buckling of planar jets. *International journal for numerical methods in fluids*, 29(6):705–718, 1999.
- S. Toppaladoddi and N. Balmforth. Slender axisymmetric stokesian swimmers. *Journal of Fluid Mechanics*, 746:273–299, 2014.
- B. J. Torby. *Advanced dynamics for engineers*. Holt Rinehart & Winston, 1984.
- A.-K. Tornberg and M. J. Shelley. Simulating the dynamics and interactions of flexible fibers in stokes flows. *Journal of Computational Physics*, 196(1):8–40, 2004.
- A. Utada, E. Lorenceau, D. Link, P. Kaplan, H. Stone, and D. Weitz. Monodisperse double emulsions generated from a microcapillary device. *Science*, 308(5721):537–541, 2005.
- T. Vilkner, D. Janasek, and A. Manz. Micro total analysis systems. recent developments. *Analytical chemistry*, 76(12):3373–3386, 2004.
- G. Whitesides and A. Stroock. Flexible methods for microfluidics. *Phys Today*, 54(6):42–48, 2001.

- Z. Wu and N.-T. Nguyen. Hydrodynamic focusing in microchannels under consideration of diffusive dispersion: theories and experiments. *Sensors and Actuators B: Chemical*, 107(2):965–974, 2005.

Titre : Hydrodynamique de fluides élancés à bas nombres de Reynolds

Mots clés : bas nombre de Reynolds, fluide élancé, subduction, micro-canal divergent, flambage visqueux

Résumé : Cette thèse concerne la simulation numérique d'écoulement de nappes et/ou de filamenteux de fluides visqueux en présence d'une seconde phase fluide non-miscible dont la viscosité est différente. Deux exemples sont présentés. Celui de la subduction de la lithosphère océanique ainsi que celui du flambage de filaments visqueux dans un micro-canal divergent. Ces deux écoulements sont en particulier caractérisés par un nombre de Reynolds relativement bas ($Re \ll 1$).

Dans le premier cas, une méthode hybride dite BITS (Boundary Integral & Thin Sheet) est proposée dont nous validerons les résultats avec ceux obtenus et confirmés par une méthode dite d'éléments aux frontières. Les solutions instationnaires et dépendantes du temps sont obtenues avec la méthode BITS. L'analyse des échelles de vitesse normalisées par la fonction de rigidité en flexion indique une bonne concordance avec les prédictions numériques que nous avons obtenues. A des nombre de

Reynolds modérés (~ 100), la nappe s'amincit considérablement pendant son écoulement sans pour autant atteindre sa rupture tel que cela est observé dans différentes régions de subduction terrestre.

Dans le second cas, nous avons utilisé le code BLUE pour réaliser simulations numériques 3D diphasiques d'écoulements visqueux dans une configuration de flambage en micro-canal divergent. L'écoulement dépend de plusieurs paramètres dont le rapport des débits volumétriques, le rapport des viscosités, le nombre de Reynolds et l'angle du micro-canal divergent. Il apparaît de cette étude que le filament présente une instabilité du type flambage en raison de la contrainte de compression. L'axe principal de flambage peut être alors parallèle ou perpendiculaire à la direction étroite de la chambre. Dans le cas parallèle, le flambage tend lentement vers un flambage perpendiculaire au moyen d'une torsion ou peut totalement disparaître.

Title : Low Reynolds number hydrodynamics of immersed thin and slender bodies

Keywords : low Reynolds number, thin sheet, subduction, diverging microchannel, viscous folding

Abstract : The hydrodynamics of thin (sheet-like) and slender (filamentary) bodies of viscous fluid immersed in a second fluid with a different viscosity is studied. Here we focus on two examples: the subduction of oceanic lithosphere and the buckling of viscous threads in diverging microchannels, both have a characteristic Reynolds number $Re \ll 1$.

A hybrid boundary integral & thin sheet method (BITS) is build for the subduction of 2D immersed sheet. After the validation by comparing with the results of full boundary elements method, both instantaneous and time-dependent solutions are done to analyze the subduction with BITS method. The scaling analysis of the normalized sinking speed as a function of the sheet's 'flexural stiffness' is confirmed by our numerical predictions. For

moderate viscosity ratios (~ 100), the sheet thins substantially as it sinks, but not enough to lead to the 'slab breakoff' that is observed in several subduction zones on Earth.

Next, the parallel code BLUE for multi-phases flows is used to simulate the 3D viscous folding in diverging microchannels. We performed a parameter study comprising five simulations in which the flow rate ratio, the viscosity ratio, the Reynolds number, and the shape of the channel were varied relative to a reference model. The thread becomes unstable to a folding instability due to the longitudinal compressive stress. The initial folding axis can be either parallel or perpendicular to the narrow dimension of the chamber. In the former case, the folding slowly transforms via twisting to perpendicular folding, or may disappear totally.